

DISSERTATION

H^- Ion Source Developments and Diagnostics at CERN

ausgeführt zum Zwecke der Erlangung des akademischen Grades eines
Doktors der technischen Wissenschaften unter der Leitung von

O. Univ. Prof. Dr. H. Winter
E134
Institut für Allgemeine Physik

durchgeführt am
Europäischen Kernforschungszentrum CERN
CH-1211 Genf 23

eingereicht an der Technischen Universität Wien
Fakultät für Physik

von
Dipl.Ing. Thomas Steiner
9325982
A-2560 Neusiedl, Dorfstraße 59

Diese Arbeit wurde unterstützt vom Österreichischen Bundesministerium
für Bildung, Wissenschaft und Kultur.

Wien, am 23. Mai 2005



Kurzfassung

Eine wesentliche Voraussetzung zukünftiger CERN Programme, wie der Large Hadron Collider (LHC), die ISOLDE Kollaboration und die Experimentierzonen des Proton Synchrotrons (PS), ist eine Steigerung der Intensität und der Dichte des Protonenstrahls. Die momentane Kombination des Linearbeschleunigers, Linac2, und des PS Booster Synchrotrons (PSB) limitiert die Leistung der gesamten nachfolgenden Kette von Kreisbeschleunigern.

Eine effektive Verbesserungsmöglichkeit ist die Injektion von H^- -Ionen bei höherer Energie mit anschließendem Stripping. Der dafür nötige H^- -Linearbeschleuniger kann als Linac4 mit 160 MeV in den PSB oder in einer supraleitenden Ausbaustufe als Superconducting Proton Linac (SPL) mit 2.2 GeV direkt in das PS injizieren.

Für beide Optionen benötigt man eine sehr zuverlässige H^- -Ionenquelle mit hohem Ionenstrom und einfacher Wartung. Design, Aufbau und Charakterisierung eines ersten H^- -Quellenprototyps sind das Ziel dieser Dissertation. Ausgangspunkt ist aufgrund der Erfahrung mit der Erzeugung von Schwerionen am CERN eine Quelle basierend auf Mikrowellentechnologie.

Ein Quellenprototyp mit „multicusp“ Magnetstruktur und der Aufbau der Experimentierumgebung ermöglichen eine erste Extraktion von H^- -Ionen am CERN. Für die Diagnostik wurde ein Spektrometer zur Trennung des H^- -Strahls vom Elektronstrahl gebaut. Variation der Quellenparameter, z.B. Mikrowellenleistung, Gasfluss, Antennenposition oder Polarisierung der Plasmaelektrode, resultierten in einer Steigerung des Ionenstroms. Die „multicusp“ Magnetstruktur wurde durch zwei Solenoide und in Folge durch eine Kombination von „multicusp“ Struktur und Solenoide ersetzt. Experimente mit verschiedenen Gaszusätzen, einem Metallgitter zur Mikrowelleneindämmung in der Plasmakammer, Einsätzen aus Tantal und Simulationen des Magnetfeldes wurden für jede Magnetstruktur durchgeführt.

Das Mikrowellensystem wurde mit „Microwave Studio“ simuliert und anschließend vermessen; in weiterer Folge wurde zur Verbesserung der Mikrowelleneinspeisung ein entsprechender Übergang konstruiert.

Ein wesentlicher Teil der Arbeit ist auch die Entwicklung des Niederenergie-Strahltransportes (LEBT) und Vielteilchensimulationen zur Kontrolle der Transporteigenschaften für die 3 MeV Experimentieranlage der CERN/IPHI Kollaboration.

Die Dissertation wurde im Rahmen des Österreichischen CERN-Doktorantenprogramms, gefördert vom Österreichischen Bundesministerium für Bildung, Wissenschaft und Kultur, in der Sektion „Hadron Sources & Linacs“ der „Accelerators & Beam Physics“ Gruppe durchgeführt. Sie ist außerdem Bestandteil einer Framework 5 Kollaboration (HP-NIS) und von der Europäischen Union per Vertrag N°: HPRI-CT-2001-50021 unterstützt.

Abstract

An essential improvement for future CERN programs, e.g. the Large Hadron Collider (LHC), the ISOLDE collaboration and the experimental areas of the Proton Synchrotron (PS), is an increase of the intensity and brightness of the proton beam. The current combination of the linear accelerator, Linac2, and the PS Booster Synchrotron (PSB) limits the performance of the subsequent chain of circular accelerators.

The injection of H^- ions at higher energy with subsequent stripping is an effective possible upgrade. The necessary linear accelerator (Linac4) injects at 160 MeV into the PSB or in a superconducting second stage as Superconducting Proton Linac (SPL) at 2.2 GeV directly into the PS.

For both options a high performance, high reliability, negative hydrogen ion source with easy maintenance is needed. Design, construction and characterisation of a first H^- ion source prototype are the aim of this thesis. Based on the experience in the production of heavy ions at CERN, a microwave driven source was chosen as a starting point.

The construction of both a first source prototype, equipped with a magnetic multicusp structure, and the experimental environment allowed a first extraction of H^- ions at CERN. For diagnostics a spectrometer for the separation of the electron and the H^- ion beam was built. Variation of the source parameters, e.g. microwave power, gas flow, antenna position and polarisation of the plasma electrode, resulted in an increase of the ion current. The multicusp structure was replaced by two solenoids and in succession by a combination of multicusp and solenoidal structure. Experiments with different secondary gas additions, a metal grid for microwave suppression in the plasma chamber, tantalum inserts and simulations of the magnetic field were done for each magnetic structure.

The microwave system was simulated with Microwave Studio and measured; to improve the microwave injection a taper was constructed.

Another important part of this work is the development of the Low Energy Beam Transfer Line (LEBT) and multi-particle simulations to check the transport characteristics for the 3 MeV test stand of the CERN/IPHI collaboration.

This work was performed within the Austrian Doctoral Student Programme at CERN, instituted and financed by the Austrian Federal Ministry for Education, Science and Culture in the Hadron Sources & Linacs Section of the Accelerators & Beam Physics Group.

It is also supported by the European Commission under contract n°: HPRI-CT-2001-50021.

Acknowledgements

First I would like to express my entire and sincere thanks to my parents, my partner, my family and my friends, especially the A-TEAM, for their support and encouragement throughout the whole PhD time.

I would like to thank my university supervisor O. Univ. Prof. Dr. H. Winter from the Institut für Allgemeine Physik of the Technical University of Vienna and my CERN supervisor, Dr. D. Küchler of the AB Department, for their help and commitment shown during the last three years.

I am pleased to have the opportunity to also thank C. Hill, R. Scrivens, A. Lombardi, R. Gobin, O. Tuske and M. Bacal for numerous stimulating and interesting discussions. I am grateful for the help of M. O'Neil and C. Mastrostefano during the installation and upgrade of the H^- ion source prototype, the assistance of B. Hadorn with the technical drawings and the continuous support of the vacuum and RF group.

This work was performed within the Austrian Doctoral Student Programme at CERN, instituted and financed by the Austrian Federal Ministry for Education, Science and Culture in the Hadron Sources & Linacs Section of the Accelerators & Beam Physics Group.

It is also supported by the European Commission under contract n°: HPRI-CT-2001-50021.

Contents

1	Introduction	7
2	Negative ion interactions	11
2.1	Negative ion formation processes	11
2.1.1	Volume formation of H^- ions	12
2.1.2	Surface formation of H^- ions	17
2.2	Negative ion destruction processes	17
2.2.1	Cross-sections of H^- destruction	18
3	An overview of H^- ion sources	21
3.1	Operational characteristics of selected H^- ion sources	22
3.1.1	Filament multicusp H^- ion sources	22
3.1.2	Magnetron H^- ion sources	23
3.1.3	Penning H^- ion source	24
3.1.4	RF driven multicusp H^- ion sources	25
3.1.5	ECR H^- ion source	25
3.2	Selected H^- ion sources and the LINAC4/SPL requirements	29
4	Experimental setup	31
4.1	Magnetic field configurations	32
4.1.1	Multicusp structure	32
4.1.2	Solenoidal structure	33
4.1.3	Combination of solenoidal and multicusp structure	35
4.2	Microwave-system	36
4.2.1	Microwave transition	38
4.2.2	Improved microwave transition	38
4.3	e^-/H^- -separation	42
5	Experiments with the CERN H^- source	43
5.1	Source behavior for different magnetic structures	44
5.1.1	Multicusp structure with additional permanent magnets	44
5.1.2	Solenoidal structure	49
5.1.3	Combination of solenoidal and multicusp structure	55
5.2	The influence of tantalum on the H^- ion production	57
5.3	Effect of a collar	60
5.4	Microwave suppression in the H^- production region	61
5.5	ECR heating on a boron nitride wall	62

5.6	H ⁻ ion production with addition of different support gases	66
5.6.1	Argon	67
5.6.2	Helium	68
5.6.3	Xenon	68
5.7	Different support gases at the CEA/Saclay	70
6	The Low Energy Beam Transfer Line	73
6.1	LEBT types	73
6.2	LEBT for the H ⁻ source at CERN	75
6.2.1	Basic decisions on the LEBT layout	77
6.2.2	Multi-particle tracking through the LEBT	79
6.2.3	Space charge compensation	80
6.2.4	Gas stripping losses	82
7	Conclusions	85
A	Drawings of the H⁻ ion source	95

Chapter 1

Introduction

CERN is committed to the realisation of the Large Hadron Collider (LHC) [70] with physics starting in the year 2007. This very high energy accelerator depends upon a cascade of lower energy machines that supply the beam (see Figure 1.1).

These high performance proton injectors are essential, and their improvement will increase the potential of the LHC itself.

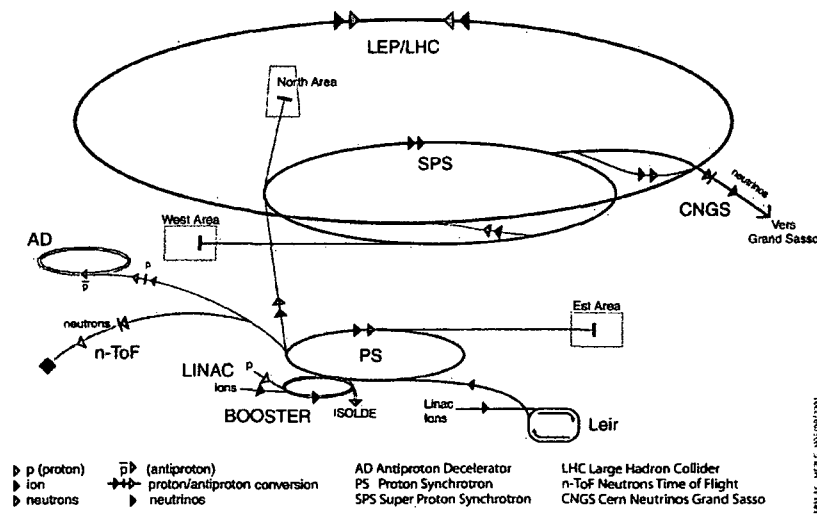


Figure 1.1: CERN accelerator complex (operating or approved projects).

Linac2, the present injector of the CERN PS Booster (PSB), could be a limit on the performance of the proton accelerator complex because of its low output energy (50 MeV). To remove this bottleneck a new proton injector for the PSB, named Linac4 [33, 87], is presently under study in the framework of the Superconducting Proton Linac (SPL) study [32, 34, 35] at CERN. Linac4 will deliver H^- ions at 160 MeV to the PSB.

For the complete list of all the different upgrade options see [15].

The step towards this H^- linac, associated with charge-exchange injection and the upgrade of the injection energy, would double the brightness and intensity of the beam delivered by the PS Booster.

At the same time Linac4 is being designed as the front end of the more ambitious accelerator, the SPL, a 4 MW 2.2 GeV linac directly injecting into the Proton Synchrotron (PS). The SPL would upgrade the CERN hadron injector system to the requirements of the next class of experiments in the field of neutrino and radioactive ion beam physics and could contribute to push the LHC beam beyond its design maximum intensity, if needed.

In order to increase the intensity in proton machines, the charge exchange injection scheme has been widely used since the 70's.

The advantage of injecting particles in another charge state (H^-) than the stored one (H^+) is that it enables accumulation of like particles in an already occupied volume of phase-space, cheating Liouville's theorem [18]:

In the vicinity of a particle, the particle density in phase space is constant if the particles move in an external magnetic field or in a general field in which the forces do not depend upon velocity.

According to this, whatever magnetic focussing or bending operation is done on the beam(s), the volume occupied by a given number of particles remains invariant.

For hadrons the beam density at injection is either limited by space charge effects or by the injector, delivering the beam, e.g. the linear accelerator. In order to increase the intensity, multi-turn injection is used to fill the phase space.

As dictated by Liouville's theorem, for each multi-turn injection another empty phase space volume has to be used, which is equivalent to emittance growth. The maximum number of injections, e.g. the intensity, is thus limited by the acceptance of the receiving circular accelerator.

These constraints on conventional multi-turn injection do not apply to charge-exchange injection since the stripping of H^- ions to protons after the injection occurs within the acceptance of the ring.

For H^- ion injection, bump dipoles lift the beam from the central orbit to one passing through a stripping foil (see Figure 1.2). A first dipole combines protons and H^- ions in the same real-space volume.

Both particle species continue to the stripping foil, for example aluminium oxide or carbon, typically with a stripping efficiency for the two electrons of the H^- ion of $\sim 98\%$, with $\sim 2\%$ remaining mainly as H atoms.

A second dipole removes the H atoms and unstripped H^- ions.

For a high intensity machine, the aim of the injection process is to fill prescribed emittances in the longitudinal and both transverse phase planes in such a way that the resulting beam distributions do not lead to excessive space-charge forces.

Charge exchange injection into the circular accelerators will require a high current, high duty cycle, high reliability H^- source. Both the Linac4 and SPL source requirements are given in Table 1.1.

Design, construction and characterisation of an H^- ion source prototype, using some non standard approaches, are the main goal of this work. The developments are based on a microwave driven source due to the good and extensive experience with the ECR technology for the heavy ion physics program.

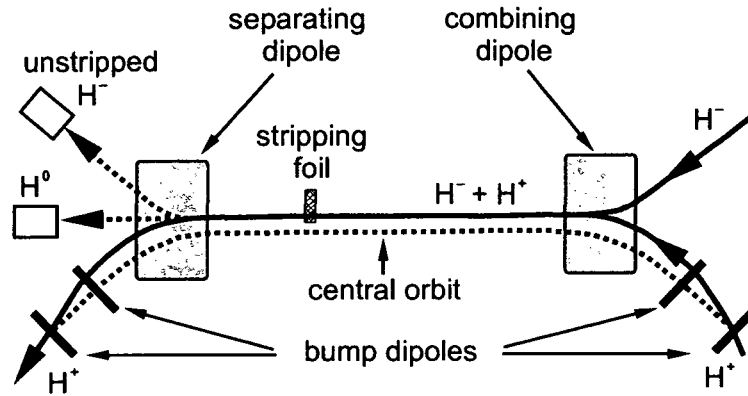


Figure 1.2: Charge-exchange injection scheme [18].

A complete and thorough exploration of parameter space is carried out to its applicable extent, including the variation of the magnetic structure, at a single source for the first time.

Based on the experiences gathered with the prototype source, recommendations for a decision on a second generation source and the future strategy concerning H^- ion production at CERN are given.

	Linac4	SPL
Instantaneous current	50 mA	>40 mA
Pulse length	0.5 ms	2.8 ms ^a
Repetition rate	2 Hz	50 Hz
Extraction voltage	95 kV	95 kV
Emittance (rms normalised) ^b	0.25 π mm mrad	0.25 π mm mrad
Availability for tests	2007	2012
Assumed start of operational use	~2008	~2013
Further features (not essential but desired)	caesium free no antenna or filament in the plasma chamber high pulse-to-pulse stability mean time between failure: 100 days easy maintenance	

^a1.5 ms for the new SPL Layout (2005)

^bEmittance at RFQ input

Table 1.1: Parameters of an H^- ion source for Linac4 and SPL (February 2004).

An essential part of this work is the design of the Low Energy Beam Transfer Line

(LEBT) and the corresponding multi-particle simulations, which provide the opportunity to optimise the transport characteristics for the 3 MeV experiment of the CERN/IPHI collaboration.

Chapter 2

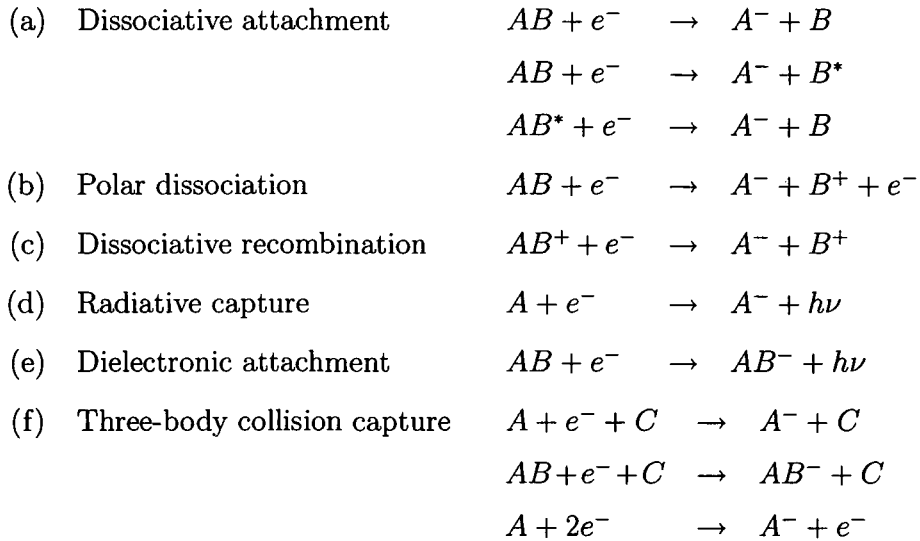
Negative ion interactions

This chapter is giving an overview on some of the processes leading to the generation and the destruction of negative ions in general and H^- ions in particular. More detailed information can be found at [29, 119, 120].

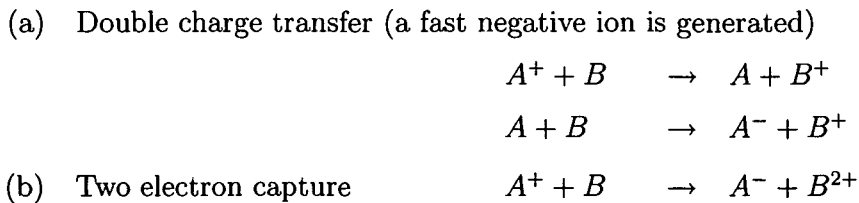
2.1 Negative ion formation processes

Negative ions are mainly generated by the following processes:

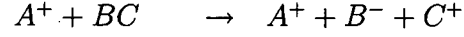
1. Electron impact:



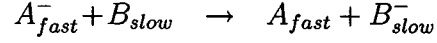
2. Ion or atom collisions:



- (c) Polar dissociation (a slow negative ion is generated)

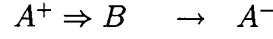


- (d) Charge transfer

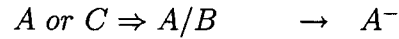
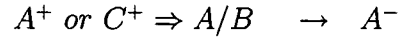


3. Particle impacts onto a solid surface B or a surface with adsorbed atoms (A/B):

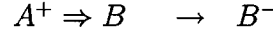
- (a) Reflection capture



- (b) Desorption capture



- (c) Sputtering capture



- (d) Negative surface ionisation



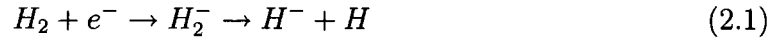
For the processes 3b to 3d the incident particle (A or A⁺, C or C⁺) is adsorbed, absorbed, backscattered into the plasma, etc.

Modern H⁻ ion sources like the Magnetron, the Penning source or the surface converter source are relying on caesiated surfaces for the production of H⁻ ions (see Point 3 above). Another possibility for H⁻ generation is the volume production, discovered in 1977 by M. Bacal [8, 77] and nowadays used in RF and Tandem sources.

2.1.1 Volume formation of H⁻ ions

H⁻ ion formation by electron impact

1a. Dissociative attachment Frequently this is the main process for formation of negative ions in a general source plasma. For hydrogen this gives:

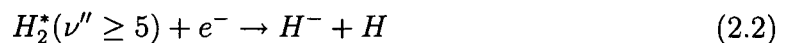


At low energy, electron capture is a transition from the ground state of H₂ to one of the autodetachment H₂⁻ states. These states are not stable, they have a lifetime of ~10⁻¹³–10⁻¹⁵ seconds. There is a strong probability of dissociation occurring before the autodetachment of the captured electron, resulting in H⁻ formation.

The cross-section of dissociative attachment as a function of electron energy is shown in Figure 2.1.

The dissociative attachment has three strong resonant characteristics up to an electron energy of around 15 eV and its probabilities are proportional to the lifetime of H₂⁻.

An abnormally high H⁻ density (e.g. 20 - 30 % of the plasma density) has been observed in low *n_e* and *T_e* (~0.1 - 0.4 eV) plasmas. It is now believed that the principal production process of these H⁻ ions is dissociative attachment to vibrationally excited H₂:



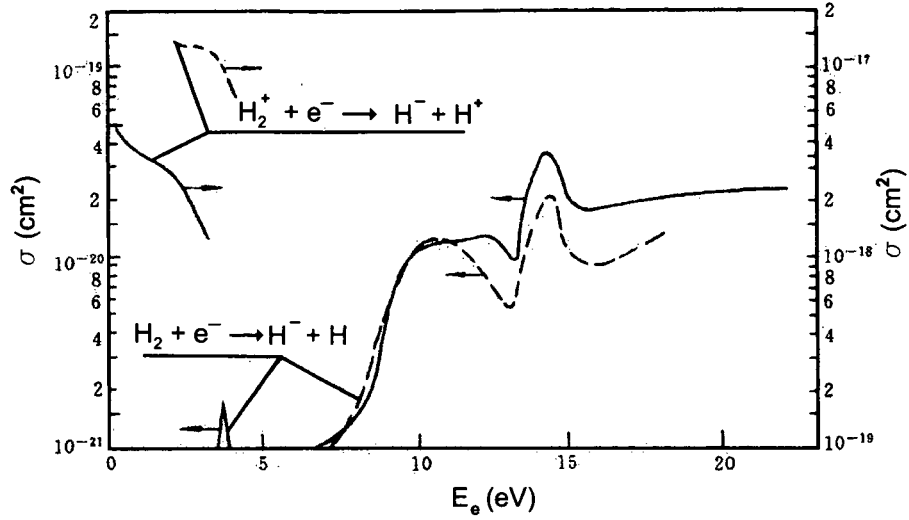


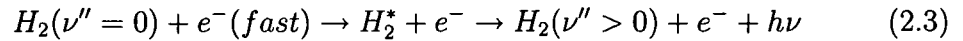
Figure 2.1: The cross-sections for H^- formation by electron impact versus electron energy [120].

Compared to the ground state of H_2 , the dissociation time of $H_2^*(\nu'' \geq 5)$ is considerably shorter. As a result the maximum cross-sections of the dissociative attachment for excited states are larger than for $H_2(\nu'' = 0)$ by a factor of $\sim 10^5$. The optimum electron energies are near their threshold ($\sim 0.5 - 1$ eV), as shown in Figure 2.2. The theoretical results are in agreement with the measured results.

In Tandem H^- ion sources (see also Chapter 3.1.5), up to $\sim 85\%$ of the total negative ion yield may be derived from the medium part of the vibrational spectrum ($5 \leq \nu'' \leq 11$). However, the calculated H^- ion densities are much lower than those measured. Some additional source terms for H^- ion generation are being considered.

Several processes for the production of vibrationally excited $H_2(\nu'')$ in Tandem H^- ion sources are:

1. Proceeding through the electronically excited singlet states by fast electrons:

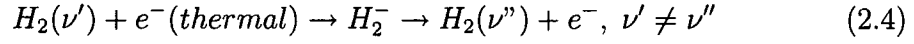


This is the principal process in most volume source discharges with high electron densities ($n_e \gtrsim 10^{12} \text{ cm}^{-3}$).

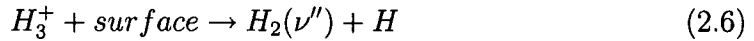
The excitation cross-sections to the level (ν'') from the initial level $(\nu'' = 0)$ as a function of the electron energy are shown in Figure 2.3. It is important that the optimum energy is ~ 40 eV. By numerical studies, the $H_2(\nu'')$ creation and the H^- production depend hardly on the shape of the energy distribution of the fast electrons if their energy is > 40 eV.

2. Proceeding through an intermediate resonant state H_2^- by a slow electron, followed

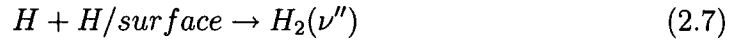
by autodetachment and leaving behind a vibrationally excited molecule, the following is obtained:



3. Generated by H_2^+ or H_3^+ wall collisions (an electron donated by the surface):



4. Generated by atom recombination on the walls:



5. Generated by H_3^+ recombination

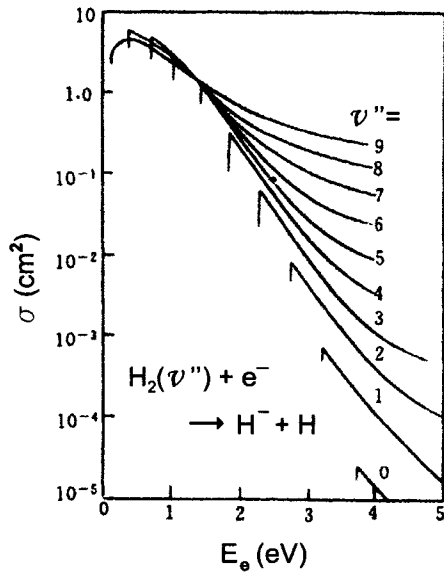
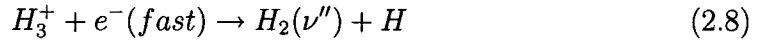


Figure 2.2: Cross-sections for electron dissociative attachment to excited hydrogen molecules [120].

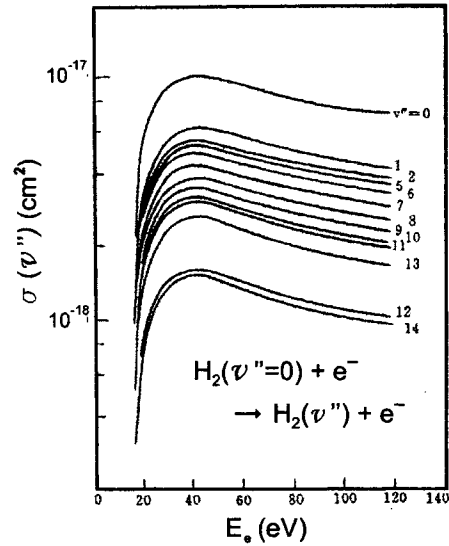
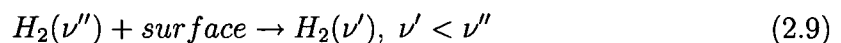


Figure 2.3: Excitation cross-sections from an initial level, $\nu'' = 0$, to a final level, $\nu'' \neq 0$ [120].

Several theoretical models predict a plateau in the distribution of vibrational levels ($\nu'' = 5 - 11$). However, the measured populations ($\nu'' = 1 - 8$) appear to be almost a Boltzmann distribution and are well described by a temperature of 0.36 eV. The principal loss process for the $H_2(\nu'')$ is the wall relaxation,



1b. Polar dissociation Attachment may occur as a result of electron (photon or other heavy particles) interaction with molecular neutrals in which sufficient energy is imparted to excite the molecule to an unstable state which dissociates spontaneously into positive and negative ions.

For hydrogen it is:



in which the electron directly excites a repulsive H^- and H^+ state. The process has an electron threshold energy of ~ 17.2 eV. With an electron energy of $E_e \lesssim 38$ eV the cross-section increases approximately linearly with E_e , up to a maximum of $\sim 1.7 \cdot 10^{-20}$ cm², and then falls after about ~ 50 eV. Compared to dissociative attachment, this process can be neglected when $kT_e < 10$ eV.

1c. Dissociative recombination Theoretically dissociative recombination, $H_2^+ + e^- \rightarrow H^- + H^+$, becomes energetically possible above the electron energy of 1.9 eV. The theoretical and experimental cross-sections are shown in Fig 2.1. Its cross-section falls rapidly with increasing electron energy, but is three orders of magnitude above the value for dissociative attachment when $E_e < 3.7$ eV, so it may be a process for H^- formation in a low-temperature plasma with a high fraction of H_2^+ ions.

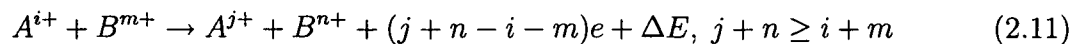
Besides H_2^+ dissociative recombination, H^- ions can also be formed by H_3^+ dissociative recombination: $H_3^+ + e^- \rightarrow H^- + H_2^+$. The maximum cross-section is $\sim 1.6 \cdot 10^{-18}$ cm² at the peak electron energy of ~ 7.5 eV.

1d. Radiative capture For hydrogen, $H + e^- \rightarrow H^- + h\nu$ has a maximum cross-section of $\sim 5 \cdot 10^{-22}$ cm², at a peak energy of ~ 0.7 eV, so it can be neglected in a general source plasma.

1f. Three-body collision capture For hydrogen this process will be as important as radiative capture only at very high electron densities ($n_e \gtrsim 10^{18}$ cm⁻³) or at high H (or H_2) densities ($n_H \gtrsim 10^{16}$ cm⁻³). The process is negligible in general ion sources.

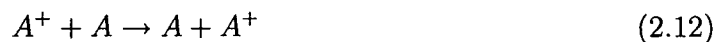
H^- ion formation by multiple charge transfer

A charge transfer collision is a collision between an energetic particle A and a target particle B as follows:



where ΔE is the change in the total internal energy of the system, called the energy defect. The cross-section is represented by σ_{ij} .

The process



having zero energy defect and a large cross-section, is termed "symmetrical resonance charge transfer". At a given impact energy, σ turns out to be inversely proportional to the ionisation potential. The resonance charge transfer cross-section for H^+ , H_2^+ and H^- are shown in Figure 2.4.

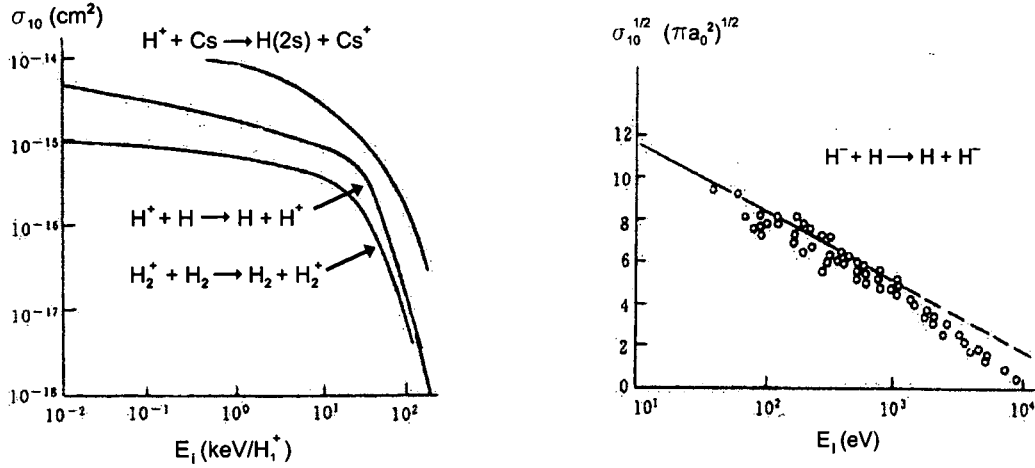


Figure 2.4: The cross-sections of some charge transfer reactions for hydrogen ions ($a_0 = 0.529 \cdot 10^{-8} \text{cm}$) [120].

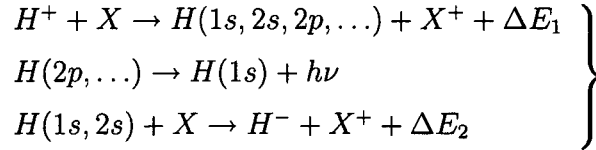
Between different systems the charge transfer is



For capture from and into the ground state, ΔE is given by the difference in first ionisation energy of the particles A and B. The lower the value of ΔE , the larger the cross-section. The energy defect, ΔE , can be minimised by a charge transfer medium which has a low ionisation energy.

The cross-section for $H^+ + Cs \rightarrow H(2s) + Cs^+$ is shown in Figure 2.4.

In an alkali metal vapor, e.g. Cs, $\sigma_{1-1} \ll \sigma_{10}$. Therefore the conversion of a positive ion to a negative ion is mainly a sequential capture of two electrons, e.g. for hydrogen:



For alkali vapor targets, $\sigma_{10} \approx 10^{-14} \text{cm}^2$. Due to the near degeneracy in the potential energies between the reactants and products for $H(n=2)$, most of the formal hydrogen atoms are in the excited state $n=2$, which has a long lifetime of $\sim 0.14 \text{s}$. The energy defect, ΔE_2 , for H^- formation from the metastable $H(2s)$ is less than from the ground state, $H(1s)$, thus H^- is mainly formed by a sequential collision with $H(2s)$.

2.1.2 Surface formation of H^- ions

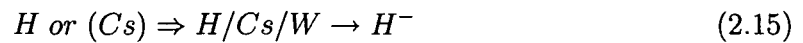
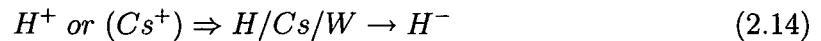
When an energetic ion or atom impinges on a solid surface, many intricate processes can occur, such as reflection or absorption of the incoming projectile, sputtering of the solid material or coated surface materials, desorption of the adsorbed gas on the surface, recombination or dissociation, secondary electron emission, photo emission or excitation. The various particles ejected from the surface may be of different charge states, excited states and mass content, etc.

The work function, W_ϕ , is the most important parameter affecting the yield of negative ions from a surface. An electron is captured or injected by the adsorbate during adsorption. When the work function of the metal substrate is greater than the ionisation energy E_i of the adsorbed atoms, therefore when the energy level of the valence electrons of the adsorbate is above the Fermi electron level of the adsorbant, the adsorbate atoms lose their valence electrons to the substrate.

The resulting positive ions induce images in the substrate producing a dipole layer which lowers the work function of the surface. This is called electropositive atomic adsorption. A lower work function increases the probability for an incident positive ion (H^+) to be converted to a negative H^- ion.

For Cs/W the work function decreases to a minimum value, $W_\phi \approx 1.5 - 1.6$ eV.

In interaction with a Cs/W surface, H^- ions originate through desorption of hydrogen particles by incident caesium and hydrogen,



or through backscattering of the incident hydrogen



For H^+ ions impacting onto a Cs/W surface at a large incident angle, the H^- yield is maximum ($K_- \approx 40\%$, with K_- the secondary ion emission coefficient) for an energy of $E_\perp \approx 2.5$ eV.

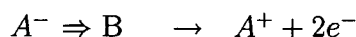
2.2 Negative ion destruction processes

The electron affinity of atoms is very low so an extra electron is easily removed by collisions with various particles and surfaces. The dominate processes for the destruction of negative ions are the following:

1. Photodetachment $A^- + h\nu \rightarrow A + e^-$
2. Electron impact detachment $A^- + e^- \rightarrow A + 2e^-$
3. Atomic (or molecular) collision detachment:

Collision detachment	$A^- + B \text{ (or } B^*) \rightarrow A + B + e^-$
	$A^- + B \rightarrow A^+ + B + 2e^-$
Associative detachment	$A^- + B \rightarrow AB + e^-$

4. Ion collision detachment:



In addition negative ions with very low electron affinity can be detached by strong magnetic or electric fields, e.g. He^- will be detached in an electric field of $E \gtrsim 4.5 \cdot 10^5 \text{ V/cm}^2$. An important destruction mechanism is the charge transfer between a fast negative ion and a slow atom, leading to a slow negative ion and a fast atom. This process is important for the destruction of energetic ions along their paths.

2.2.1 Cross-sections of H^- destruction

The cross-sections of H^- destruction by photodetachment are shown in Figure 2.5. There are two narrow resonant peaks at 10.93 and 10.98 eV, but this process is not important for ion sources.

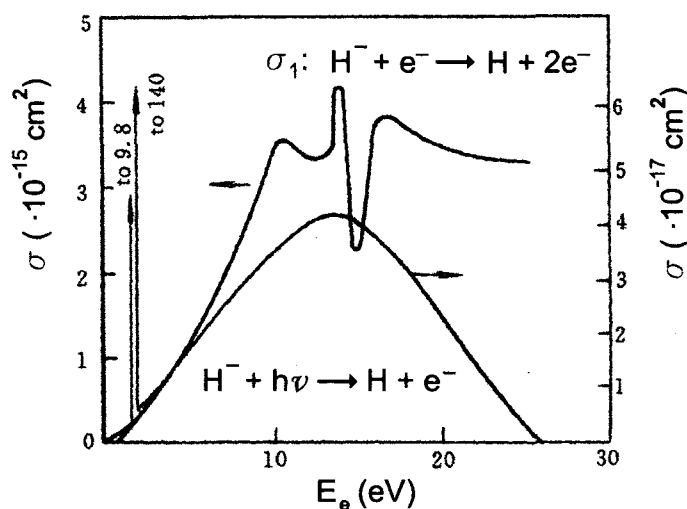


Figure 2.5: The cross sections of H^- destruction by photodetachment and electron impact [120].

The measured cross-sections for electron detachment of H^- ions by electron and particle impact (see Table 2.1) are plotted in Figures 2.5 to 2.7.

The cross-section $\sigma_{-10} = \sigma_1$ for electron detachment has a threshold at $E_e \leq 1.25 \text{ eV}$. Before it was measured there was a resonant peak and a maximum cross-section, σ_{max} , at the electron energy $E_{max} \approx 15 \text{ eV}$, as shown in Figure 2.5. Recently, the cross-section for D^- was measured for energies from 0 to 20 eV and no resonance peak was observed.

$\sigma_1 :$	$H^- + e^- \rightarrow H + 2e^-$
$\sigma_2 :$	$H^- + H^+ \rightarrow H + H^*$
$\sigma_3 :$	$H^- + H \rightarrow H + H^-$
$\sigma_4 :$	$H^+ + H \rightarrow H + H^+$
$\sigma_5 :$	$H^- + H \rightarrow H + H + e^-$
$\sigma_6 :$	$H^- + H_2 \rightarrow H + H_2 + e^-$
$\sigma_7 :$	$H^+ + H_2 \rightarrow H + H_2^+$
$\sigma_8 :$	$H^- + H \rightarrow H_2^- \rightarrow H_2 + e^-$

Table 2.1: The cross sections for electron and particle impact (σ_4 and σ_7 are the charge transfer cross-sections for a proton).

The cross-section σ_6 for H^- destruction by molecular collisions has a maximum $\sigma_{max} \approx 8 \cdot 10^{-16} \text{ cm}^2$, at an energy $E_{max} \approx 10 \text{ keV}$.

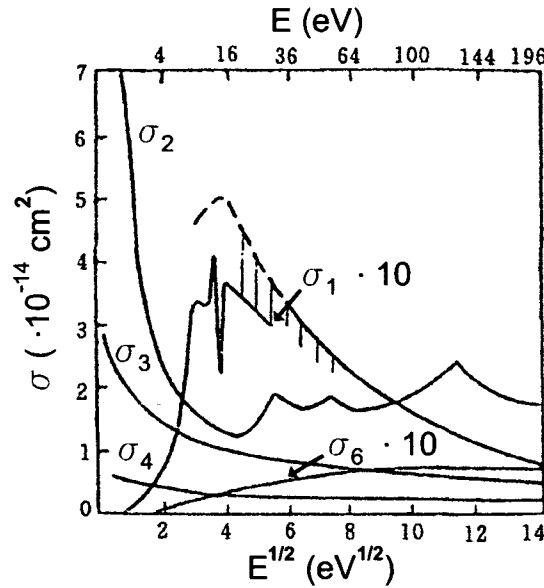


Figure 2.6: H^- detachment by collisions with various particles (for processes $\sigma_1 - \sigma_7$ see Table 2.1) [120].

The cross-section for $H^- + H_2 \rightarrow H^+ + H_2 + 2e^-$ is about $4.5 \cdot 10^{-17} \text{ cm}^2$ for the energy range of 5 – 40 keV.

σ_8 is the reverse process of dissociative attachment, with a suspected cross-section of more than 10^{-15} cm^2 . There could be an isotope effect for this process (It is greater for D^- ions than for H^- ions). It was found that this stripping may be the main loss process in the plasma volume.

Some impurities have large cross-sections for H^- destruction, e.g. the reaction rate $\langle \sigma v \rangle$

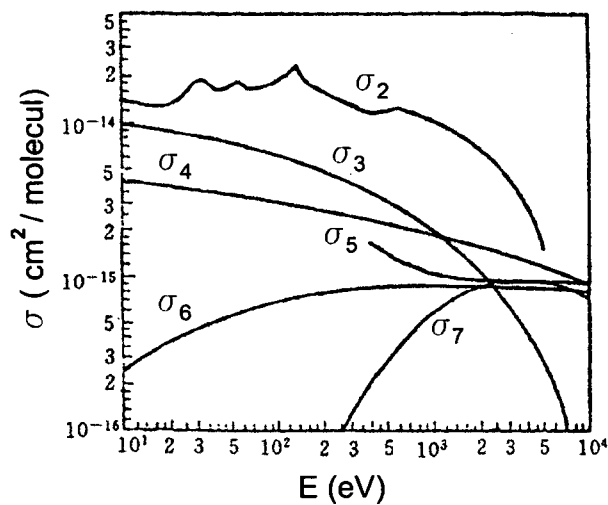


Figure 2.7: H^- detachment by collisions with various particles (for processes $\sigma_1 - \sigma_8$ see Table 2.1) [120].

for $H^- + H_2O \rightarrow OH^- + H_2$ is $\sim 3 \cdot 10^{-8} \text{ cm}^2$ at an H^- ion energy of 2 eV.

The mutual neutralisation (σ_2) increases continuously with decreasing energy, at $E \approx 0.15 \text{ eV}$ it is $2.5 \cdot 10^{-13} \text{ cm}^2$. This is another important loss process in the volume production ion source.

Chapter 3

An overview of H^- ion sources for high intensity accelerators

Accelerators capable of delivering high average power beams (1 MW or more) have many applications. The most demanding projects use high duty factor linear accelerators to reach final beam energies in the GeV range.

In cases where the ion beam must be delivered in short pulses, a favoured technique uses charge exchange injection in a compression ring, requiring the linac to accelerate a negative ion beam. A summary of the latest source specifications for high intensity accelerator projects is given in Table 3.1 [89].

	Current [mA]	Pulse Length [ms]	Repetition Rate [Hz]	Duty Factor	Average Current [mA]	Emittance ^a [$\pi \cdot \text{mm} \cdot \text{mrad}$]
LINAC4 [75]	50	0.5	2	0.1 %	0.05	0.25
SPL [75]	>40	2.8	50	14 %	5.6	0.25
ESS [31]	65	1.2	50	6 %	3.9	0.3
SNS [118]	50	1	60	6 %	3	0.2
JKJ [76]	30	0.5	50	2.5 %	0.75	N/A

^a1rms, normalised

Table 3.1: H^- ion source parameters required for selected high power projects (SPL – Superconducting Proton Linac, ESS – European Spallation Source, SNS – Spallation Neutron Source, JKJ – Joint KEK Jaeri).

The mixture of high current and high duty factors is a challenge for source engineers. The high beam powers require stable beam parameters, often with small emittances and delivered with very high reliability.

H^- ion sources presently deliver high currents or high duty factors. However, average H^- ion currents are presently below 10 mA.

The processes leading to the generation of H^- ions are explained in Chapter 2, more in

depth discussion of the different source types can be found at [29, 119, 120]. Excellent reviews of the upgrade history have been reported by Peters [80, 81, 82]. The data given below is summarised in Table 3.2.

3.1 Operational characteristics of selected H^- ion sources

3.1.1 Filament multicusp H^- ion sources

Using a multicusp magnetic arrangement, a plasma can be produced by a discharge from a cathode or a filament to the chamber wall. The H^- ions are either produced on the chamber surfaces or in the plasma volume. Most sources report that the H^- ion current increases proportional to the discharge power.

The highest performance accelerator source of this type was built at the Institute of Applied Physics (IAP) [113] in Frankfurt in anticipation of the European Spallation Source project. Running at the same 6 % duty factor as the SNS project source, this filament multicusp source has in comparison demonstrated higher average currents (120 mA pulsed, leading to an average current of 7.2 mA).

The IAP source uses multiple filaments of 1.8 mm diameter tungsten wire, and has been run for 190 hours with the 6 % duty factor. The tungsten erosion suggests that the lifetime of the source would be ~ 14 days before the filaments require changing.

The source relies on caesium seeding of the plasma by an oven, which delivers caesium into the outlet aperture region. The controlled release of caesium is required every 10–18 hours.

The H^- ion yield has been demonstrated to vary almost linearly with the arc discharge power up to 50 kW. No saturation of this has yet been seen, so higher currents appear not to be limited by fundamental processes in this source, but rather by the arc power supply and the cathode lifetime.

The IAP source has not been in operation since 1998 and there are presently no plans to change this situation.

At the Los Alamos Neutron Science Center (LANSCE) [67], the filament multicusp source includes a caesium coated molybdenum converter, to produce H^- ions by surface conversion. 18 mA of H^- ions are extracted radially into an emittance of $0.13 \pi \cdot \text{mm} \cdot \text{mrad}$ at 12 % duty factor. The tungsten filaments have to be replaced every 28 days [88].

Full CW operation, without caesium, is achieved at the TRI-University Meson Facility (TRIUMF) [64, 110] in Vancouver, Canada and the University of Jyväskylä, [47, 59], Finland with currents of 6 and 1.5 mA respectively.

A pulsed low duty factor source, without caesium, is in operation for the JOINT KEK JAERI (JKJ) project [76, 111], Japan, producing 38 mA of H^- ions at less than 1 % duty factor.

Lifetimes of the sources range from 200 to 600 hours due to erosion of the filaments by ions falling through the cathode sheath potential.

The production efficiency of the non-caesiated sources is 1.1 – 1.4 mA/kW while the pulsed IAP source, with caesium, has a factor 2 greater efficiency.

3.1.2 Magnetron H^- ion sources

Magnetron ion sources consist of a central cathode surrounded by an anode, which is immersed in a magnetic field along the cathode axis. The negative ions are produced from the caesiated cathode surface, and are accelerated through the cathode sheath potential. Charge exchange with neutral hydrogen in the plasma can lead to the production of a lower energy component of H^- ions in the plasma, which leads to a larger beam emittance.

Magnetrons are used for the H^- ion production of beams with 0.5 % duty factor or less at the Argonne National Laboratory (ANL) [4], the Brookhaven National Laboratory (BNL) [16] and Fermilab (FNAL) [28], all in the USA, and at DESY. Between them the magnetron has more than 80 years of operational experience. In all cases the magnetron sources were able to satisfy the requirements of the accelerators, and in most cases they run at the space charge limit of the extraction.

All sources manage to provide beams for 6 – 9 months per year before requiring a dismounting and cleaning, usually being shut down rather than failing. A failure of the source is usually attributed to:

- A build-up of caesium hydride near the Cs inlet or on the pulsed gas valves.
- The flaking of the cathode material, either shorting the anode and cathode, or blocking the source outlet.
- A caesium oven heater failure.
- Extraction sparking.
- A pitting of the cathode surface.
- Contamination.

It is not clear if higher duty factors would significantly increase these failure rates. If they increase the caesium consumption, this may decrease the time between the failures mentioned above.

All four source species use an extraction voltage of 35 kV or less, so the higher field gaps required for future accelerators may be an issue.

Although extraction through a slit aperture is common, Brookhaven has used a circular aperture since 1989. This has increased the H^- ion production efficiency from 6.7 to 67 mA/kW, although the source presently runs at 36 mA/kW [2].

To increase the duty factor of 0.5 % by a factor 10 or more would have implications not only for the heat load, but for the pulsed gas injection and the caesium coverage of the cathode as well. Presently, the caesium coverage is probably maintained by condensation during the off-cycle, while the atoms are sputtered away by incoming H^+ ions during the discharge. A porous cathode could allow caesium to seep through the cathode body to the surface, as demonstrated by Alessi et al. [1]. However, there is at the moment little active research on increasing the duty factor of Magnetron H^- ion sources.

3.1.3 Penning H^- ion source

The Penning H^- ion source uses a discharge with a hollow anode capped with cathodes at each end, along the magnetic field. The ions are extracted through a slit in the anode. As for magnetrons, a caesium layer on the cathode is bombarded by H^+ ions and can emit H^- ions. In contrast to the magnetron source, these ions are not directly aimed at the extraction aperture, therefore the additional electron has to be attached to an H atom which may then be extracted as an H^- ion. The energy distribution of the H^- ions is thus from the plasma alone, without a direct contribution from the cathode surface. This results in a lower emittance beam when compared to magnetron sources.

Existing sources are running at high currents and medium to full duty factors.

The ISIS penning source [54, 108] at Rutherford is based on a Los Alamos design and is able to run for 50 days at 1 % duty factor, delivering 35 mA of H^- ions, before the source has to be changed.

Rutherford have available a full development rig and hope in the near future to improve the source cooling and upgrade the power supplies to provide 1.2 and 2.5 ms pulses with a higher extraction voltage.

The medical source of the Budker Institute of Nuclear Physics (INP) [53], Russia, with 8 mA of H^- ions CW, runs during working hours for 3 weeks before more caesium has to be added, equating to approximately 150 hours [14].

At the Los Alamos National Laboratory (LANL) [68], sources were designed and constructed applying plasma scaling laws and increasing two of the source dimensions by a factor of 4 (the 4X source), which reduced the cathode power load from 16.7 to 2.24 kW/cm², while increasing the H^- ion current from 160 to 250 mA [91, 94].

The emittance product $\epsilon_x \cdot \epsilon_y$ increased by a factor 3, but the increase was not distributed to the x and y emittances with the same ratio as the increase in outlet slit apertures, with the emittance ϵ_y being slightly larger than the value demanded for most high power accelerators. It is further suggested that this 4X source could run at 5 % duty factor and 105 mA H^- ion current while keeping the source life time to about 2 months. In tests, the discharge was successfully maintained at 6 % duty factor without extraction. Ion current measurements with a circular aperture result in an appreciable decrease in the average current density.

LANL also developed an 8X source with hot water cooling of the cathode and anode close to the discharge surfaces, based on the same scaling as the 4X source. Initial pulsed operation is reported in [95], however full CW operation was never achieved due to funding limitations.

Penning sources with slit extraction have an H^- ion production efficiency of 8 - 12 mA/kW, which primarily heats the small surface area of the cathode and anode. To extend the performance to higher duty factors with high currents, three main issues have to be solved: Reducing the power per area unit on the source electrodes, sufficiently cooling the electrodes and maintaining a coating of caesium on the cathodes.

3.1.4 RF driven multicusp H^- ion sources

At DESY [27], Germany, at Lawrence Berkeley National Laboratory (LBNL) [69], California (for SNS) and at Seoul National University (SNU) [96] the development of RF sources has continued for the production of low to full duty factor beams.

Using an antenna, electrons present in the gas volume are excited into oscillations by the RF electric field, quickly acquiring enough kinetic energy to form a plasma by ionising the background gas particles.

The lifetime of RF sources is limited by sputtering of the antenna surface, as it is exposed to the plasma. For several years, different metal materials were tried for the conducting antenna (which typically is hollow for water cooling) and different surface treatments with insulating materials. The most promising, using less than a millimeter of porcelain, produced average operational lifetimes of ~ 1000 hours at DESY.

Although in the later part of the 1990's the SNS and DESY source designs were very similar, DESY has since made a break-through in reliability, by insulating the antenna from the plasma with a thick Al_2O_3 cylinder [79]. This external antenna source has now delivered 40 mA of H^- ions, at a pulse length of 100 μs at 5 Hz for 25000 hours, without caesium enhancement, using an RF power of 20 kW. The performance of the source is presently limited in current, pulse length and duty factor by the RF power supply.

The SNS source also uses a pulsed radio frequency of 2 MHz, of up to 50 kW, which is coupled to the plasma by a porcelain enamel coated antenna. Continuous, low power RF at 13.56 MHz is supplied to facilitate the ignition of the plasma.

With caesium enhancement – provided by caesium chromate inside a heated collar – the source has produced 50 mA H^- ion beams with a duty factor of 6 %, but is still in testing stage to produce this beam in an operational manner and with high reliability [118]. Without caesium, the source has produced 15 mA of H^- ions.

The source is currently providing beams for the commissioning of the SNS RFQ, with operation at low duty factor from 2006. In the future, a design with an external antenna will be tried for high duty factors.

The SNU source uses 13.56 MHz radio frequency, delivered by an antenna behind a quartz or alumina window, allowing the antenna to be completely separated from the plasma. In CW operation, the source provides 0.2 mA of H^- ions at 20 kV with no caesium addition. Previously higher currents were claimed [51], but measurements appear not to have fully suppressed the electron current.

The H^- ion production values are highly variable with values of 2, 1 and 0.13 mA/kW for the DESY, SNS and SNU sources, suggesting that the configurations of the SNU and even the SNS source might still be improved.

3.1.5 ECR H^- ion source

Energetic electrons gyrate in a magnetic field B with a frequency ω_c defined by the relation

$$\omega_c = \frac{eB}{m_e}, \quad (3.1)$$

or in engineering units at 28 GHz/T. In a box immersed in an arbitrary magnetic field there can exist a surface where the above relationship (3.1) holds.

If power of this frequency is injected into the box, plasma electrons crossing this surface will, in general, be heated and can be used for ionisation of the plasma.

The ECR (Electron Cyclotron Resonance) ion source (ECRIS) makes use of this effect using microwave frequencies, injected either by an antenna or a waveguide. Longitudinal confinement is achieved by Helmholtz coils configured to give a 'minimum B' field configuration. Powerful permanent magnet multipoles, usually a hexapole, provide radial confinement and MHD stability of the plasma [36]. For a microwave frequency of 2.45 GHz Equation (3.1) corresponds to a flux density of 0.0875 T.

With a production efficiency of more than 100 mA/kW and no cathode, highly reliable 2.45 GHz ECR plasma heating proton sources have been demonstrated with the SILHI source [42] at the Commissariat à l'Energie Atomique (CEA) [22], Saclay, France, with TRIPS – Trasco Intense Proton Source – at Catania [20, 21] and at LANL [90].

With the success of the CW proton beam sources, development of these sources for the production of H^- ions is of great interest.

The H^- ion sources at CEA/Saclay (2 mA, duty factor 2 %, 1.2 kW discharge power) [42], ANL (4 mA, CW, 2 kW discharge power) [98] and TRIUMF [58] (2.1 mA, CW, 0.5 kW discharge power) have all produced beams.

CEA and ANL both use 2 solenoid field configurations, while TRIUMF uses a multicusp arrangement with some magnets inverted to produce a magnetic filter.

TRIUMF reached a production efficiency of 4 mA/kW and has run continuously for 1 month with only a vacuum gauge failure.

Magnetically filtered multicusp volume sources

In a strict way of speaking, the sources mentioned above are not real ECRIS, since they use either solenoids or a multicusp structure. In fact a better definition would be microwave-driven source or tandem source, if a magnetic filter is used [120].

This filter provides a limited region of transverse magnetic field ($\int Bdl \lesssim 10^{-4}$ T·m) and divides the source into two chambers, the plasma or source chamber and the extraction chamber.

The magnetic filter is strong enough to prevent all energetic primary electrons in the plasma region from entering the extraction region. However, both positive and negative ions together with cold electrons can penetrate the filter (see Figure 3.1).

Due to the confinement of the magnetic filter, a relatively large concentration of fast electrons ($E_e > 10$ eV [19]), which are very effective for the formation of vibrationally excited hydrogen molecules, is formed in the plasma region (see Chapter 2).

On the other hand, in the extraction region, the low temperature electrons with $kT_e \lesssim 1$ eV are favoured for dissociative attachment to the vibrationally excited hydrogen molecules ($5 \leq \nu'' \leq 11$) (see Chapter 2) and not significant for H^- ion destruction (see Chapter 2.2). Thus a plasma with a high H^- fraction of 40 – 70 % and low negative ion temperature of $\sim 0.1 - 0.7$ eV can be formed in the extraction region.

An explanation of the operation of the magnetic filter might be based on the classical diffusion governed by Coulomb collision [93, 112]. The plasma electron diffusion coefficient perpendicular to the magnetic field, D_\perp , is given by:

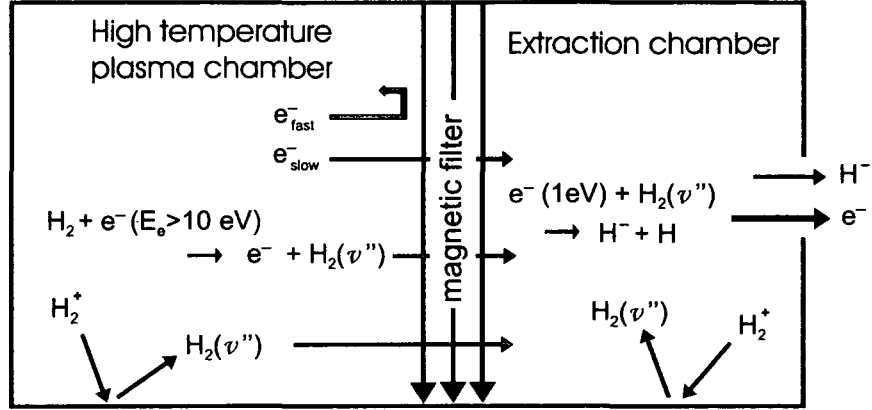


Figure 3.1: Scheme of a tandem source for volume production.

$$D_{\perp} = \frac{8}{3\pi} \frac{kT_e \nu}{m_e (\omega_c^2 + \nu^2)} \quad (3.2)$$

where ν is the total collision frequency. In a dense plasma ($n_e > 10^{11}/\text{cm}^3$) and at low pressures ($p < 5 \text{ mTorr}$), Coulomb collisions dominate the total elastic electron collision, so

$$\nu = K n_e T_e^{-\frac{3}{2}}. \quad (3.3)$$

In the high field limit, when $\omega_c \gg \nu$, the plasma is strongly affected by the magnetic field, and

$$D_{\perp} = \frac{8}{3\pi} \frac{kT_e \nu}{m_e \omega_c} \propto T_e^{-\frac{1}{2}}. \quad (3.4)$$

Thus the hot electrons are subject to a low diffusion coefficient relative to the cold electrons.

The plasma transport equation was used to derive the exact effect of the filter. The results show that T_e decreases exponentially through the filter, and does not become constant in the extraction region.

	Op.	Type	Current ^a [mA]	Pulse Length [ms]	Repetition Rate [Hz]	Duty Factor	Discharge [kW]	Eff. [mA/kW]	Extr. [kV]	$\epsilon_{x,y}$ ^b [π -mm-mrad]	Caesium [mg/day]	Lifetime [h]
ANL	✓	Mg	48/0.1	0.07	30	0.21 %	7	6.9	20	0.22, 0.35	5	2100
BNL	✓	Mg	90/0.47	0.7	7.5	0.525 %	2.5	36	35	0.27	12	4368
CEA		E _{2.45GHz}	2	2	5	2 %	1.2	1.2	9	N/A	-	N/A
DESY (RF)	✓	RF _{2MHz}	40/0.025	0.1	5	0.05 %	20	2	35	0.18, 0.16	-	25000
DESY (Mg)	✓	Mg	60/0.027	0.075	6	0.045 %	N/A	N/A	18	0.38, 0.29	2	6384
FNAL	✓	Mg	60/0.06	0.066	15	0.1 %	10	6	18	0.33	✓	2000
IAP		FI MC	120/7.2	1.2	50	6 %	47.5	2.5	33	0.07	50	190
INP		P	8	-	-	CW	0.63	12.7	23	0.3	40	140
INR-MMF	✓	P	80/2	0.25	100	2.5 %	N/A	N/A	20	0.15	24	336
ISIS	✓	P	35/0.35	0.2	50	1 %	4	8.8	18	0.12, 0.17	0.1	1200
JKJ		FI	38/0.34	0.36	25	0.9 %	35	1.1	50	0.1	-	100
Jyväskylä	✓	FI	1.5	-	-	CW	1.1	1.4	5.8	N/A	-	200
LANL		P-1X	160/0.8	1	5	0.5 %	18	8.9	22	0.17	✓	N/A
LANL		P-4X	170/0.85	1	5	0.5 %	19.8	8.6	29	0.29	✓	N/A
LANSCE	✓	FI MC ^c	18/2.2	1	120	12 %	N/A	N/A	N/A	0.13	110	670
LANSCE		FI MC ^d	40/4.8	1	120	12 %	10	4	80	0.35	✓	N/A
SNS		RF _{2MHz}	50/3.9	1.3	60	8 %	50	1	65	0.17	≤1	110
SNU		RF _{13.56MHz}	0.2	-	-	CW	1.5	0.1	5	N/A	-	100
TRIUMF (FI)	✓	FI	6	-	-	CW	5	1.2	25	0.163	-	600
TRIUMF (E)		E _{2.45GHz}	2.1	-	-	CW	0.5	4.2	N/A	0.25	N/A	720

^aAverage over the pulse length / Time average^bI_{rms}, normalised^cRadial source with a converter.^dAxial source with a converter, not yet in operation.

Table 3.2: Parameters of selected H^- ion sources (Op. – operational on an accelerator, Eff. – Efficiency, RF – Radio frequency, MC – Multicusp, FI – Filament, Mg – Magnetron, P – Penning, E – ECR, Extr. – Extraction voltage).

3.2 Selected H^- ion sources and the LINAC4/SPL requirements

The main requirements on the LINAC4 and the SPL H^- ion source(s) are given in Table 3.1 and more detailed in Table 1.1. As can be seen in Figure 3.2, there are already a few sources, both operational and others dedicated to research, that would fulfill the requirements of LINAC4.

There is at the moment no source meeting the SPL project specifications, with the SNS and IAP sources coming nearest. However, since the IAP source has not been operational for a few years and also used a filament, the SNS source is the only real option.

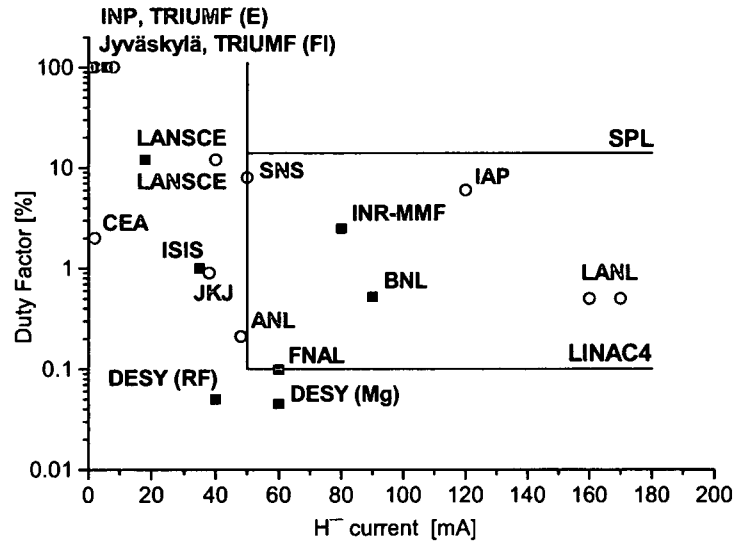


Figure 3.2: The duty factor versus the maximum current of present H^- ion sources (■ operational, ○ research) and the requirements of the LINAC4/SPL project (blue).

Another important feature of the future LINAC4/SPL source is its reliability. The product of average H^- ion current and source lifetime (see Figure 3.3) might be an indication of the reliability of the different sources, with the TRIUMF source with 3600 mA·h the most promising.

The BNL magnetron delivers 2100 mA·h (see Table 3.3), but DESY (500 mA·h), being very good with respect to lifetime but lacking the duty factor, and SNS (420 mA·h), with a lifetime of only 110 hours, are further in the back of the field.

Taking into account the above data, for LINAC4 two H^- ion source types might be feasible:

The first one is the BNL magnetron, with almost all its parameters in LINAC4 range and exceeding them in current and repetition rate. Additional positive points are the proven reliability of 6 months and the experience with oven heaters at CERN. Work would have

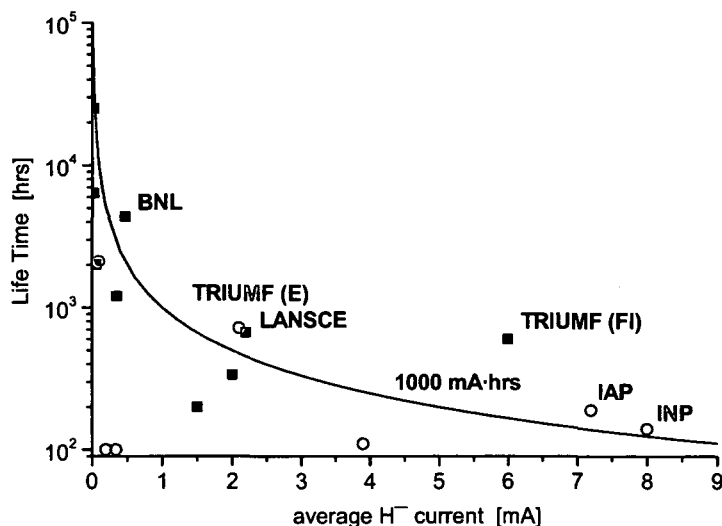


Figure 3.3: The average current times the source lifetime as an indication of the reliability of present H^- ion sources, with the 1000 mA·h line (blue).

to be done to reduce the emittance a little, to learn the Cs handling and to change the extraction voltage to 95 keV.

	TRIUMF (F1)	BNL	TRIUMF (E)	IAP	LANSCE	INP	DESY (RF)	SNS	ISIS
mA·h	3600	2100	1500	1400	1200	1100	500	430	420

Table 3.3: The average current times the source lifetime as an indication of the reliability of present H^- ion sources.

Another possibility would be a RF multicusp source, either SNS or DESY. The SNS source works at a higher duty factor, while DESY, with its proven 3 years reliability, is operating caesium-free. The pulse structure would have to be modified to increase the duty factor and working with 2 MHz RF technology has to be learned in both cases.

Chapter 4

Experimental setup

The core of the source is the water-cooled plasma chamber, a stainless-steel cylinder with 10 cm inner diameter and 20 cm length. Following the principles of H^- volume production in a tandem source (see Chapter 2 and 3.1.5) a magnetic filter consisting of two permanent magnets is used for the separation of the plasma chamber into the plasma- and the H^- production-region near the plasma electrode (see Figure 4.1). The filter is placed 7.8 cm away from the plasma electrode with a maximum flux density of ~ 0.007 T between the two magnetic rods (increasing towards the magnets).

The microwave of a frequency of 2.45 GHz and a maximum power of 1.5 (1.2) kW¹ (pulsed) is injected with a movable straight antenna (see Chapter 4.2).

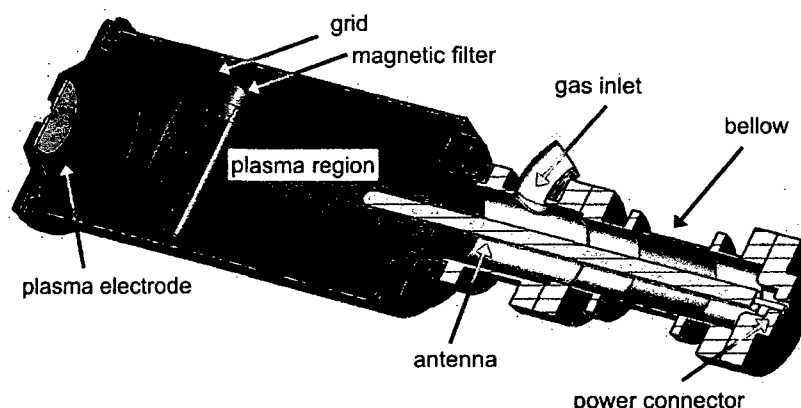


Figure 4.1: Schematic view of the source.

The source and its support systems, such as microwave and gas injection, cooling system and the power supplies for the solenoids, are held at negative high voltage inside a secured high voltage cage. The power for the components is delivered by a 3 kW transformer.

For extraction a two electrode system is used. A 100 kV power supply delivers a constant high voltage. 20 kV are used for all the measurements because of stability reasons (voltage drop for a high load on the power supply).

The plasma electrode is insulated with respect to the plasma chamber and can be biased up to a voltage of ± 60 V, the diameter of the extraction hole is 5 mm.

¹Maximum power changed due to a replacement of the magnetron

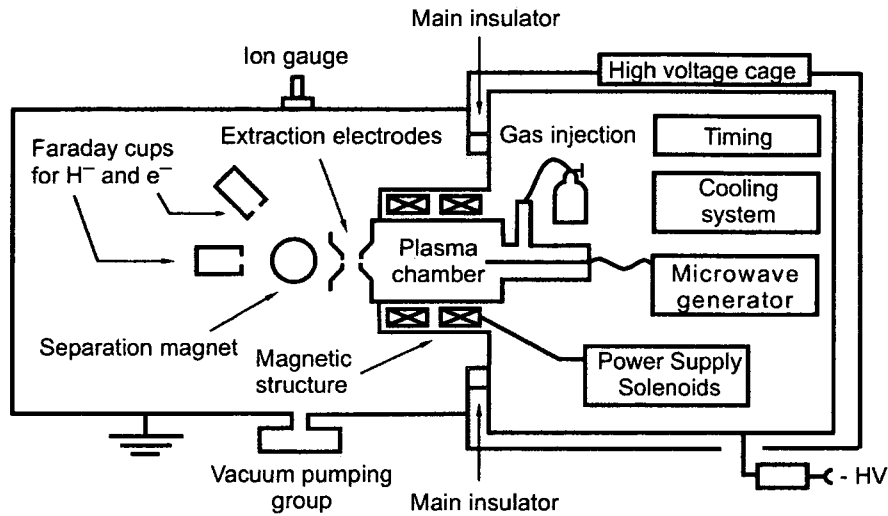


Figure 4.2: The experimental setup.

Both the source and the extraction system with the subsequent spectrometer for the e^-/H^- separation (see Chapter 4.3) are housed inside a ~ 160 l vacuum tank. A 600 l/s turbo molecular pump achieves pressures of $7 \cdot 10^{-8}$ mbar without hydrogen gas flow, measured at the ion gauge ~ 40 cm away from the extraction hole. To avoid contamination the tank can be vented with pure nitrogen.

The hydrogen gas is injected at the antenna side of the source, with flow rates of up to 12 ml/min. An additional mass flow controller allows the injection of secondary gases. For efficient pumping of the gas-injection line after a system vent the source can be bypassed, but there is no differential pumping between source and tank during operation. Three different magnetic structures – multicusp, solenoids and solenoids with multicusp – can be installed between the cooling pipes of the plasma chamber and the outer shell of the source (see Figure 4.2 and Appendix A).

4.1 Magnetic field configurations

4.1.1 Multicusp structure

For the first experiments a configuration of 10 permanent magnet columns around the plasma chamber was used (see Figure 4.3), surrounding only the plasma region behind the magnetic filter. The 50 permanent magnets with a dimension of $6 \times 10 \times 30$ mm, type SMCO-2:17, provide a magnetic flux density of 0.29 T at the magnet position inside the plasma chamber, if they are kept in place by a thin iron cylinder (0.21 T with anticylinder). This is not enough for the 0.0875 Tesla ECR surface of the individual permanent magnets to interconnect with each other inside the plasma chamber (see Figure 4.4).

Simulations of the magnetic structure were done both with POISSON SUPERFISH [66] and ANSYS [5], showing good correlation.

For later measurements the 10 permanent magnet rods were extended to surround the production region of the plasma chamber as well. The motivation was to increase the suspected low electron density in the production region.

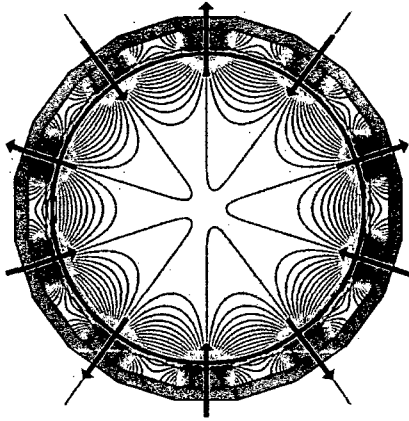


Figure 4.3: Orientation of the permanent magnets and the resulting magnetic field-lines [SUPERFISH] (with surrounding iron cylinder).

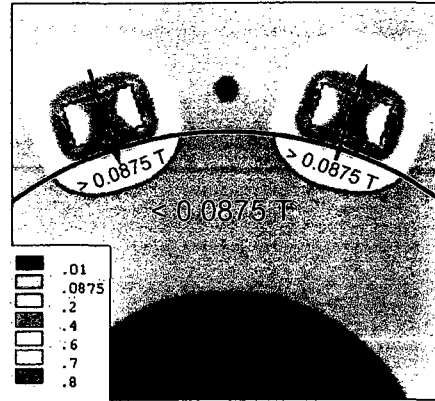


Figure 4.4: Field structure near the magnets of the multicusp structure [ANSYS] (without surrounding iron cylinder). The resonance surface is emphasised.

4.1.2 Solenoidal structure

The multicusp structure was replaced by two solenoids, since the higher magnetic flux density and hence expanded 0.0875 Tesla surface were expected to increase the electron density and therefore the H^- beam current. The solenoid nearer to the microwave input is named Solenoid 1, the solenoid nearer to the extraction Solenoid 2.

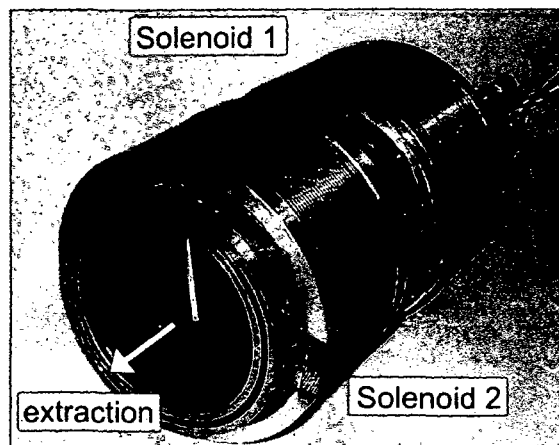


Figure 4.5: The source body with the magnetic filter and the two solenoids.

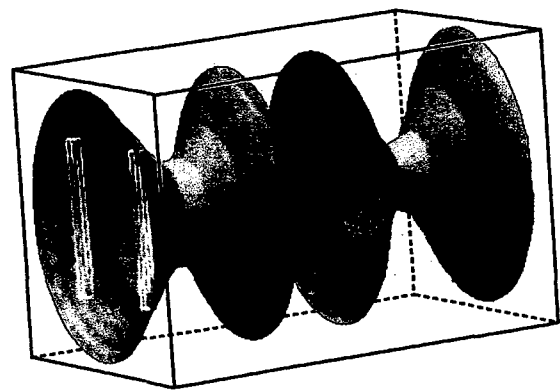


Figure 4.6: The surface of 0.0875 Tesla flux density of the two solenoids at a current of 22 A [ROXIE].

The limited available space for the integration of the coils and the necessity for a magnetic flux density (see Equation (4.1)) higher than 0.0875 T on axis made the design of the solenoids difficult.

For both the solenoids and the e^-/H^- separation coils (see Chapter 4.3) the magnetic flux density on the center axis x for two solenoids with distance b , current I and N windings can be derived from the Biot Savart law with

$$B(x) = \frac{1}{2}\mu_0 N I R^2 \left(\frac{1}{\sqrt{R^2 + x^2}^3} + \frac{1}{\sqrt{R^2 + (x-b)^2}^3} \right) \quad (4.1)$$

with μ_0 as the magnetic field constant.

For an inner coil diameter of 114 mm and a maximum thickness of 18 mm the conventional solenoid design with hollow pipes for water cooling demands a current of more than 400 A (see Table 4.1).

	layers	turns	d [mm]	R_{Sol} [mm]	I [A]	B [T]	P [kW]
Pipe	3	40	4 x 4	65	430	0.17	4.8
Wire	9	380	1 x 2	67	40	0.16	2.2

Table 4.1: Main parameters of the solenoids for two different types of wiring.

To keep the demands on the power supplies for the two solenoids reasonable and to avoid a replacement of the 3 kW voltage transformer, the use of water-cooled pipes was abandoned and the number of turns increased by using capton insulated 1 x 2 mm copper wire.

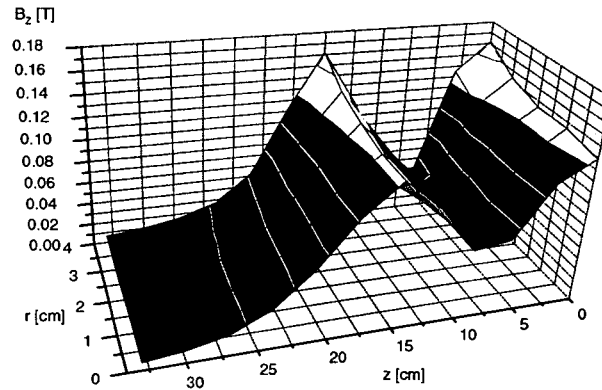


Figure 4.7: Magnetic flux density B_z of the two solenoids at a current of 41 A.

To provide sufficient cooling the pulsed operation of the two solenoids is thus inevitable. With a duty cycle of 1 % the average power is about 20 Watt, low enough for the only marginal thermal contact between the solenoids and the cooling pipes of the plasma chamber. To reduce the magnetic field strength in the production region and between the two solenoids, iron rings of variable thickness for the different coil positions can be added (see also Chapter 4.1.3). In the case of the pure solenoidal structure iron rings of a

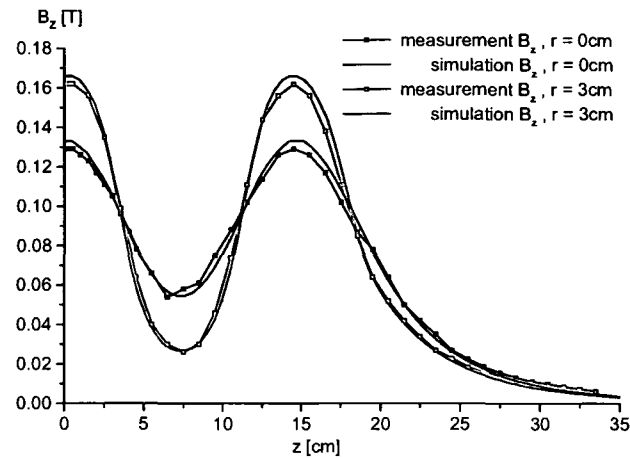


Figure 4.8: Comparison of simulated and measured magnetic flux density of the two solenoids at a current of 41 A, a distance of 6 cm between them.

total width of 3.1 cm were placed around the H^- production region in front of Solenoid 2, 3.4 cm of iron between the solenoids and 1 cm behind Solenoid 1.

Exact knowledge of the position of the 0.0875 T ECR surface is essential, especially for the solenoid nearer to the production region (see Figure 4.6 and 4.7). The correlation between field measurements and simulation is very good (see Figure 4.8).

4.1.3 Combination of solenoidal and multicusp structure

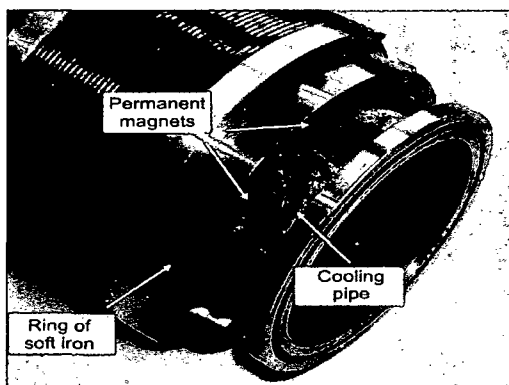


Figure 4.9: Extraction region of the source body with cooling pipes, permanent magnets with the supporting iron rings and Solenoid 2.

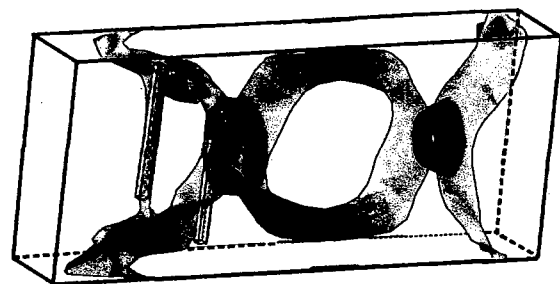


Figure 4.10: Cut through 0.0875 Tesla surface of the two solenoids at 22 Amperes together with the permanent magnets [ROXIE].

Both the solenoids and the iron rings are equipped with slots to install the permanent magnets, allowing a combination of the two field types (see Figure 4.9).

It is noteworthy that the inclusion of the iron rings also changes the field of the permanent magnets. In the case of turned-off solenoids the resulting multicusp field cannot be compared to the multicusp field without the iron rings of Chapter 4.1.1.

Iron rings with a total width of 2.4 cm were placed around the H^- production region in front of Solenoid 2, 4.1 cm between the solenoids and 1.4 cm behind Solenoid 1.

Again 3D magnetic field simulations were done (see Figure 4.10), using the program ROXIE [65], showing the influence of the magnetic filter and the drop below a flux density of 0.0875 T between the permanent magnets.

4.2 Microwave-system

The H^- source is a 2.45 GHz microwave driven source. The microwave system is designed for a maximum power of 1 kW DC, but in the end a pulsed magnetron of 1.5 (1.2) kW maximum power was used.

The main parts (see Figure 4.11) of the microwave system are the microwave generator (magnetron), followed by a circulator for the protection of the generator, which directs the reflected power to a 1 kW DC load. A 40 dB dual directional coupler allows the simultaneous measurement of forwarded and reflected power with two Schottky diode detectors. For their protection, two 20 dB attenuators are installed.

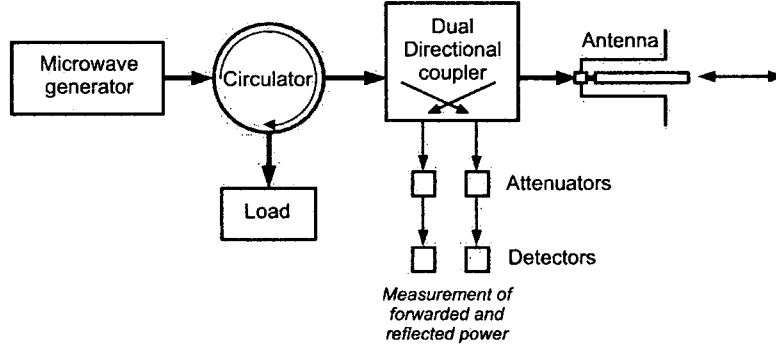


Figure 4.11: The setup of the microwave components.

For microwave injection into the source a movable straight antenna is used to allow easy tuning of the source. The total antenna length is $2 \cdot \lambda_{2.45 \text{ GHz}}$, the range of the antenna tip into the plasma chamber is $\sim \lambda_{2.45 \text{ GHz}}/4$, with $\lambda_{2.45 \text{ GHz}} \sim 12.24 \text{ cm}$, to simulate a quarter wave vertical antenna. For free antenna movability cables with 7/16 connectors replace the commonly used waveguides.

The calibration of the two detectors was done both with a pulse generator and a network analyser at 2.45 GHz, showing the expected identical behavior of the detectors. The polynomial fit between the detector output U_{Det} and applied power P_{mw} (see Figure 4.12) for U_{Det} higher than 50 mV is then given by

$$P_{mw}[\text{W}] = -31.82401 + 1.1391 \cdot U_{Det}[\text{mV}] + 0.01804 \cdot U_{Det}^2[\text{mV}] \quad (4.2)$$

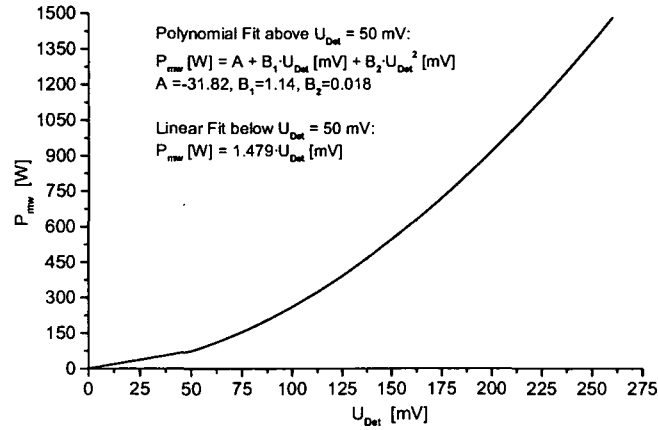


Figure 4.12: Calibration of the detectors.

Below 50 mV a simple linear fit with $P_{mw} [W] = 1.479 \cdot U_{Det} [mV]$ is used.

The comparison of the calibration and the actual output of the microwave system with the two magnetrons (see Figure 4.13) shows that the delivered power is in general lower than the expected calibration value, due to the losses in the cables and connections, and that the power delivered by the magnetrons is not straight proportional to the applied control voltage. The maximum delivered microwave power of the 1.2 kW magnetron is only 1.1 kW.

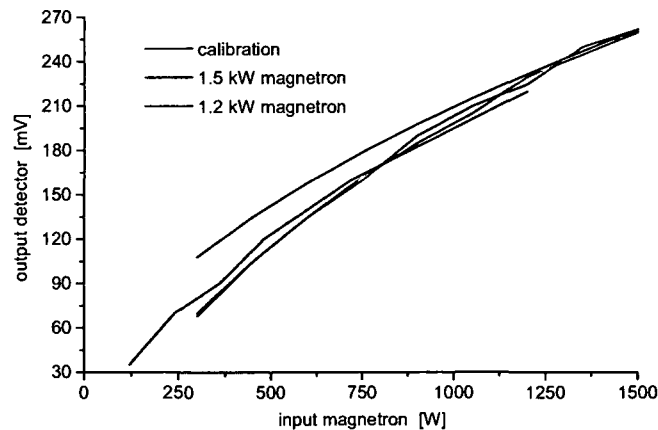


Figure 4.13: Theoretical and measured values of the magnetron output.

4.2.1 Microwave transition

The response of the actual plasma chamber to the microwave injection was studied with some simulations in MICROWAVE STUDIO [26]. Figure 4.14 shows the layout and the distribution of the electric field at the beginning of the straight antenna, near the transition point of the microwave into the vacuum.

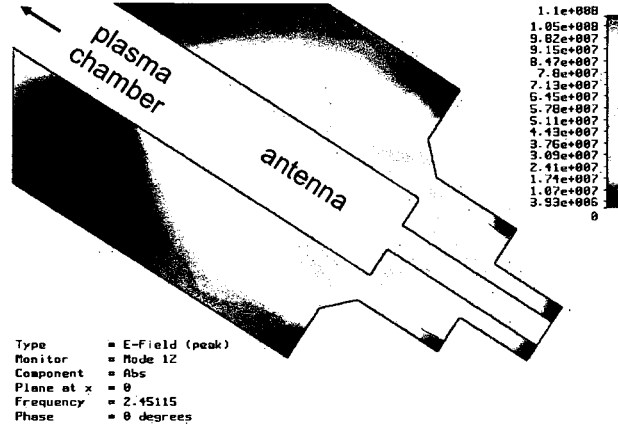


Figure 4.14: The layout of the antenna mounting and the resulting electric field (Absolute electric field values arbitrary, $z = 30$ mm).

Figure 4.15 shows the calculated S_{11} parameter of the plasma chamber and the measurements of the S_{11} parameter are shown in Figure 4.16.

Marker 1 is at the generator frequency of 2.45 GHz, which is not a prominent eigenmode, leading to a high reflected power. Markers 3 and 4 are positioned at the two most prominent eigenmodes at 2.38 GHz and 2.65 GHz, corresponding well to the simulations (compare to Figure 4.15), which also predicted a smaller eigenmode at 2.32 GHz.

A promising approach to optimise the microwave power insertion might be a reduction of either the inductance or the capacitance of the cavity to move the 2.38 GHz eigenmode to 2.45 GHz.

4.2.2 Improved microwave transition

A main factor prohibiting a DC operation of the source is the heating of the connection between coaxial cable and the antenna, therefore the heating of the power feed-through into the vacuum.

This heating might be a consequence of the large variations in inner and outer conductor diameter (see Figure 4.14), with impedances ranging from 25 to 100 Ω .

By insertion of a taper and changes in the antenna layout (compare Figures 4.14 and 4.17) a reduction of the heating and an increase in the microwave transmission was intended. Using the formulae

$$Z = \left(\frac{138}{\sqrt{\epsilon_r}} \right) \log \left(\frac{r_o}{r_i} \right) [\Omega] \quad (4.3)$$

with the impedance Z , ϵ_r the dielectric constant and r_o and r_i the outer and inner conductor radius, and

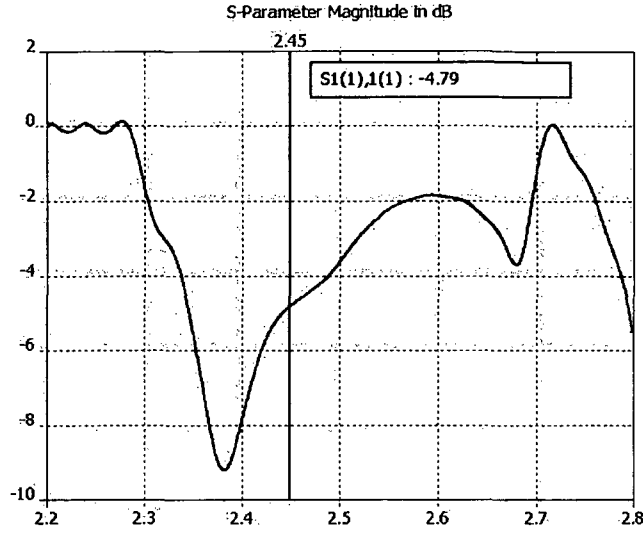


Figure 4.15: Simulation of the S_{11} parameter of the plasma chamber (Marker at 2.45 GHz, $z = 30$ mm).

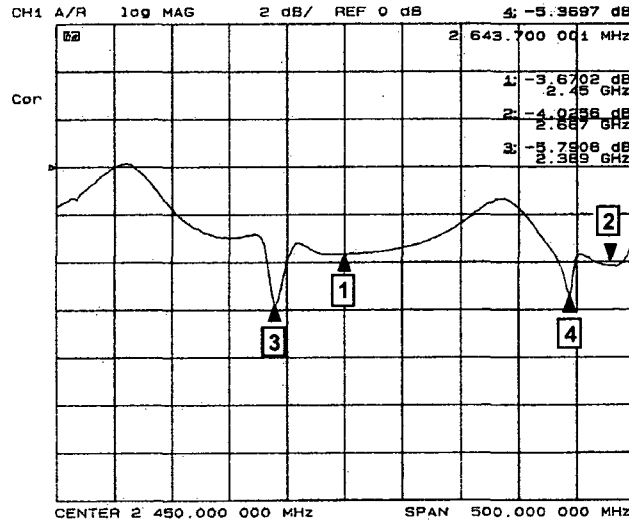


Figure 4.16: Measurement of the S_{11} parameter of the plasma chamber (Marker 1 at 2.45 GHz, $z = 30$ mm).

$$\Gamma = \frac{Z_L - Z_0}{Z_L + Z_0}, \quad (4.4)$$

with Γ the reflection coefficient, a smoother transition from the 50Ω impedance of the coaxial cable to the 75Ω impedance of the antenna channel was created. The changed conductor diameters cause a 30 % increase in the electric field (compare Figures 4.14 and 4.17), therefore an increase in the sparking probability. Note that the electric field values in Figures 4.14 and 4.17 are only arbitrary.

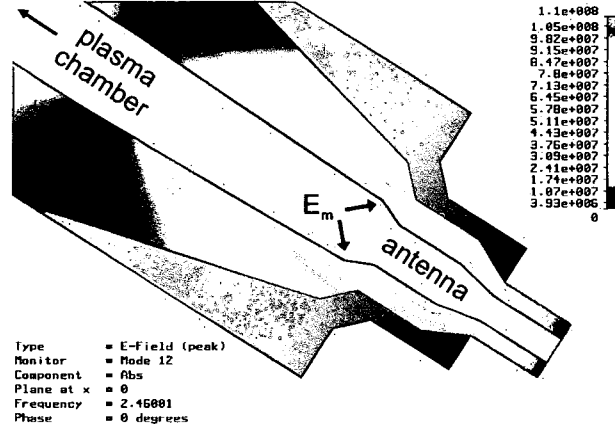


Figure 4.17: The layout of the antenna mounting with the installed taper (gray) and the resulting electric field (Electric field values arbitrary, $z = 30$ mm).

The maximum electric field E_m at the position indicated in Figure 4.17, using

$$E_m = \frac{V_0}{r_i \cdot \ln\left(\frac{r_o}{r_i}\right)} \quad (4.5)$$

with $V_0 = \sqrt{2PZ_0} \approx 330$ V for a microwave power of 1.1 kW and 50Ω impedance, is ~ 0.1 MV/m.

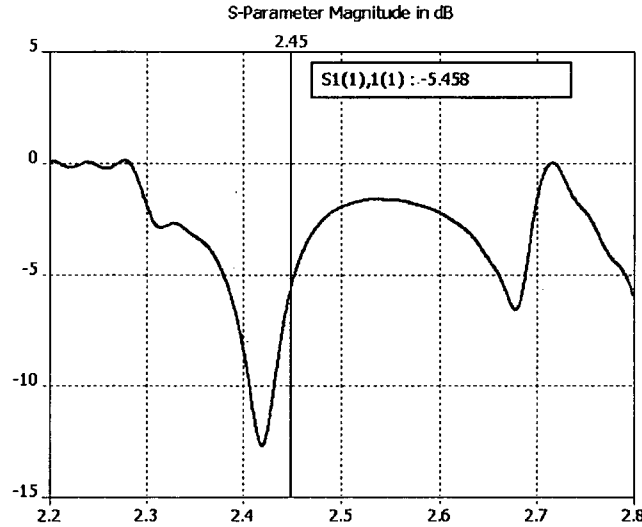


Figure 4.18: Simulation of the S_{11} parameter of the plasma chamber with a taper (Marker at 2.45 GHz, $z = 30$ mm).

This is still more than a factor 300 below the electric field necessary for sparking, according to the Kilpatrick sparking criterion (29.5 MV/m at 1 GHz) [62].

Both the simulations (compare Figures 4.15 and 4.18) and the measurements (compare Figures 4.16 and 4.19) show a small 5% reduction of the microwave power reflection coefficient.

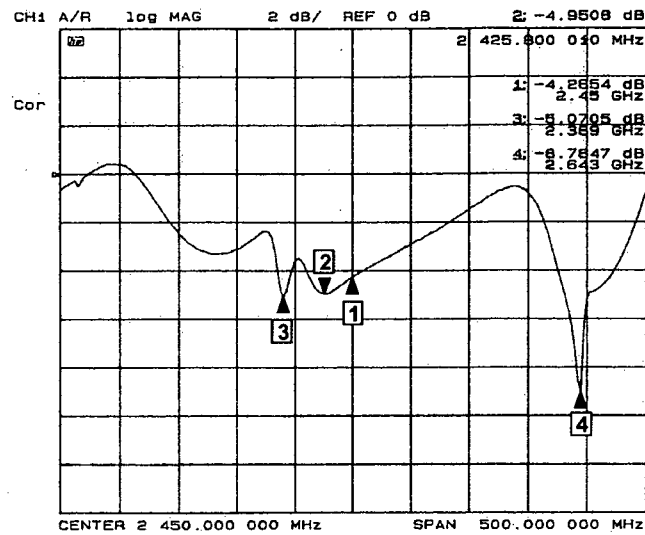


Figure 4.19: Measurement of the S_{11} parameter of the plasma chamber with a taper (Marker 1 at 2.45 GHz, $z = 30$ mm).

With an input power of 550 Watt and a duty factor of 10 %, the taper reduced the temperature measured on the feed-through surface by ~ 12 %.

4.3 e^-/H^- -separation

Together with the H^- ions large quantities of electrons are extracted. A small spectrometer consisting of two coils (see Table 4.2) separates the H^- ions from the electrons. Two biased Faraday cups allow the independent measurement of H^- and electron current.

	layers	turns	R_{Coils} [mm]	I [A]	B [T]
Wire $\phi = 1.3$ mm	4	76	27	5.9	0.008 T

Table 4.2: Main parameters of the separation solenoids for an extraction voltage of 20 kV.

The electrons are directed to Faraday Cup 2, while the heavier H^- ions and other heavy negative particles continue to Faraday Cup 1 (see Figure 4.20). For the maximum homogeneous magnetic flux density the two coils have to be arranged in a distance equivalent to the coil radius, equation (4.1) then leads to

$$B\left(\frac{b}{2}\right) = \frac{8\mu_0}{\sqrt{125}} \frac{nI}{R} \quad (4.6)$$

The two Faraday cups and the spectrometer are arranged as an isosceles triangle of ~ 11 cm length; to deflect a 20 kV electron into the outer cup (Cup2) ~ 0.008 T are needed.

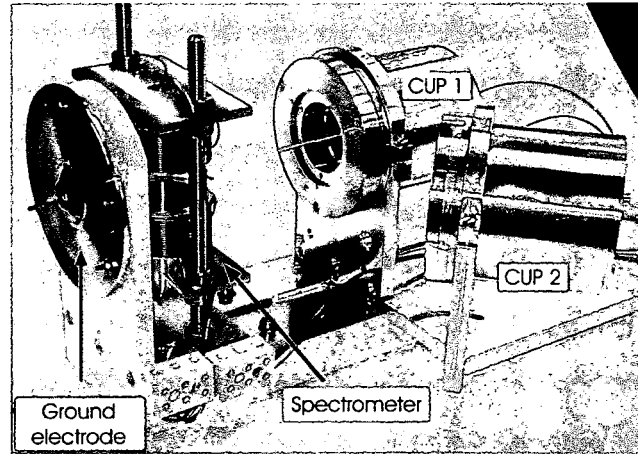


Figure 4.20: Ground electrode with the e^-/H^- separation coils and the subsequent Faraday Cups.

Chapter 5

Experiments with the CERN H⁻ source

The behavior of the source depends on several parameters. For a complete analysis of the parameter space the influence of each of them has to be considered. To make this task easier some settings are kept constant for all measurements and if possible independent of the others (see Table 5.1).

repetition rate of the microwave	1 Hz
extraction voltage	20 kV
e ⁻ /H ⁻ spectrometer	5.9 Ampere, 5.2 Volt, pulse length 30 to 40 ms
bias voltage Faraday cups	-100 Volt
tank vacuum pressure	below 7·10 ⁻⁷ mbar without gas flow

Table 5.1: Constant parameters and vacuum condition for the measurements.

The main parameters are the hydrogen gas flow, the microwave power, the antenna position and the bias of the plasma electrode. Their influence is observed for all three magnetic structures. For an overview on the parameters and their variation range see Table 5.2.

magnetic structure	<ul style="list-style-type: none"> · permanent magnets: with/without 10 additional magnets around the production region · solenoids: 0 - 0.15 T per coil · solenoids + perm. magnets: 0 - 0.15 T per coil
hydrogen gas flow	2 - 12 ml/min (tank pressure: 3·10 ⁻⁵ - 8·10 ⁻⁴ mbar)
microwave power	150 - 1500 (1200) ^a W, pulse length 10 to 30 ms or cw
antenna position	$\lambda_{2.45\text{ GHz}}/4$ (30.6 mm) ± 20 mm into the plasma chamber
plasma electrode	±60 V bias voltage

^aMaximum power changed due to a change of magnetron

Table 5.2: Main parameters and their variation ranges for source tuning.

For all measurements the H⁻ current, the electron current, the pressure in the extraction tank, the reflected power and later also the current onto the plasma electrode were recorded.

5.1 Source behavior for different magnetic structures

5.1.1 Multicusp structure with additional permanent magnets

After an inaugurating experiment with an arc discharge, using an oxide cathode, normally used in the CERN Linac2 duoplasmatron [50, 114], both with a positive power supply for proton extraction (~ 15 mA of protons) and a negative one for H⁻ extraction (~ 0.6 mA of H⁻ current without a magnetic filter), the first measurements were done with the microwave-driven source with the multicusp magnetic structure.

Since the plasma needs about 5 to 6 ms to become stable (see Figure 5.2) the microwave pulse length is 10 ms and the measurements are done after 7.5 ms.

The whole parameter space (see Table 5.2) was explored, but the source output of maximum $20 \mu\text{A}$ H⁻, with 13 mA of electrons and an e^-/H^- ratio of 650, was low. As a possible explanation a too small electron density in the production region was suspected. For this reason the permanent magnets were extended to surround the production region of the plasma chamber (see Chapter 4.1.1) for additional plasma confinement. This resulted in a small increase of the H⁻ current to $\sim 26 \mu\text{A}$ with 13.2 mA of electrons and an e^-/H^- ratio of ~ 500 .

Source response to changes in microwave power and hydrogen gas flow

The dependence of the source output on the hydrogen gas flow and the microwave power is examined for fixed antenna positions and a grounded plasma electrode. For a gas flow of 2 ml/min the pressure inside the tank is $\sim 3 \cdot 10^{-5}$ mbar, increasing to $\sim 8 \cdot 10^{-4}$ mbar at 12 ml/min.

The use of a stub tuner extends the power range to lower input powers of 50 Watt. The minimum without the tuner is 130 Watt.

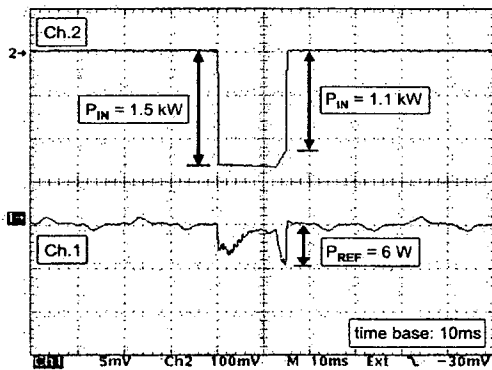


Figure 5.1: Forwarded (Channel 2) and reflected power (Channel 1) at 1.5 kW power and 4 ml/min gas flow, $z = 35$ mm.

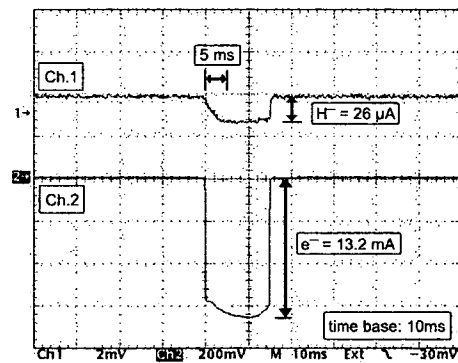


Figure 5.2: Electron (Channel 2) and H⁻ current (Channel 1) at 1.5 kW power and 4 ml/min gas flow, $z = 35$ mm.

The absolute values given for the measured reflected power are only arbitrary in their quantity. The reason is a damaged attenuator in the measurement line with 33 dB instead of 20 dB, reducing the measured reflected power by an approximate factor of 20. A comparison of the individual measurements is nevertheless possible.

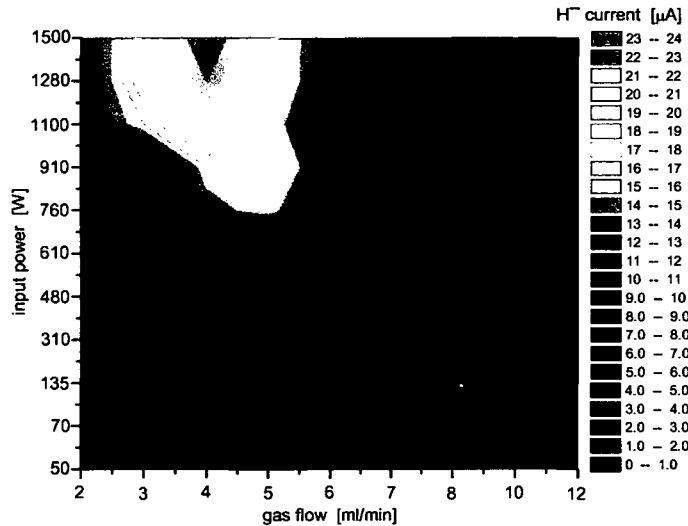


Figure 5.3: Dependence of the H^- current (in μA) on initial microwave power and gas flow (multicusp structure, bias voltage 0 V, antenna position $z = 25$ mm).

The influence of the gas is difficult to assess. For increasing hydrogen gas flows the electron and H^- current are reduced (see top right corner in Figures 5.3 and 5.4). Measurements at the "Camembert III" source delivered similar results [11]. This could not only be an effect of the H^- production, as well it could be a direct result of the missing differential pumping between vacuum tank and source, since an increase of the pressure inside the source results in an increase of the pressure in the extraction tank as well.

Therefore, due to the higher amount of residual gas in the tank and the sensitivity of the H^- ion to it, the results for the H^- current for high gas flows are most likely too low.

Starting from zero forwarded microwave power, a power increase is accompanied by an increase of the electron and H^- current and the reflected microwave power for all gas flows, until, at a certain forwarded power, a sudden drop of the reflected power (see Figure 5.5) and a simultaneous increase in particle output is observed.

For a gas flow of 3 ml/min this happens at about 1100 Watt. This region of optimal source tuning is reached at smaller input powers for higher gas flows, for a gas flow of 7 ml/min at about 800 Watt. Again the particle currents are reduced with higher gas flows.

The improved source tuning at higher forwarded power can also be observed in Figure 5.1. To demonstrate this behavior, at the end of the microwave pulse the forwarded power is reduced from 1.5 kW to 1.1 kW. This artificial drop is caused by extending the microwave

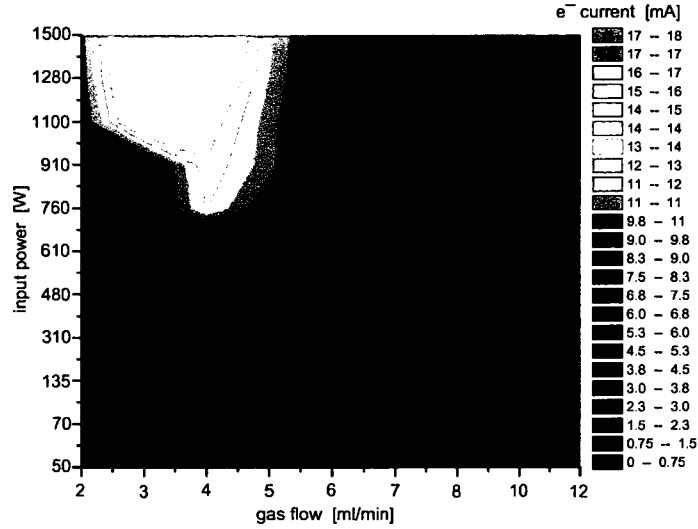


Figure 5.4: Dependence of the electron current (in mA) on initial microwave power and gas flow (multicusp structure, bias voltage 0 V, antenna position $z = 25$ mm).

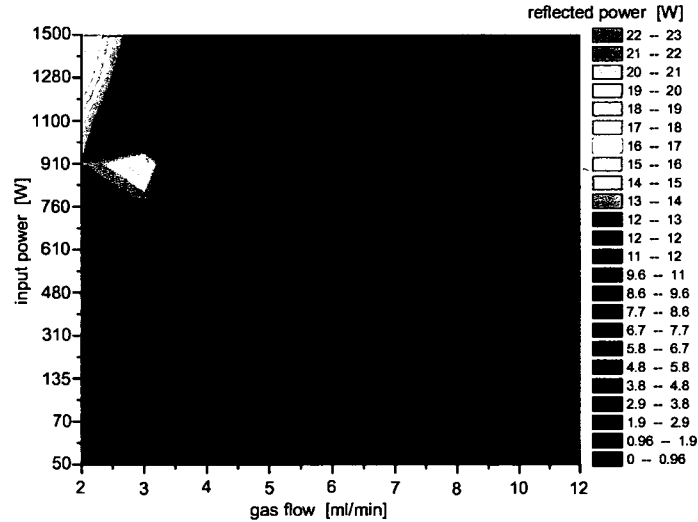


Figure 5.5: Dependence of the reflected power (in W) on initial microwave power and gas flow (multicusp structure, bias voltage 0 V, antenna position $z = 25$ mm).

pulse length beyond the maximum pulse length and capacity of the magnetron (10 ms). As a consequence, the reflected power increases.

Source tuning by means of changed antenna positions

The variation of the antenna length reaching into the plasma chamber between $z = 10$ mm and $z = 50$ mm yields the best source tuning for a length slightly below $\lambda_{2.45\text{ GHz}}/4 \sim 30.6$ mm at $z = 25$ mm (see Figure 5.6).

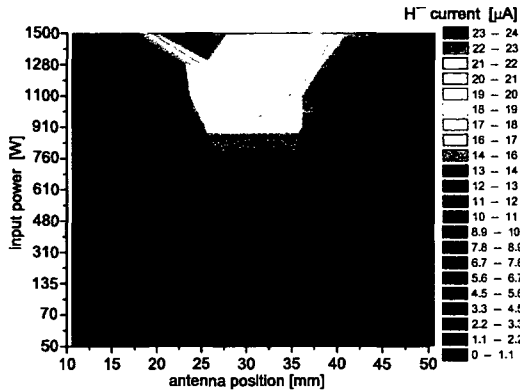


Figure 5.6: Dependence of the H^- current (in μA) on the antenna position and the microwave power (multicusp structure, bias voltage 0 V, gas flow = 4 ml/min).

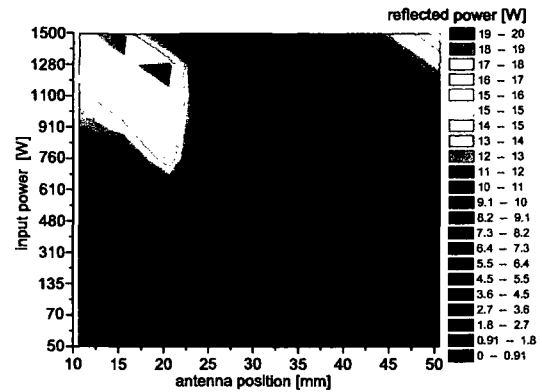


Figure 5.7: Dependence of the reflected power (in W) on the antenna position and the microwave power (multicusp structure, bias voltage 0 V, gas flow = 4 ml/min).

For some experiments a length closer to $\lambda_{2.45\text{ GHz}}/4$, $z \sim 30$ mm, brought slight improvements. In general a completely withdrawn antenna results in higher reflected powers than for one pushed forward into the plasma chamber (see Figure 5.7).

Influence of a spatial potential in the H^- extraction region

The plasma electrode can be biased to ± 60 Volt with respect to the chamber, and the extracted negative ion and electron currents are sensitive to the applied bias potential. Experiments using the laser-induced photodetachment (PHD) method [13] for a measurement of the H^- and electron densities near the plasma electrode at the "CAMEMBER III" source [25] of the Ecole Polytechnique, France, show that a positive bias of the plasma electrode increases the negative ion density near the plasma electrode and as a consequence the extracted H^- current [11]. Also the electron density is reduced and with it the extracted electron current. This was also found by J. Bruneteau et al. [17].

The results for different plasma electrode bias voltages are in accordance to this earlier measurements (see Figures 5.8 to 5.11).

A negative bias of the electrode deteriorates the source performance while the H^- current can be increased by a factor of about 10 to more than $200\text{ }\mu\text{A}$ with a positive bias (compare Figures 5.3 and 5.12). The removal of large quantities of electrons near the extraction with a plasma electrode bias voltage of $+30$ V reduces the electron current to a third of the value without a bias voltage.

The plasma electrode current shows a voltage-current-behavior similar to a Langmuir probe [23, 121] (see Figure 5.10).

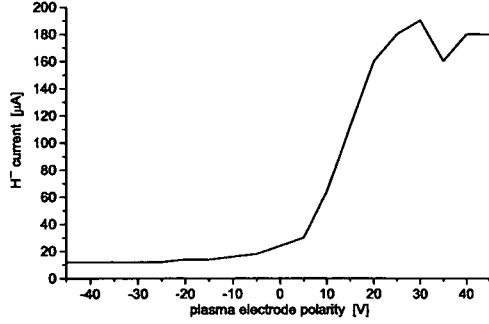


Figure 5.8: Dependence of the H^- current on the plasma electrode voltage (multicusp structure, microwave power 1500 W, antenna position $z = 25$ mm, gas flow = 4 ml/min).

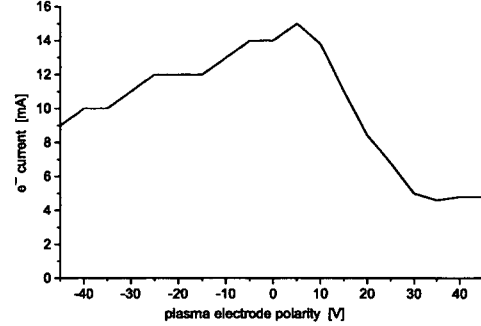


Figure 5.9: Dependence of the electron current on the plasma electrode voltage (multicusp structure, microwave power 1500 W, antenna position $z = 25$ mm, gas flow = 4 ml/min).

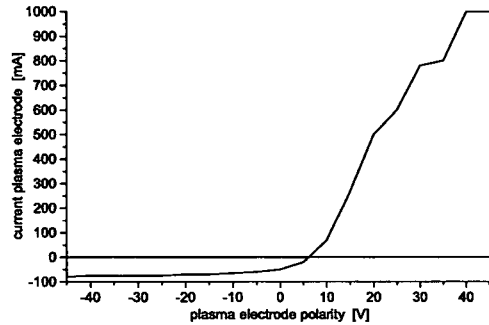


Figure 5.10: Dependence of the current through the plasma electrode on the plasma electrode voltage (multicusp structure, microwave power 1500 W, antenna position $z = 25$ mm, gas flow = 4 ml/min).

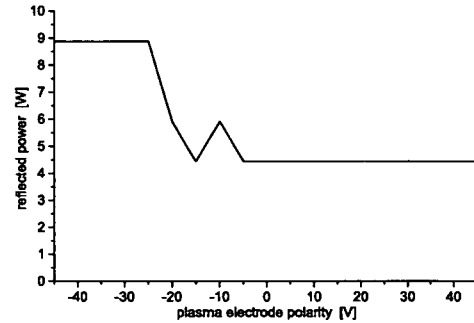


Figure 5.11: Dependence of the reflected power on the plasma electrode voltage (multicusp structure, microwave power 1500 W, antenna position $z = 25$ mm, gas flow = 4 ml/min).

The reflected power is also reduced by the positive bias of the plasma electrode and its effects on the plasma (see Figure 5.11).

The maximum beam current is reached at +30 Volt. The beam stability deteriorates with higher bias voltage, the cause being unknown. Possible explanations of the increasing instability could be plasma oscillations or plasma instabilities as a consequence of the pulsed operation. Applying a higher bias than +40 V is therefore useless, most of the measurements are done with a bias voltage of +20 V, as a compromise between maximum H^- current and beam quality.

The reduced electron and increased H^- currents naturally have a big influence on the e^-/H^- ratio. This ratio is for most of the measurements in the range of 20 - 80 (see Figures 5.13 and 5.14), compared to 500 and more of the first measurements.

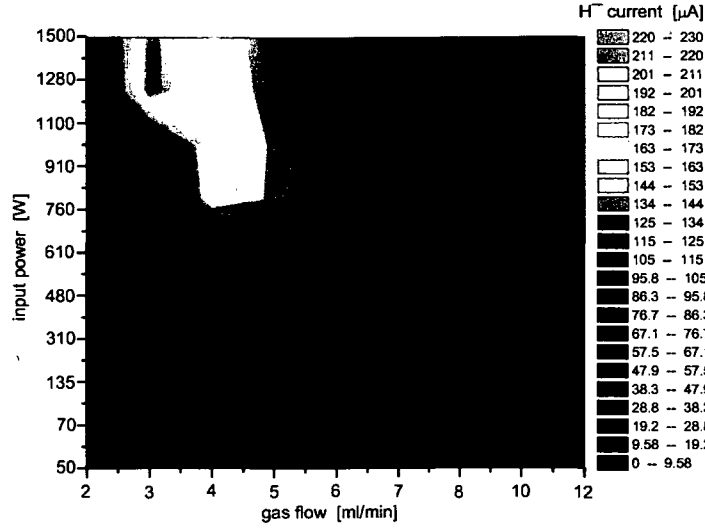


Figure 5.12: Dependence of the H^- current (in μA) on initial microwave power and gas flow (multicusp structure, bias voltage +30 V, antenna position $z = 25$ mm).

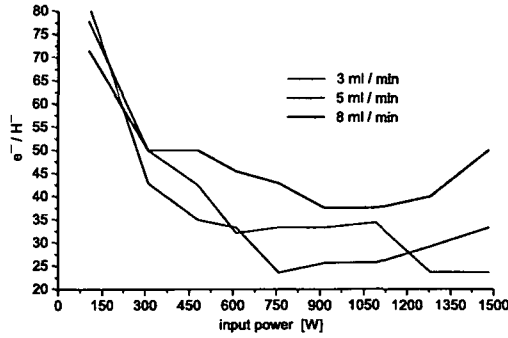


Figure 5.13: Dependence of the ratio e^-/H^- on initial microwave power for different gas flow rates (multicusp structure, bias voltage +30 V, antenna position $z = 25$ mm).

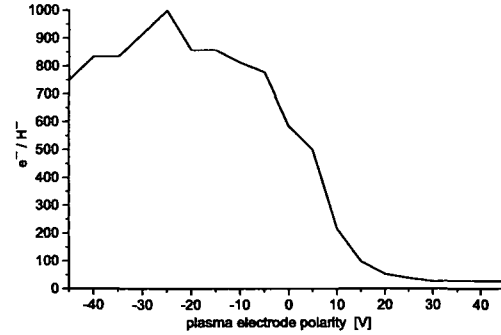


Figure 5.14: Dependence of the ratio e^-/H^- on the plasma electrode voltage (multicusp structure, microwave power 1500 W, antenna position $z = 25$ mm, gas flow 3 ml/min).

5.1.2 Solenoidal structure

The permanent magnets were replaced by two solenoids. The stronger magnetic field was expected to result in a higher electron density and therefore in a higher H^- beam current. The 1.5 kW pulsed microwave generator had to be replaced by a 1.2 kW generator which, according to specification, should be able to deliver 1.2 kW of pulsed or 1 kW of cw microwave power. During the replacement also the damaged attenuator was discovered

and replaced, allowing the quantitative measurement of the reflected power.

Since the solenoids, due to cooling requirements, have to be pulsed, the microwave system is also operated in pulsed mode and the microwave pulse placed on the flat top of the magnetic field (see Figure 5.15).

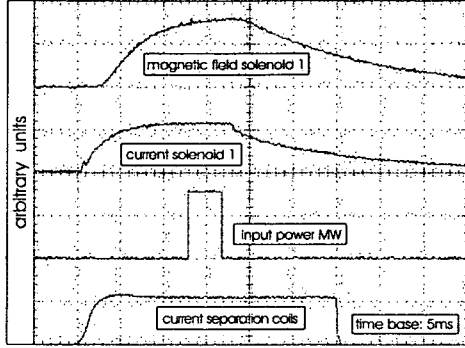


Figure 5.15: Timing scheme for a constant magnetic field during the microwave pulse.

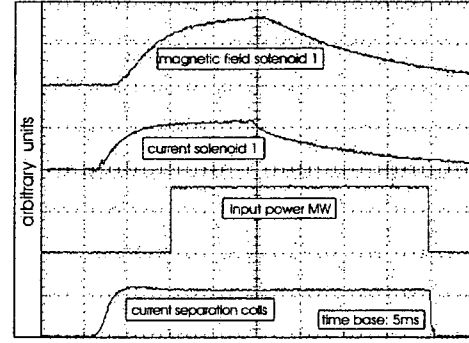


Figure 5.16: Timing scheme for a decreasing magnetic field during the microwave pulse.

Already the first measurements showed that the expectations for an increased H^- ion output of the source would not be fulfilled.

The solenoid further away from the H^- production region, Solenoid 1 (see Chapter 4.1.2), is used for igniting the plasma, an event taking place at a current above 20 Ampere (see Figures 5.17 to 5.20).

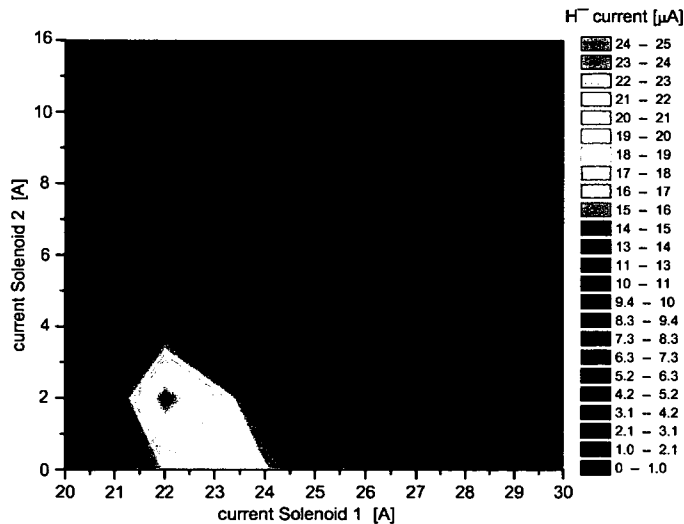


Figure 5.17: Dependence of the H^- current (in μA) on the solenoid currents (solenoidal structure, microwave power 1100 W, bias voltage +20 V, antenna position $z = 30$ mm, gas flow = 3.4 ml/min).

It was planned to generate a kind of magnetic mirror with the two solenoids, but the beam stability is badly affected by the magnetic field of Solenoid 2.

The two solenoids are arranged in such a way that, according to SUPERFISH simulations, the 0.0875 Tesla resonance surface of the solenoid nearer to the extraction (Solenoid 2) does not reach into the H^- production region below a current of 22 Ampere in both solenoids.

Although accidental electron heating in the H^- production region can therefore be excluded, already at a current of 6 Ampere through Solenoid 2, with a corresponding maximum flux density of 0.038 Tesla on the chamber wall in the center of Solenoid 2 and 0.004 T at the extraction hole, the beam stability becomes unacceptable and no H^- ions can be measured (see Figure 5.17).

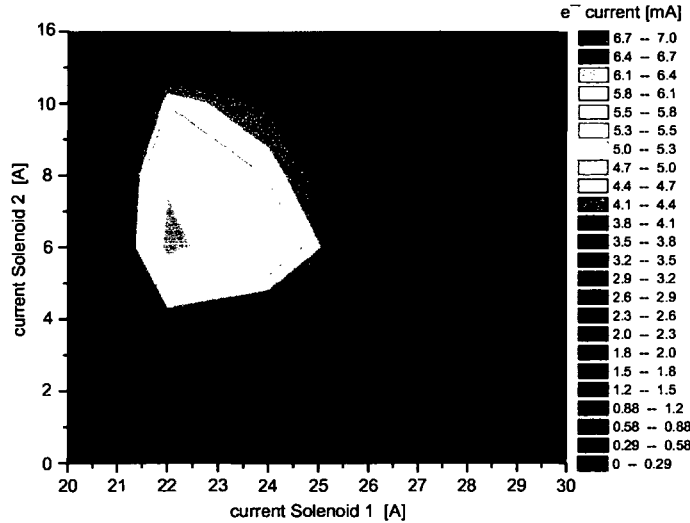


Figure 5.18: Dependence of the electron current (in mA) on the solenoid currents (solenoidal structure, microwave power 1100 W, bias voltage +20 V, antenna position $z = 30$ mm, gas flow = 3.4 ml/min).

A smaller magnetic field in the extraction, generated by Solenoid 2, seems to enhance the H^- output. A small stray magnetic field in the extraction region also improved the H^- output of the "Camembert III" source [11, 101].

With the multicusp magnetic structure, the highest electron and H^- currents were extracted at the same source parameters (see Chapter 5.1.1), for the solenoidal structure this is different. The highest electron current is found for a higher magnetic field on Solenoid 2. In Figure 5.18 also a drop of the electron current with the increasing magnetic field of Solenoid 1 is observed.

SUPERFISH simulations show that for a setting of Solenoid 1 = 27 A and Solenoid 2 = 6 A, the ECR surface is starting to reach into the antenna channel (see Figures 5.21 and 5.22).

Since the electron density is especially high at the ECR surface [43], the microwave power coupling might be negatively affected or even be short circuited, resulting in a

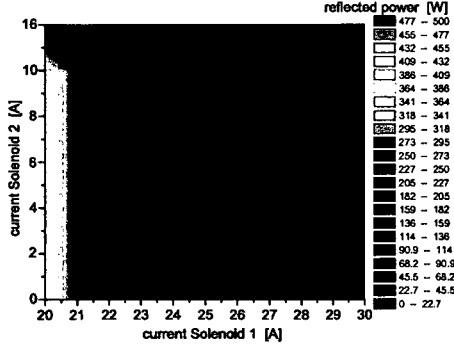


Figure 5.19: Dependence of the reflected power (in W) on the solenoid currents (solenoidal structure, microwave power 1100 W, bias voltage +20 V, antenna position $z = 30$ mm, gas flow = 3.4 ml/min).

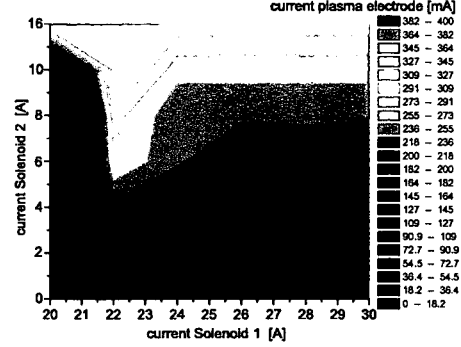


Figure 5.20: Dependence of the plasma electrode current (in mA) on the solenoid currents (solenoidal structure, microwave power 1100 W, bias voltage +20 V, antenna position $z = 30$ mm, gas flow = 3.4 ml/min).

higher reflected power for an increased current through Solenoid 1 (see Figure 5.19). The variation of hydrogen gas flow and microwave power, for a solenoid setting of Solenoid 1 = 22 Ampere and Solenoid 2 turned off, show a behavior similar to the multicusp structure (see Chapter 5.1.1).

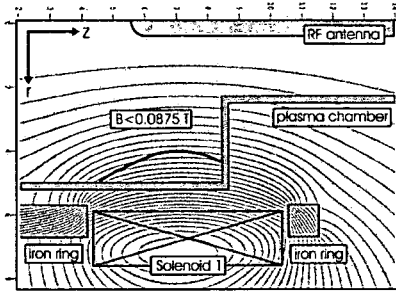


Figure 5.21: The 0.0875 T surface of Solenoid 1 at a current of 22 Ampere (Solenoid 2 = 6 A).

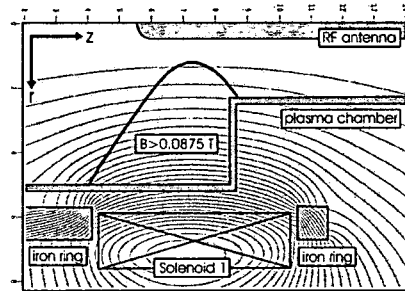


Figure 5.22: The 0.0875 T surface of Solenoid 1 at a current of 27 Ampere (Solenoid 2 = 6 A).

The variations of the microwave power and the hydrogen gas flows showed that no H^- ions can be extracted for gas flows above 8 ml/min. The highest H^- current can be found for a gas flow of 2 ml/min at 1.1 kW, with $28 \mu A$ of H^- ions and 7 mA electron current. The variation of the antenna position brought the best results for an antenna length of $z = 30$ mm ($\sim \lambda_{2.45 GHz}/4$ into the plasma chamber (see Figure 5.23)).

The optimal plasma electrode voltage bias, taking into account the decreasing beam quality for higher bias voltages, was again found at +20 Volt.

The e^-/H^- ratio is worse compared to the multicusp structure, above a ratio of 100 for all bias voltages (see Figure 5.24).

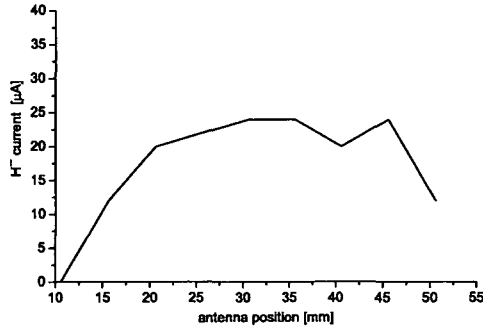


Figure 5.23: The H^- current (in μA) as dependence from the antenna position (solenoidal structure, microwave power 1100 W, Sol1 = 22 A, Sol2 = 0 A, bias voltage +20 V, gas flow = 2 ml/min).

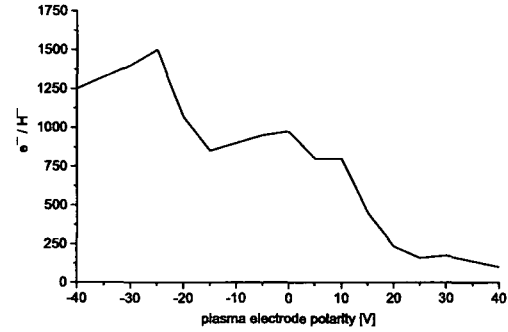


Figure 5.24: The ratio e^-/H^- as dependence from the plasma electrode voltage (solenoidal structure, microwave power 1100 W, Sol1 = 22 A, Sol2 = 0 A, antenna position $z = 30$ mm, gas flow 2 ml/min).

Source behaviour for a degrading solenoidal magnetic field

Both the small H^- current and the low beam quality for an operating Solenoid 2 indicate a too hot plasma for efficient H^- volume production due to the strong magnetic field.

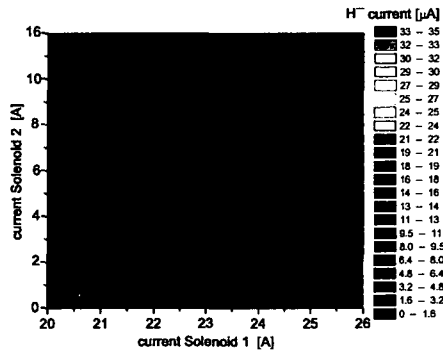


Figure 5.25: Dependence of the H^- current (in μA) on the solenoid currents after 10 ms (solenoidal structure, microwave power 1100 W, bias voltage +20 V, antenna position $z = 30$ mm, gas flow = 3.4 ml/min.)

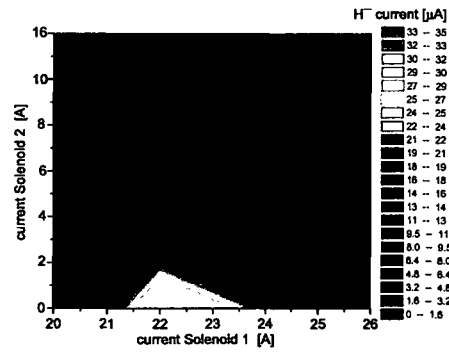


Figure 5.26: Dependence of the H^- current (in μA) on the solenoid currents after 20 ms (solenoidal structure, microwave power 1100 W, bias voltage +20 V, antenna position $z = 30$ mm, gas flow = 3.4 ml/min).

A different timing of microwave and solenoidal pulse was tried (see Figure 5.16). After a short period of 1 to 2 ms for plasma ignition the magnetic field is allowed to decrease below the electron cyclotron resonance (ECR) value.

Measurements were done after 10, 15 and 20 ms of the microwave pulse and it was found that the H^- current is becoming bigger with decreasing magnetic field (compare Figures 5.25 and 5.26).

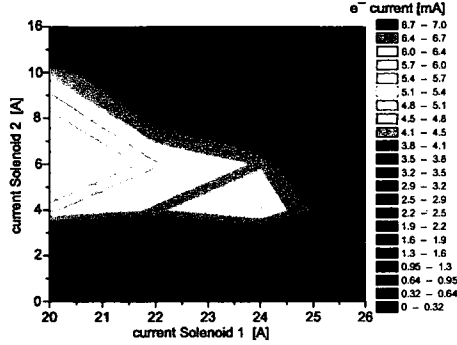


Figure 5.27: Dependence of the electron current (in mA) on the solenoid currents after 10 ms (solenoidal structure, microwave power 1100 W, bias voltage +20 V, antenna position $z = 30$ mm, gas flow = 3.4 ml/min.)

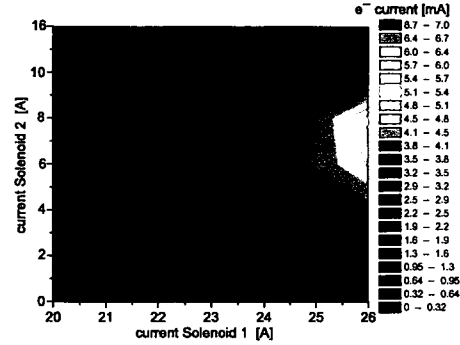


Figure 5.28: Dependence of the electron current (in mA) on the solenoid currents after 20 ms (solenoidal structure, microwave power 1100 W, bias voltage +20 V, antenna position $z = 30$ mm, gas flow = 3.4 ml/min).

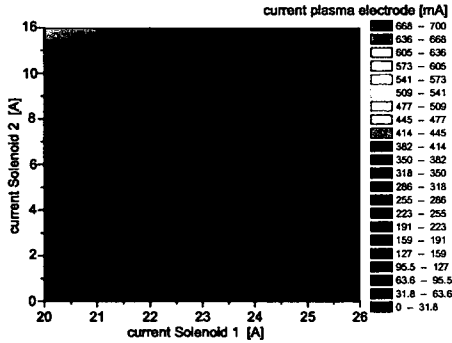


Figure 5.29: Dependence of the plasma electrode current (in mA) on the solenoid currents after 10 ms (solenoidal structure, microwave power 1100 W, bias voltage +20 V, antenna position $z = 30$ mm, gas flow = 3.4 ml/min).

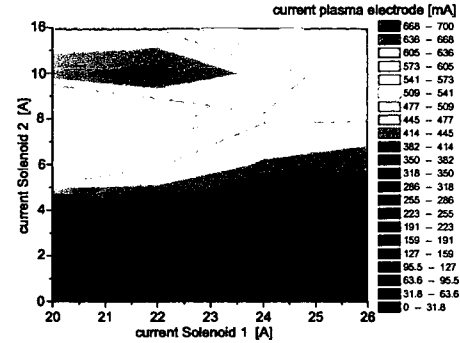


Figure 5.30: Dependence of the plasma electrode current (in mA) on the solenoid currents after 20 ms (solenoidal structure, microwave power 1100 W, bias voltage +20 V, antenna position $z = 30$ mm, gas flow = 3.4 ml/min).

The current onto the plasma electrode is higher, on the other hand the extracted electron current is smaller (compare Figures 5.29 and 5.30).

This is even more remarkable since the MUEGGE microwave generator seems not, against specification and manual, to be able to provide a constant microwave power during the 30 ms microwave pulse. The maximum microwave pulse length for 1.1 kW seems to be 15 ms, no quantitative statements can therefore be made for the measurement after 20 ms. Nevertheless, with the magnetic field degraded to about half its initial strength after 20 ms and less microwave power, the amount of extracted H^- ions is bigger compared to the measurement after 10 ms, with maximum magnetic field and full microwave power.

This indicates that the solenoids with a magnetic field sufficient for ECR heating are generating a too hot plasma for efficient H^- production. This was also observed at the H^- source at the CEA/Saclay [41]. The H^- source there is also operating with two solenoids, but in DC mode [37, 40].

5.1.3 Combination of solenoidal and multicusp structure

The inner space of both the solenoids and the iron rings are equipped with slots, to allow the additional installation of the permanent magnets (see Chapter 4.1.3). A 10 ms pulse is used for the microwave, the measurements are taken after 7.5 ms to allow the plasma to stabilise.

Since the permanent magnets provide the necessary field to ignite the plasma, Solenoid 1 doesn't have to be run above 22 Ampere. As a consequence the break down of the H^- beam stability occurs at higher operating currents for Solenoid 2.

The measurements with a multicusp structure showed that optimal source tuning is achieved at higher gas flows with lower power (see Chapter 5.1.1). In accordance with this earlier measurements, for 1.1 kW microwave power this region of minimal reflected microwave power and maximum H^- current was found for a gas flow of 6 ml/min (compare Figures 5.5 and 5.34).

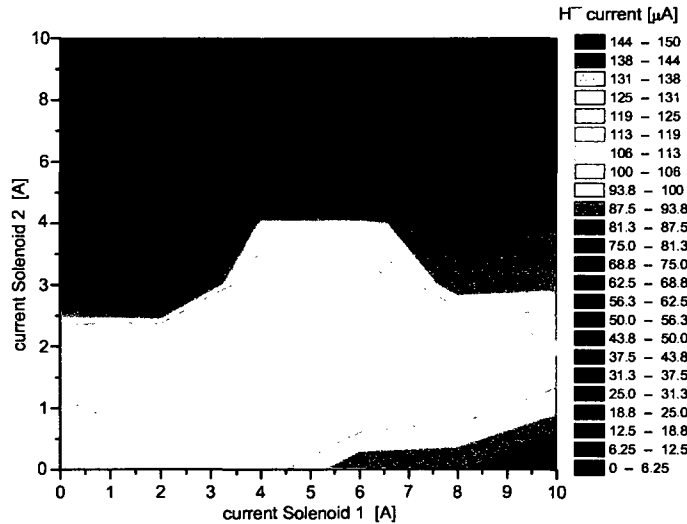


Figure 5.31: Dependence of the H^- current (in μA) on the solenoid currents (combined structure, microwave power 1100 W, bias voltage +30 V, antenna position $z = 25$ mm, gas flow = 6 ml/min).

Without a contribution of the solenoids to the magnetic field, the H^- current for a gas flow of 6 ml/min is 100 μA (see Figure 5.31) and therefore smaller than the results achieved with the original multicusp structure ($\sim 130 \mu A$, see Figure 5.12).

An explanation could be the completely rebuilt microwave system and the different iron quantities and distributions around the permanent magnets. The covering iron rings are

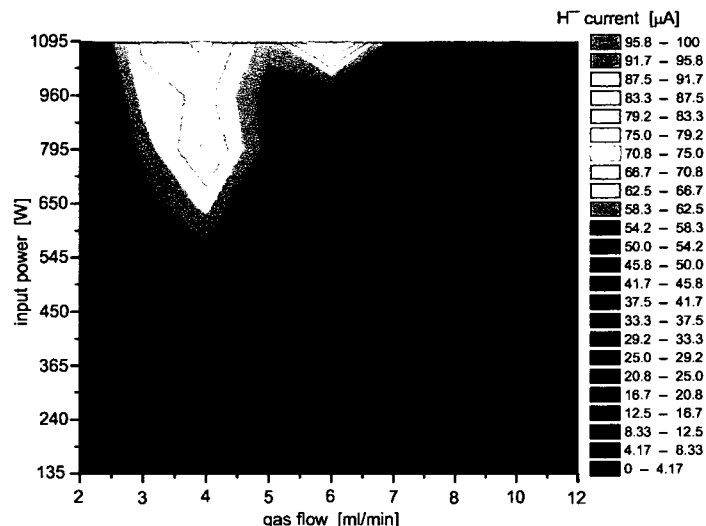


Figure 5.32: Dependence of the H^- current (in μA) on initial microwave power and gas flow (combined structure, bias voltage +20 V, antenna position $z = 25$ mm, Sol1 = 4 A, Sol2 = 2 A).

thicker than the original iron cylinder and inside the solenoids there is no iron at all, reducing the magnetic field of the permanent magnets on the plasma chamber between two neighbouring magnets by a factor of two.

A small magnetic field in the extraction region, generated by the two solenoids, improves the H^- output by ~ 40 percent (see Figure 5.31). Also the extracted H^- ion current at higher hydrogen gas flows seems to be increased.

The measurements with the multicusp structure showed that the highest currents for both H^- ions and electrons are achieved at gas flows of about 3 to 4 ml/min with maximum microwave power (see Chapter 5.1.1). This changed with the addition of the solenoids. The maximum electron current has moved to higher hydrogen gas flows of ~ 7 ml/min (see Figure 5.33), maybe due to the increased electron density as a consequence of the additional solenoidal field.

Nevertheless, still no significant amount of H^- ions can be measured at higher gas flows. There are at least two possible explanations for this. The electrons might be too hot and destroy the H^- ions. The second reason might be the missing differential pumping, as mentioned before.

For a fixed small magnetic field in the extraction region the influence of Solenoid 1 is shown in Figure 5.36. The increasing electron heating, due to the stronger solenoidal magnetic field, results in smaller H^- currents, as another hint that with the solenoid structure the plasma temperature is too high for efficient H^- production.

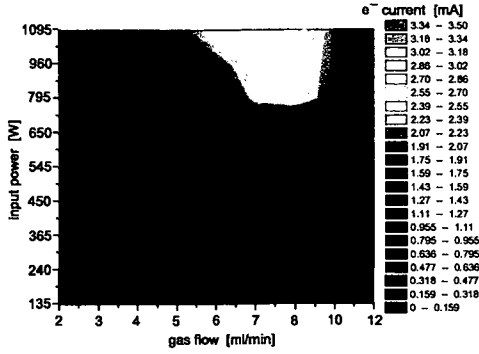


Figure 5.33: Dependence of the electron current (in mA) on initial microwave power and gas flow (combined structure, bias voltage +20 V, antenna position $z = 25$ mm, Sol1 = 4 A, Sol2 = 2 A).

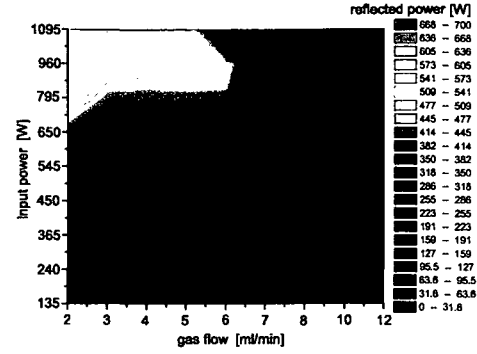


Figure 5.34: Dependence of the reflected power (in W) on initial microwave power and gas flow (combined structure, bias voltage +20 V, antenna position $z = 25$ mm, Sol1 = 4 A, Sol2 = 2 A).

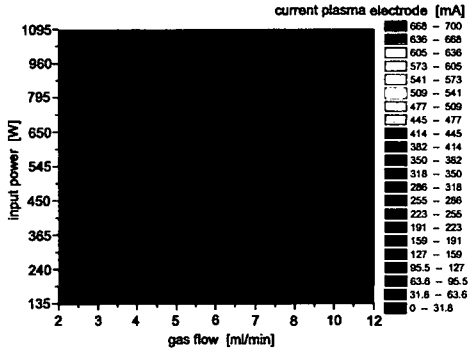


Figure 5.35: Dependence of the plasma electrode current (in mA) on initial microwave power and gas flow (combined structure, bias voltage +20 V, antenna position $z = 25$ mm, Sol1 = 4 A, Sol2 = 2 A).

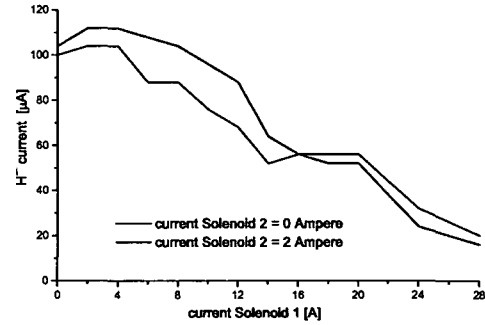


Figure 5.36: Dependence of the H^- current (in μA) on the current in Solenoid 1 (combined structure, microwave power 1100 W, bias voltage +30 V, antenna position $z = 25$ mm, gas flow = 6 ml/min).

5.2 The influence of tantalum on the H^- ion production

The effect of surface reactions in volume hydrogen negative ion sources has been extensively discussed [30, 71]. The important surface reactions in this context are the collisional wall de-excitation of vibrationally excited molecules and the wall recombination of atoms (followed by recombinative desorption of hydrogen molecules).

Under some conditions the de-excitation of vibrationally excited molecules in wall collisions may be the dominating destruction mechanism for these precursors of the H^- ions (see Chapter 2).

Also a low density of hydrogen atoms is very important for efficient H^- volume production [9]. At the low pressure used in ion sources, wall recombination is the only loss for atomic

hydrogen other than physical pumping.

At the "CAMEMBERT III" source [25], the steady reduction in the H^- source output during long time measurements was suspected to be caused by a decreasing tantalum concentration on the plasma chamber wall.

The positive effect of tantalum on H^- production was confirmed by experiments with an artificially created tantalum layer on the wall, produced via the evaporation of a tantalum filament [10].

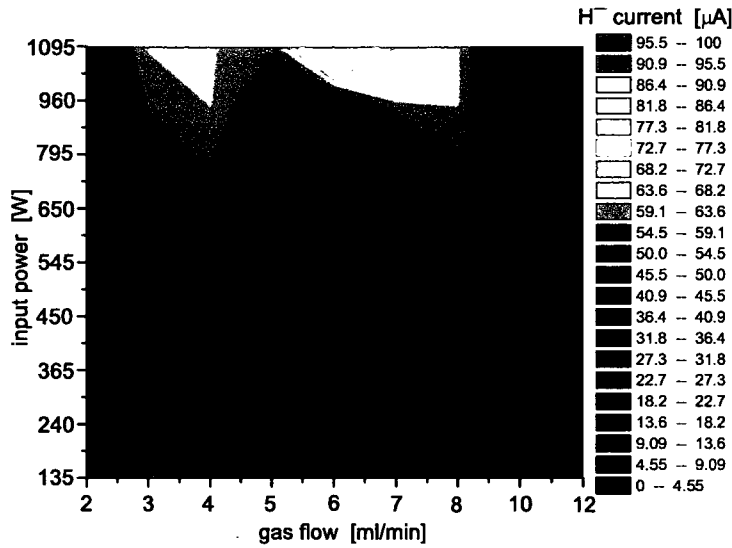


Figure 5.37: Dependence of the H^- current (in μA) on initial microwave power and gas flow with a tantalum foil (combined structure, bias voltage $+20$ V, antenna position $z = 25$ mm, Sol1 = 4, Sol2 = 2).

Inoue et al. [52] modified the wall material by evaporating filament material and suggested that the observed difference in H^- yield is due to the higher hydrogen atom recombination coefficient on a tantalum covered wall. This causes a reduction of the density of atomic hydrogen, which is considered as a poison for volume H^- production.

At the CERN H^- source, the influence of tantalum was examined twice, first with the multicusp structure and later with the combined solenoid and multicusp structure.

The 0.025 mm thin, tantalum foil of 10 times 10 centimeters suffices to cover about 40 % of the plasma chamber wall, both in the H^- production and the plasma region.

The tantalum does not change the general source behaviour, for example the optimum antenna position is still slightly below $\sim \lambda_{2.45 \text{ GHz}}/4$. The source response to variations of the gas flow is also unchanged.

Nevertheless, the tantalum has a positive effect on the absolute H^- current and the e^-/H^- ratio, although this effect is varying and small for some source settings.

For the combination of solenoids and multicusp structure (compare Figures 5.32 and 5.37), the maximum H^- current increases from 80 μA to 92 μA and the electron current decreases from 3.2 mA to 2 mA. Thus the e^-/H^- ratio changes from 40 to 22.

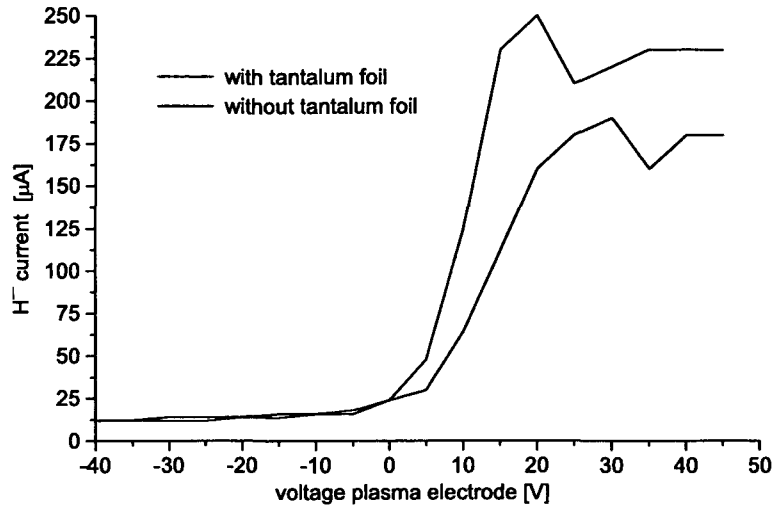


Figure 5.38: Dependence of the H^- current (in μA) on the plasma electrode bias voltage with/without tantalum foil (multicusp structure, microwave power 1100 W, antenna position $z = 25$ mm, gas flow = 4 ml/min).

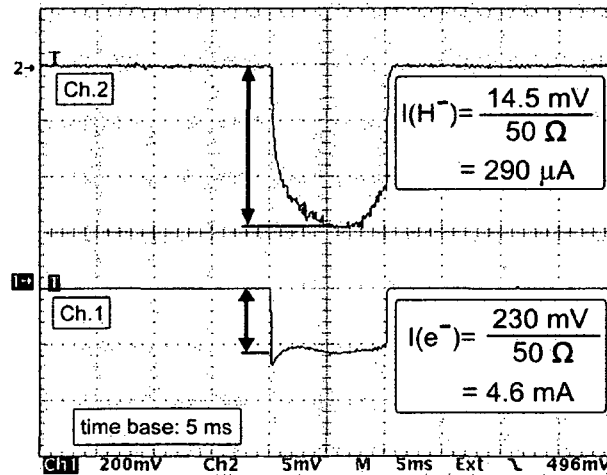


Figure 5.39: Oscillogram of the H^- current (top trace) and the electron current (bottom trace), (multicusp structure, tantalum foil, microwave power 1100 W, bias voltage +20 V, antenna position $z = 25$ mm, gas flow = 3.66 ml/min).

In addition to increasing the H^- current, the maximum H^- output is found at lower plasma electrode bias voltages (see Figure 5.38), further improving the beam stability. For the multicusp structure, the maximum H^- current is $190 \mu A$ without the tantalum foil at a plasma electrode bias voltage of +30 V, with an electron current of 5 mA. With

the tantalum foil installed this changed to 250 μA of H^- ions and 4 mA of electrons at +20 V bias voltage. The e^-/H^- ratio dropped from 26 to 16.

The combination of the multicusp structure with the tantalum foil resulted in the highest extracted H^- current of the CERN H^- source with the 1.5 kW microwave generator (see Figure 5.39). An H^- current of 290 μA with an electron current of 4.6 mA results in an e^-/H^- ratio of ~ 15 .

Since no negative effects of the tantalum foil were observed, it was left in the plasma chamber as a permanent addition for all measurements with the solenoidal structure.

5.3 Effect of a collar

Following the positive results obtained by Peters [83] when using a tantalum collar in the microwave source operated in pure hydrogen, the influence of a tantalum collar of varying length was examined.

The collar was fixed on the plasma electrode, thus put onto the same bias voltage. The collar had an inner diameter of 19 mm. Three different lengths were tried, 18 mm, 40 mm and 70 mm. The longest collar thus reaches toward the magnetic filter. The experiment was again done with all three magnetic structures and the complete parameter space was explored.

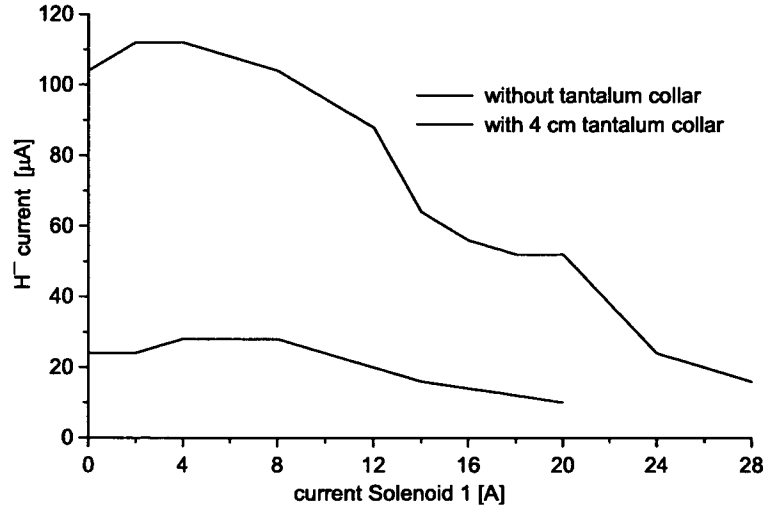


Figure 5.40: Dependence of the H^- current (in μA) on the current through Solenoid 1 (combined structure, collar, microwave power 1100 W, bias voltage +30 V, antenna position $z = 25$ mm, gas flow = 6 ml/min, Sol2 = 2 A).

The presence of the collar reduces the negative ion current depending on the collar length (see Figures 5.40 to 5.42), reducing it to one half for the shortest collar. The medium

collar cuts the H^- current approximately to a quarter, and for the longest collar only a small remnant is left. The beneficial effect is the reduction of the electron current.

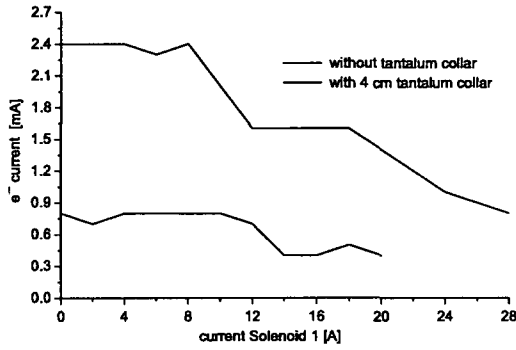


Figure 5.41: Dependence of the electron current (in mA) on the current through Solenoid 1 (combined structure, collar, microwave power 1100 W, bias voltage +30 V, antenna position $z = 25$ mm, gas flow = 6 ml/min, Sol = 2 A).

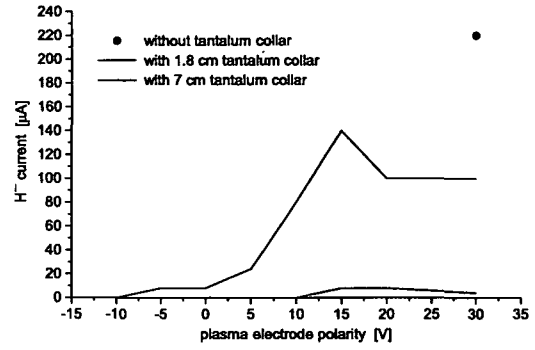


Figure 5.42: Dependence of the H^- current on the plasma electrode voltage (multicusp structure, collar, microwave power 1500 W, antenna position $z = 25$ mm, gas flow = 3 ml/min).

The measurements of Peters were done in a region with a considerable density of hot electrons, which is probably not the case for the multicusp and combined structure at the CERN H^- source. The results correspond better with Leung et al. [72], where the H^- current was reduced for a collar length of more than 1 cm, and the extracted electron current was reduced for all collar lengths. Bacal et al. [10] also reported a reduction of both the H^- and electron current.

5.4 Microwave suppression in the H^- production region

Gobin et al. [41] reported that a negatively biased stainless steel grid placed in front of the plasma electrode can enhance the negative ion production. Microwave power, which is not absorbed in the plasma, might propagate to the H^- production region and contribute to the H^- loss. The grid is believed to stop this microwave propagation and to reduce the number of hot electrons through the negative bias.

At the CERN H^- source, a stainless steel grid with 0.5 mm wire diameter and 3 mm mesh width was installed in the production region between the plasma electrode and the magnetic filter, 6 cm away from the plasma electrode (see Figure 4.1). The grid was kept at plasma chamber potential.

The measurements with a grid showed a significant reduction of both the H^- ion and electron current for all three magnetic structures. This is in agreement with the negative results of Bacal et al. [10].

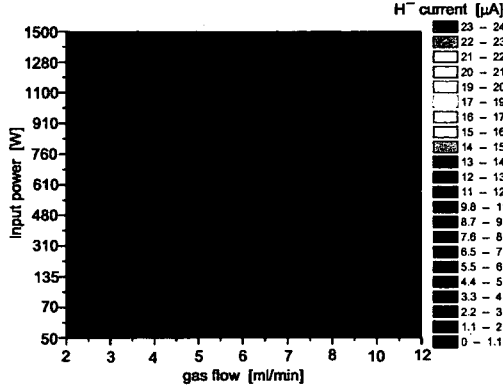


Figure 5.43: Dependence of the H^- current (in μA) on initial microwave power and gas flow (solenoidal structure, grid, bias voltage 0 V, antenna position $z = 25$ mm).

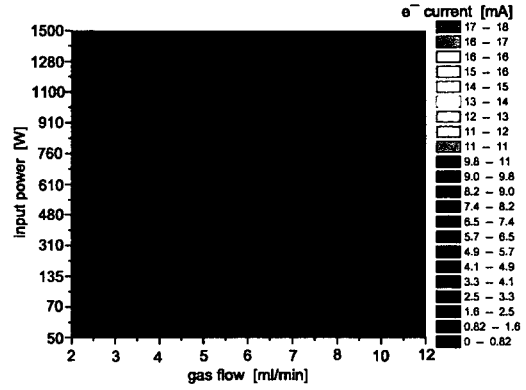


Figure 5.44: Dependence of the electron current (in mA) on initial microwave power and gas flow (solenoidal structure, grid, bias voltage 0 V, antenna position $z = 25$ mm).

For the solenoid structure the reduction was found both for the constant (compare Figure 5.43 with 5.3 and Figure 5.44 with 5.4) and the degrading magnetic field.

With the combined structure as a small positive effect the maximum H^- current was found at a lower plasma electrode bias voltage, +25 V instead of +30 V, improving the beam quality.

5.5 ECR heating on a boron nitride wall

The microwave entrance of the SILHI source at CEA/Saclay is covered with a 2 mm thick boron nitride layer and the magnetic field of the two solenoids is arranged in such a way that the 0.0875 T ECR surface is passing through the boron nitride [40]. This setup increases the H^- source output by a factor of two [38].

Boron nitride is supposed to donate electrons to the plasma and since it is an isolator, it might improve the electron containment.

At the CERN H^- source the backside of the plasma chamber was covered with a 2 mm thick boron nitride layer. Together with the support structure for the boron nitride this results in 5 mm of additional wall thickness, which has to be compensated by the antenna position setting. It was emphasised that the 0.0875 T ECR surface is situated on the boron nitride for the pure solenoidal structure.

The difference to the CEA/Saclay source is thus that the microwave does not have to propagate through the boron nitride and only the boron nitride surface is affected.

The experiment was done with all three magnetic structures. For the H^- ion output no consistent effect of the boron nitride could be found, but the extracted electron current and the reflected power were reduced with each structure and the current through the plasma electrode was increased.

Multicusp structure with additional permanent magnets

The comparison of the boron nitride measurement of the multicusp structure with the following reference measurement showed no big influence of the boron nitride on the H^- production.

Nevertheless, the first time use of the boron nitride changed the source behavior for the boron nitride experiment itself and the following reference measurement. For some source settings the H^- ion current from the reference measurement after the insertion of the boron nitride was more than doubled in comparison to a reference measurement before the use of the boron nitride.

A possible contamination of the boron nitride disc was suspected. Another explanation would be a change in its chemical composition due to the first exposure to the plasma, a one-time effect.

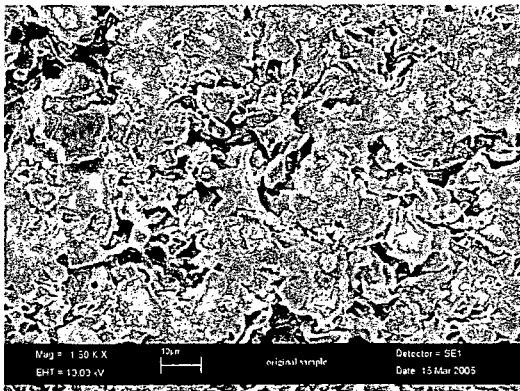


Figure 5.45: Surface of the initial boron nitride before exposure to the plasma (1500-times magnified).

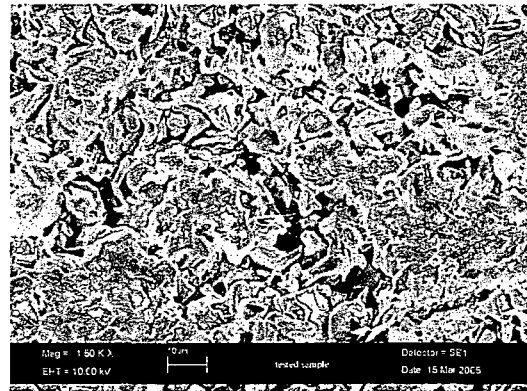


Figure 5.46: Surface of the boron nitride after exposure to the plasma (1500-times magnified).

X-ray photoelectron spectroscopy (XPS) [24] was done with a sample of the original boron nitride disc and one exposed to the plasma. The only significant difference is that the amount of carbon is lower on the sample exposed to the plasma. The amount of oxygen is slightly lower for the sample in its virgin state. Other impurities are calcium, sodium and chlorine. Calcium is usually present in boron nitride as an element used in the raw material preparation. The origin of sodium and chlorine is unknown.

No marked difference in the chemical composition, which could easily explain the different source behavior, could be found, but a morphology analysis of the two samples showed a smoother sample surface for the boron nitride disc in its original state before exposure to the plasma (compare Figure 5.45 and 5.46). It is unknown if this is the cause for the one time effect or only a normal reaction of the boron nitride to the plasma exposure.

To finally determine if the boron nitride in combination with the 0.0875 T ECR surface has a positive effect and also if the different source behaviour for the multicusp structure was accidental or not, a repetition of the experiment will be necessary.

Solenoidal structure

With the solenoidal structure, the measurements were done with the degrading solenoidal field. Due to the maximum microwave pulse length of 15 ms, only the measurement after 10 ms is analysed.

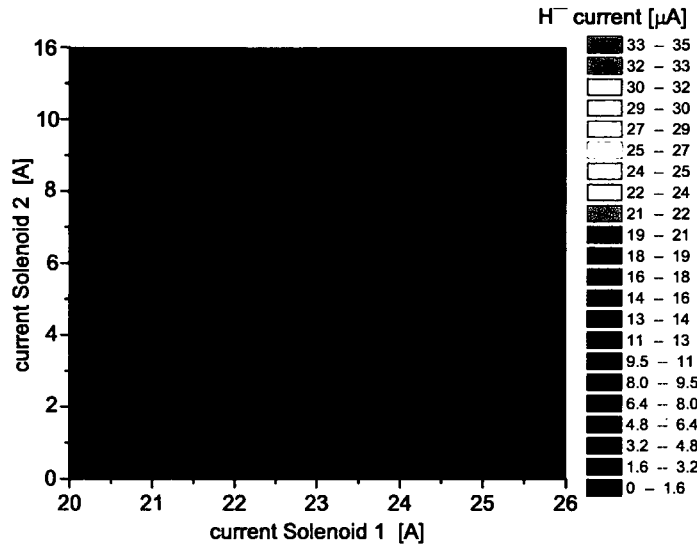


Figure 5.47: Dependence of the H^- current (in μA) on the solenoid currents after 10 ms (solenoidal structure, boron nitride, microwave power 1100 W, bias voltage +20 V, antenna position $z = 35$ mm, gas flow = 3.4 ml/min).

The maximum H^- output is unchanged by the boron nitride, but limited to currents above 22 Ampere for Solenoid 1 (compare Figure 5.47 with Figure 5.25). The maximum electron current is still ~ 6 mA, but at a solenoid setting of Solenoid 1 = 22 A, Solenoid 2 = 6 Ampere (see also Figure 5.27).

The plasma electrode current and the reflected power are unchanged. The reflected power again increases with a higher current through Solenoid 1. For the solenoidal structure no significant effect of the boron nitride disc could be discovered.

Combination of solenoidal and multicusp structure

For the combined structure the implementation of the boron nitride had a positive effect on the source performance (compare Figures 5.48 to 5.51 with Figures 5.32 to 5.35).

The maximum H^- current increased from 80 μA to 100 μA , an increase of ~ 25 %. Together with the reduction of the maximum electron current from 3.2 to 2.2 mA, the e^-/H^- ratio decreases from 40 to 22.

The reflected power is unaffected by the boron nitride disc, the maximum current through the plasma electrode at a gas flow of 7 ml/min and 1100 W input microwave power increased from 400 to 640 mA.

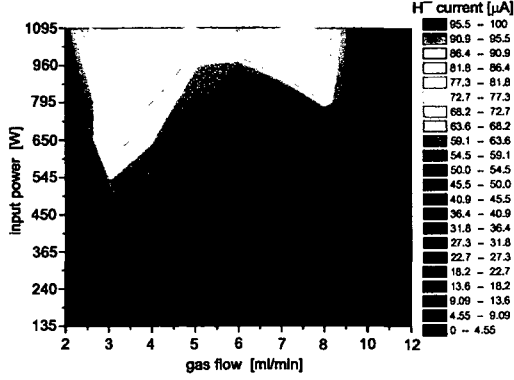


Figure 5.48: Dependence of the H^- current (in μA) on initial microwave power and gas flow (combined structure, boron nitride, bias voltage +30 V, antenna position $z = 30$ mm, Sol1 = 4 A, Sol2 = 2 A).

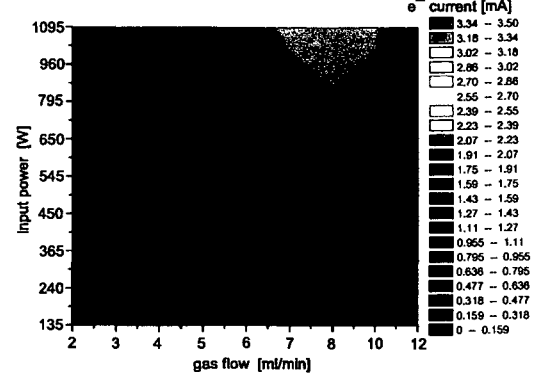


Figure 5.49: Dependence of the electron current (in mA) on initial microwave power and gas flow (combined structure, boron nitride, bias voltage +30 V, antenna position $z = 30$ mm, Sol1 = 4 A, Sol2 = 2 A).

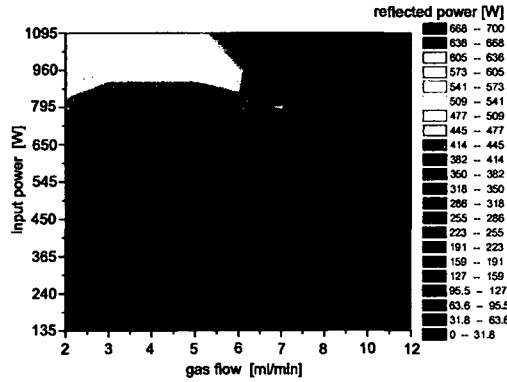


Figure 5.50: Dependence of the reflected power (in W) on initial microwave power and gas flow (combined structure, boron nitride, bias voltage +30 V, antenna position $z = 30$ mm, Sol1 = 4 A, Sol2 = 2 A).

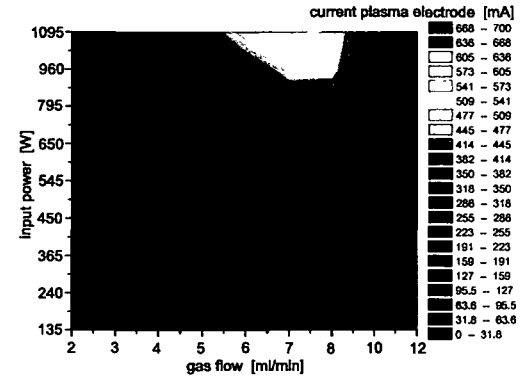
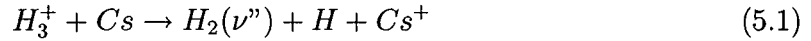


Figure 5.51: Dependence of the plasma electrode current (in mA) on initial microwave power and gas flow (combined structure, boron nitride, bias voltage +30 V, antenna position $z = 30$ mm, Sol1 = 4 A, Sol2 = 2 A).

5.6 H⁻ ion production with addition of different support gases

It has been observed that the introduction of small quantities of caesium to a hydrogen ion source significantly increases the negative ion output [49].

Together with the increased electron density, possible caesium volume effects, such as the enhancement of H₂(ν'') production by charge transfer between H₃⁺ and Cs (see Chapter 2),



the collisional cooling of electrons and the enhanced H⁻ electrostatic confinement, due to the increased plasma potential caused by the reduced mobility of the heavy ions, might also be found for other atoms such as xenon and krypton [102].

Some of the characteristic properties of the different elements, such as atomic mass, first ionisation energy and total ionisation cross-section, gathered from different sources [6, 85, 104, 116], are given in Table 5.3 and plotted in Figure 5.52.

	H	H ₂	He	Ar	Kr	Xe	Cs
mass [amu]	1	2	4	40	83.8	131.3	133
E _i [eV]	13.59	15.43	24.59	15.76	14.1	12.1	3.89

Table 5.3: Atomic mass and first ionisation energy of different atomic (molecular) species.

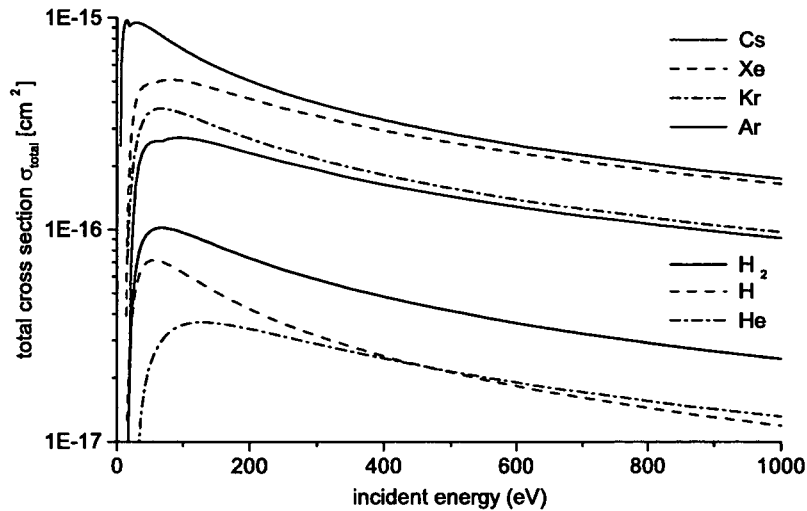


Figure 5.52: Dependence of the total ionisation cross-section σ_{total} on the incident electron energies E_e .

At the CERN H^- source the influence of argon, helium and xenon has been examined. The main difficulty was the control of the very small gas flows, especially for xenon and argon, since a too high concentration causes voltage break down, as has also been observed by Krylov et al. [63] for other gases with a high ionisation cross-section.

5.6.1 Argon

Addition of argon was found to be very detrimental for H^- production at the CERN H^- source, independent of the antenna position, the hydrogen gas flow or the microwave power.

Even small additions of only a few percent of the total gas flow gradually reduce the extracted H^- current (see Figure 5.53).

On the other hand, the electron current at first rises to a maximum before it also decreases (see Figure 5.54). The maximum may be a result of an increased electron density due to multiple ionisation of argon. A too high concentration of argon results in severe break downs of the extraction voltage, limiting the measurements.

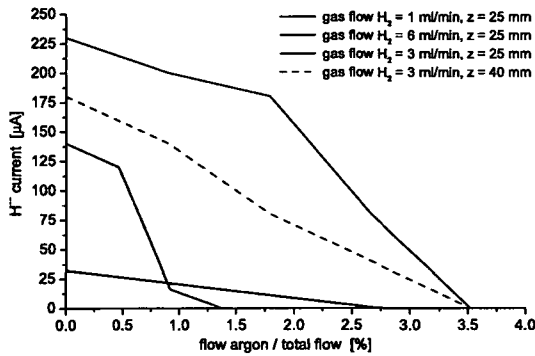


Figure 5.53: Dependence of the H^- current (in μA) on argon addition (multicusp structure, bias voltage +20 V, antenna position $z = 25$ mm).

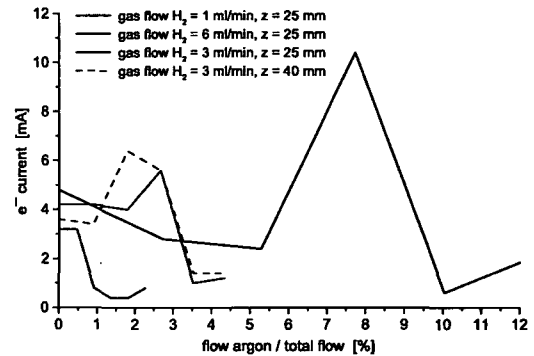


Figure 5.54: Dependence of the electron current (in mA) on argon addition (multicusp structure, bias voltage +20 V, antenna position $z = 25$ mm).

The measurement with argon was repeated both with the solenoidal and the combined structure. In both cases its negative effect was observed again.

5.6.2 Helium

Helium in general shows the same reduction of the H^- yield (except for a hydrogen gas flow of 1 ml/min) as argon, but larger gas additions, compared to argon, have to be inserted to stop the H^- production (see Figure 5.55). This might be a consequence of the higher ionisation energy and the smaller ionisation cross-section.

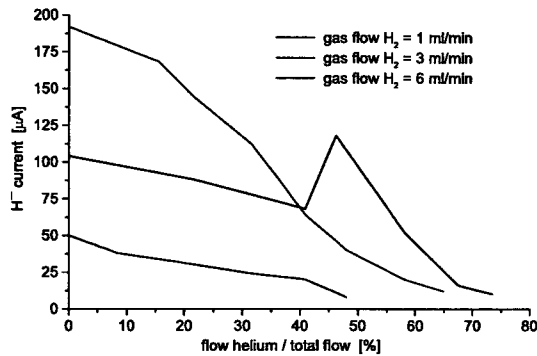


Figure 5.55: Dependence of the H^- current (in μA) on helium addition (multicusp structure, bias voltage +20 V, antenna position $z = 25$ mm).

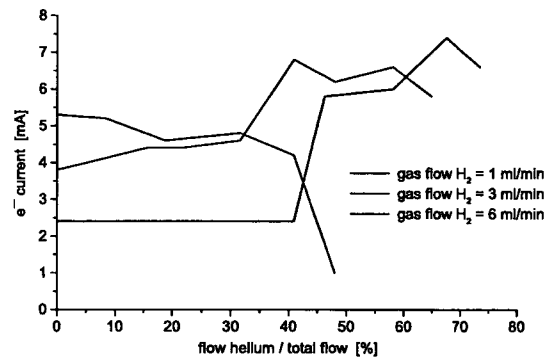


Figure 5.56: Dependence of the electron current (in mA) on helium addition (multicusp structure, bias voltage +20 V, antenna position $z = 25$ mm).

5.6.3 Xenon

Xenon and caesium are quite similar in respect of elastic collisions. Both have comparable large masses and consequently large ion gyroradii, large ionisation cross-sections, and therefore should have a similar diffusion rate, and lower thresholds for ionisation relative to H_2 (see Table 5.3).

As in the case of caesium, xenon also provides a higher density of low energy electrons to the extraction region of the ion source [115]. This increase in electron density probably enhances the H^- ion production.

Multicusp structure

The positive effect of xenon was first observed with the multicusp structure.

After failed attempts to regulate the xenon gas flow at flow rates below 100 $\mu l/min$ to avoid the high voltage break downs, the xenon contaminated source, with the xenon gas flow stopped, yielded a 13 % increased H^- ion current (see Table 5.4).

Also a small reduction in the electron current was observed. The source output returned to its initial value during a period of few hours.

Too high a concentration results in high voltage break downs, similar as for argon.

	$I(H^-)$ [μA]	$I(e^-)$ [mA]	P_{refl} [W]	I_{PE} [mA]
before	184	3.8	43	800
after	208	3.6	43	800

Table 5.4: Difference in the measured source parameters before/after xenon injection (multicusp structure, microwave power 1100 W, bias voltage +20 V, antenna position $z = 30$ mm, H_2 gas flow = 3 ml/min).

Solenoidal structure

With the solenoidal structure and the source tuned to optimum performance, short pulses of xenon were injected and the time dependent changes in H^- ion and electron current observed 5, 10 and 15 ms after the beginning of the microwave pulse (see Figures 5.57 and 5.58).

The xenon gas injection was restricted to a 3 second long pulse with a flow rate of ~ 0.5 ml/min, corresponding to a xenon quantity of ~ 20 mm³. The average H^- ion current increase after the high voltage break down is $\sim 45\%$. The extracted electron current is more or less unaffected. With a hydrogen gas flow of 3 ml/min the xenon injection of ~ 20 mm³ results in a high voltage break down of about 1 minute duration (see Figure 5.59).

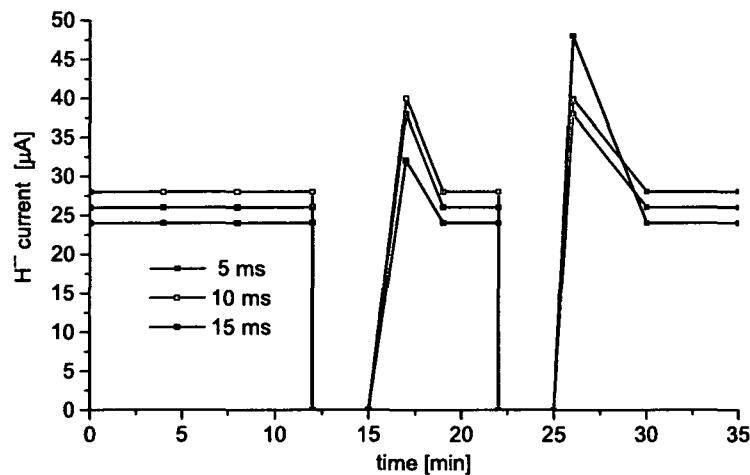


Figure 5.57: Dependence of the H^- current (in μA) on xenon addition (solenoidal structure, microwave power 1100 W, bias voltage +20 V, antenna position $z = 15$ mm, Sol1 = 22 A, Sol2 = 0 A).

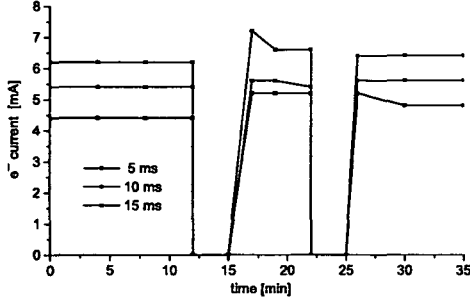


Figure 5.58: Dependence of the electron current (in mA) on xenon addition (solenoidal structure, microwave power 1100 W, bias voltage +20 V, antenna position $z = 15$ mm, Sol1 = 22 A, Sol2 = 0 A).

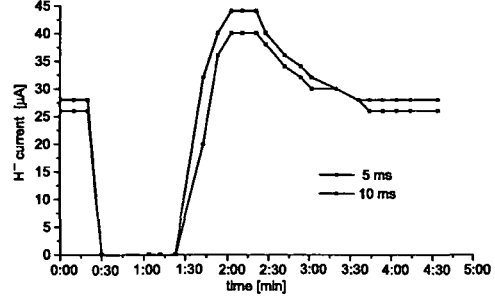


Figure 5.59: Dependence of the H^- current (in μA) on xenon addition (solenoidal structure, microwave power 1100 W, bias voltage +20 V, antenna position $z = 15$ mm, Sol1 = 22 A, Sol2 = 0 A).

Combination of solenoidal and multicusp structure

With the combined structure the xenon contamination of the H^- source had a positive effect (see Table 5.5). After addition of xenon, the extracted H^- current increased up to 60 % of its initial value. Together with the reduction of the electron current from 3.2 to 2.2 mA, this results in a change of the e^-/H^- ratio from 31 to ~ 14 .

	$I(H^-)$ [μA]	$I(e^-)$ [mA]	P_{refl} [W]	I_{PE} [mA]
before	104	3.2	50	460
after	160	2.2	100	750

Table 5.5: Difference in the measured source parameters before/after xenon injection (combined structure, microwave power 1100 W, bias voltage +30 V, antenna position $z = 25$ mm, H_2 gas flow = 5.5 ml/min, Sol1 = 4 A, Sol2 = 2 A)

No definite explanation can be given for the observed influences of the different gases, further theoretical studies and diagnostic work are needed to understand them and therefore, within the framework of the HP-NIS collaboration, the influence of the support gases argon, xenon and krypton was also examined at the H^- ion ECR source at CEA/Saclay, France.

5.7 The influence of different support gases at the CEA/Saclay H^- ion source

The setup of this 2.45 GHz solenoidal ECR source is described in detail in [40], an important feature is the strong dipole magnet allowing a species analysis of the extracted

beam. The spectrometer magnet is equipped with small apertures on both sides, reducing the initial H^- ion current of ~ 2 mA to a few μA .

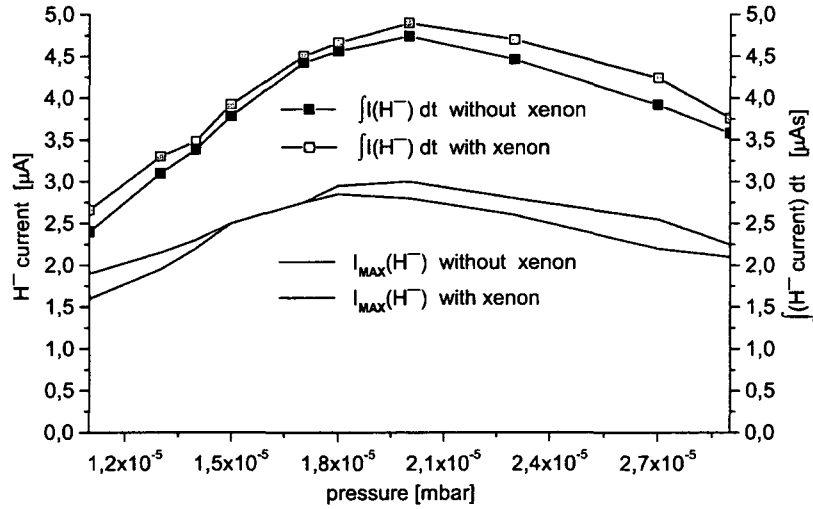


Figure 5.60: Dependence of the H^- current (in μA) and H^- charge (in μAs) on hydrogen pressure with/without a small addition of xenon (solenoidal structure, microwave power ~ 1100 W, bias voltage grid - 102 V).

The valves for the gas injection did not permit a measurement of the gas flow, but their manual operation allowed very fine control and therefore a constant xenon flow instead of the pulsed one at the CERN H^- ion source. As a consequence no xenon concentration can be given.

The influence of a variation of the initial hydrogen pressure on the H^- ion production with and without xenon is shown in Figure 5.60. For each data point the microwave injection was tuned to the maximum H^- ion production. In the case of xenon addition the xenon flow rate was also optimised to this goal.

Again a positive effect on the extracted H^- beam was observed with xenon. The result can be summarized as follows.

When the source is operated below or above a hydrogen pressure of about $1.7 \cdot 10^{-5}$ mbar the addition of xenon shows an improvement of the maximum H^- ion current by up to ~ 19 %. On the other hand, when the source is operated near this pressure, adding xenon does not improve the maximum H^- ion current. This is a similar behavior as reported by Leung et al. [72].

The absolute amount of extracted H^- ions per microwave pulse, therefore the integral of the H^- current over the pulse duration, showed an increase for any hydrogen pressure of up to ~ 10 %.

Contrary to the measurements of Leung et al. and the measurements at the CERN H^- ion source, the extracted electron current is unaffected by the xenon addition.

The influence of a variation of the initial hydrogen pressure on the H^- ion production with and without krypton is shown in Figure 5.61.

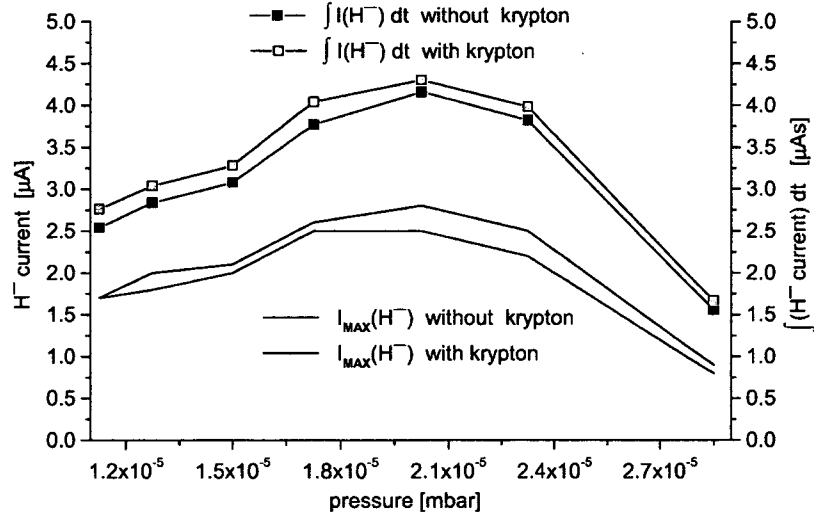


Figure 5.61: Dependence of the H^- current (in μA) and H^- charge (in μAs) on hydrogen pressure with/without a small addition of krypton (solenoidal structure, microwave power ~ 1100 W, bias voltage grid - 102 V).

For krypton both an increase of the maximum H^- ion current of up to ~ 13 %, and an increase of the absolute amount of extracted H^- ions per microwave pulse, up to ~ 8 %, is observed for all hydrogen pressures.

Also an argon - hydrogen mixture was tried, without any measurable effect on the H^- beam.

Especially for argon the results achieved so far are not conclusive, since they range from an enhanced H^- ion production [63] to no significant influence (CEA/Saclay) to steady reduction of the source yield [103].

Chapter 6

The Low Energy Beam Transfer Line

The connecting structure between the source and the linear accelerator is called LEBT (Low Energy Beam Transfer). Its main function is to match the extracted H^- ion beam from the source into the subsequent accelerator structure, the RFQ (Radio Frequency Quadrupole). To give the beam the desired radial size and divergence, at least two lenses are required.

Further functions of the LEBT are the magnetic or electrical beam steering and the differential pumping of the gas emitted from the source. The LEBT also houses the different diagnostic systems for current and profile measurements and, in CERN's case, maybe a pre-chopper with a dump to remove unwanted particles still at a low beam power.

6.1 LEBT types

To achieve these goals different LEBT types can be used, working either with magnetic or electric fields [61]. The characteristics of the different lay-outs are compared in the following.

Magnetic LEBT

Most sources are equipped with a magnetic LEBT, using at least two solenoids, for example ISIS at Rutherford [12, 73], at the University of Frankfurt [55, 56, 57] and Desy [84], or both linear accelerators at CERN [74, 86].

advantages:

- a high grade space charge compensation through the auxiliary gas
- the exact control of the beam for matching and steering
- experience, widely used

problems:

- a severe emittance growth
- the losses through charge exchange (stripping)

The length of these magnetic LEBTs varies from 1 to 4 m, with transmission rates of 70 % (ISIS [73]) to 90 % (CERN Linac2 [44]).

Electrostatic LEBT

A LEBT working purely on an electrostatic focussing principle was built at Berkeley for the Spallation Neutron Source (SNS) [60, 99, 117].

The big advantage in using electric fields is the resulting shortness, for a 35 mA H^- ion beam at 65 keV the complete two lens system is about 15 cm long.

For steering in both angle and displacement and for pre-chopping, pulsed voltage signals and independent DC potentials can be applied to the four quadrants of the center electrode of the second lens (see Figure 6.2). The chopped beam is then dumped onto the entrance flange of the RFQ (see Figure 6.1).

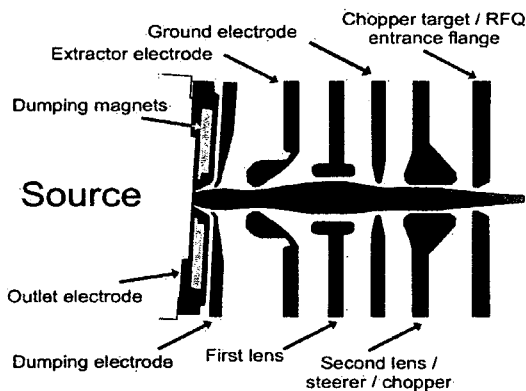


Figure 6.1: The SNS electrostatic two electrode system [60].

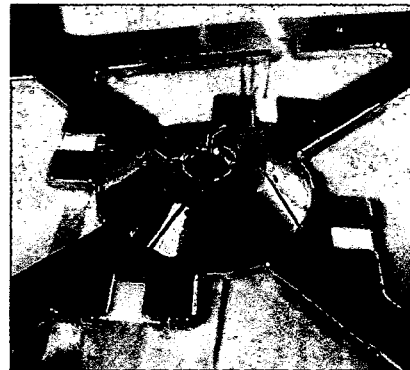


Figure 6.2: The split chopper electrode [100].

advantages:

- no space charge compensation is needed
- short and compact
- a small emittance growth
- provides a larger cross-sectional area for pumping

problems:

- the frequent sparking is a serious drawback
- very sensitive to any misalignment
- the electron heating of the support structure and the electrodes due to particle losses

Direct injection scheme

Another possibility would be the complete abandonment of the LEBT and the direct injection into the RFQ. This method, called DPIS – direct plasma injection scheme – is used at the laser ion source at RIKEN [78, 105].

advantages:

- no explicit electron dumping is needed
- very small losses in the transition
- the immediate acceleration of particles - space charge of small consequence

problems:

- no diagnostics are available
- electron losses in the RFQ
- no steering or matching capabilities
- source plasma not always stable, can not be corrected

6.2 LEBT for the H^- source at CERN

For the LEBT at the CERN H^- ion source, due to the reasons given above, a magnetic LEBT with 2 solenoids was proposed. The LEBT should match the H^- ion beam, extracted at 95 keV¹, to the RFQ with an emittance of 0.25π mm·mrad rms normalised² with $\alpha = 1.2$ and $\beta = 0.0587$ mm/mrad.

The total length of the LEBT has to be below 2 m, with the distance between the two solenoids as long as possible to allow the installation of diagnostic equipment and a possible pre-chopper.

For the pre-chopper to achieve a sufficient separation of the 95 keV beam of about 2.5 times the beam radius, the plates of the electrical pre-chopper, with 5 kV per plate and 6 cm distance between them, have an effective length of about 230 mm.

Subsequent to the pre-chopper a drift of about 30 cm to the second solenoid (SolB) is needed, giving the pre-chopper a total length of about 50 cm. A length of ~ 1 m would therefore be desired between the two solenoids.

¹Source parameters changed, initially 100 keV.

²RFQ parameters changed, initially 0.28π mm·mrad rms normalised

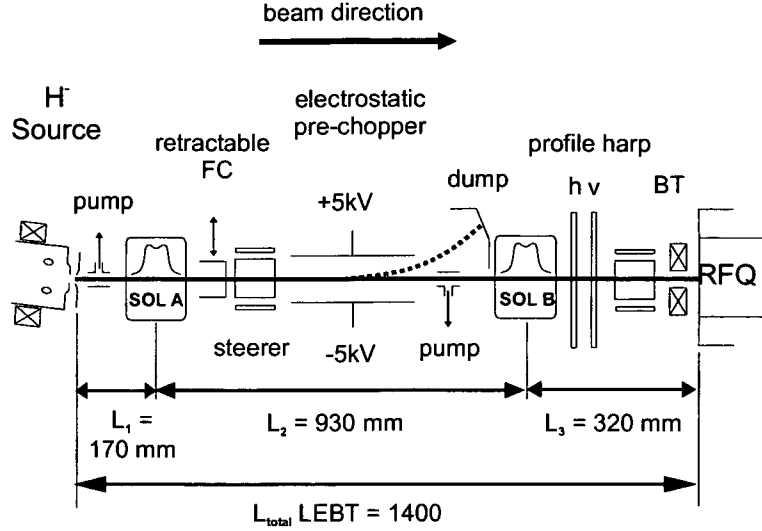


Figure 6.3: LEBT scheme, with a selection of possible diagnostics (FC – Faraday Cup, BT – beam transformer, h – horizontal, v – vertical).

The drift in front of the first solenoid (SolA) has to be long enough to install a vacuum pump and maybe magnetic steerers. This length together with the source divergence will define the acceptance of the LEBT.

For diagnostic measurements 2 Faraday Cups (FC), one retractable and one fixed as a possible beam dump, replacing the RFQ before the actual operation during the measurements at the source itself, a current transformers after Solenoid B and a profile harp or phosphor screen for beam profile measurements should be considered (see Figure 6.3). An emittance meter or a spectrometer to measure the energy spread might also be useful.

Two different solenoids, one of each type, with apertures of 50 and 60 mm diameter, called solenoid Type 1 and 2, could be found at CERN, together with the necessary 1 kA power supplies, and were checked for their suitability.

	$\phi_{aperture}$ [mm]	L_{real} [mm]	L_{eff} [mm]	wire [mm]	turns
Sol Type 1	50	180	110	12.8 x 2.54	120
Sol Type 2	60	190	130	15.3 x 3.85	80
Sol Type 3	60	220	180	17.8 x 4.8	180

Table 6.1: Design parameters for different solenoids. Type 1 and Type 2 already exist at CERN.

Magnetic field simulations were done using POISSON [66] (see Table 6.1 and Figures 6.4 and 6.5) as either the effective magnetic length or magnetic field maps of the solenoids are needed for both programs calculating the beam propagation, TRACE [107] and PATH [109]. Other solenoids with different effective lengths were examined as well.

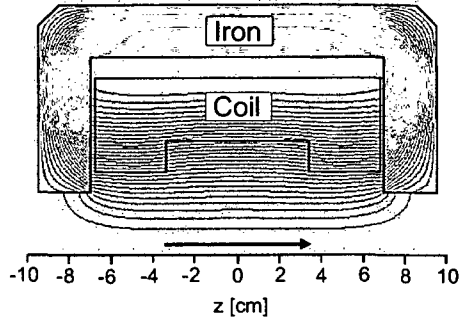


Figure 6.4: Magnetic field plot of the Type 2 solenoid. 80 kA·turns calculated for this 80 turn solenoid.

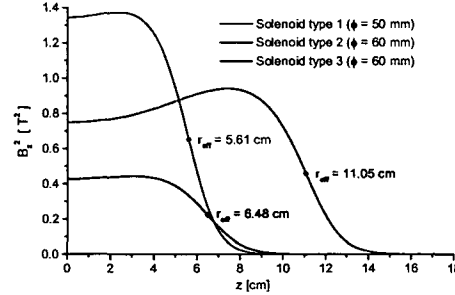


Figure 6.5: B_z^2 (z along solenoid axis) and the corresponding effective radius for the different solenoid types. Note that the focussing force is $\propto B_z^2 \cdot L$.

6.2.1 Basic decisions on the LEBT layout

The first studies were done using the TRACE 2-D code [107]. Since the beam characteristics from the source have to be guessed, to be on the safe side an unnormalised source emittance of 100π mm·mrad, resulting in 0.356π mm·mrad rms normalised, and two different diameters for the extraction opening were used (see Table 6.2), with $\phi_{\text{extraction}} = 2 \cdot x_{\text{max}}$ and $x_{\text{max}} = \sqrt{\epsilon \beta}$.

x_{max} [mm]	$\epsilon_{x,y}$ (rms, norm)	$\epsilon_{x,y}$	$\alpha_{x,y}$	$\beta_{x,y}$
7	0.356π mm·mrad	100π mm·mrad	0	0.49
2.5	0.356π mm·mrad	100π mm·mrad	0	0.0625

Table 6.2: Assumed output parameters of the H^- ion source.

For a first check if the requirements mentioned above could be met, a non divergent beam and ideal solenoids were assumed.

The simulations showed that the use of both existing solenoid types would be possible, but that the smaller 50 mm aperture of solenoid Type 1 is limiting the maximum distance between the solenoids (length L_2). With two solenoids of Type 2, therefore with an aperture of 60 mm diameter, this distance could be more than doubled to ~ 90 cm (see Figure 6.6).

Solenoids with a longer effective length reduce the magnetic field necessary for focussing the beam, but give only a slight increase in the length between the solenoids.

The desired flux densities of ~ 0.8 T should pose no problem for the pulsed power supplies which can provide up to 1 kA, with the Type 2 solenoid producing a magnetic flux density of ~ 1.1 mT per Ampere.

Favouring the Type 2 solenoid, it was tried to create a waist by focussing the beam between the solenoids. This might have advantages for the diagnostic set-up.

A configuration was found that could even match a highly divergent beam ($\alpha = -7 \approx 5.8$ degrees) from the source into the RFQ, both with and without a waist (see Figures 6.7

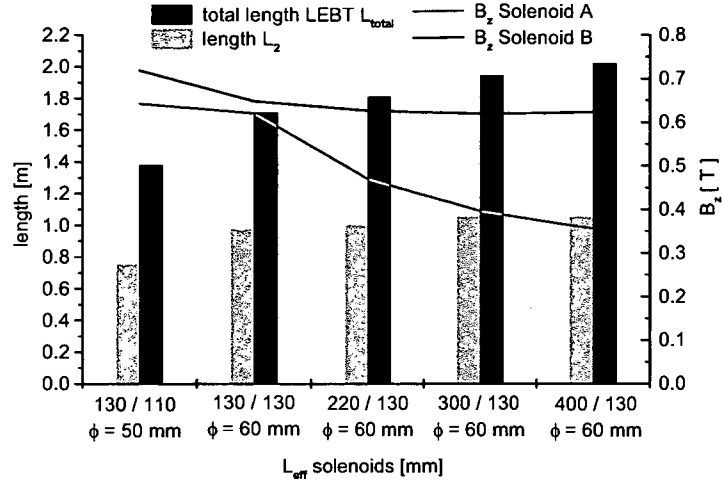


Figure 6.6: Dependence of the total LEBT length L_{total} and the length L_2 between the two solenoids (center to center) on the used solenoid type. The lines indicate the necessary magnetic field for matching into the RFQ ($x_{\text{max}} = 2.5 \text{ mm}$, 100 keV).

and 6.8). For this layout the distance between both solenoid centers is $\sim 800 \text{ mm}$, with $\sim 120 \text{ mm}$ in front of the first solenoid for pumping. This length from the source to the first solenoid is especially important, since together with the source divergence it defines the LEBT acceptance.

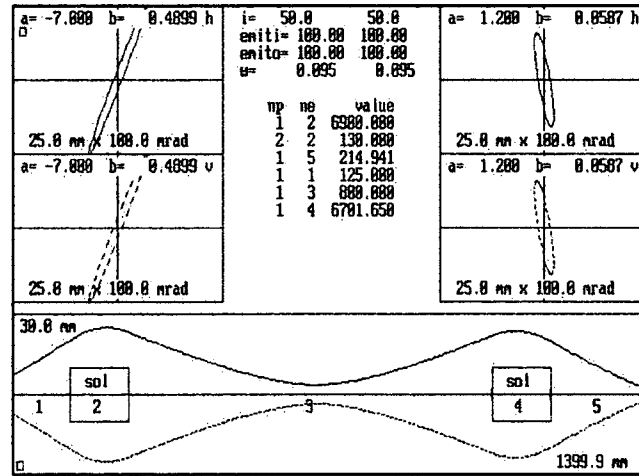


Figure 6.7: The beam envelope of the LEBT layout with a waist ($x_{\text{max}} = 7 \text{ mm}$, 95 keV).

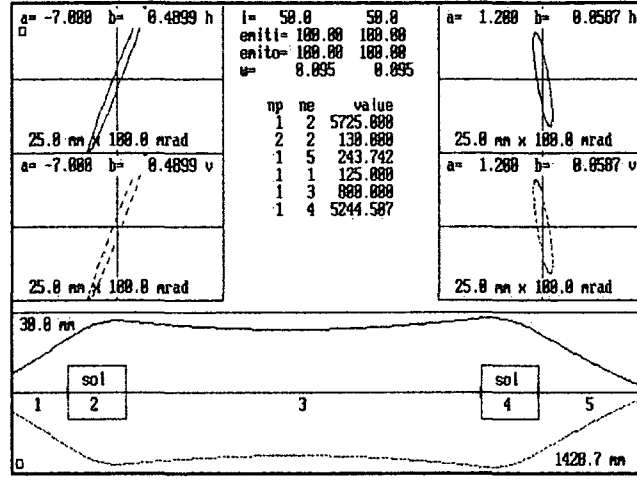


Figure 6.8: The beam envelope of the LEBT layout without a waist ($x_{max} = 7$ mm, 95 keV).

6.2.2 Multi-particle tracking through the LEBT

With the possibilities of the TRACE program exhausted, the so far achieved lay-out was further developed using the multi-particle tracking program PATH [109]. Starting with approximately the same distances and ideal solenoids with an effective length of 130 mm, simulations with and without a waist in between the two solenoids showed that the waist is to be avoided since it significantly increases the transverse emittance (see Figure 6.9). For an initially square beam with a Gaussian distribution, the emittance increase is ~ 70 % with a waist and ~ 30 % without.

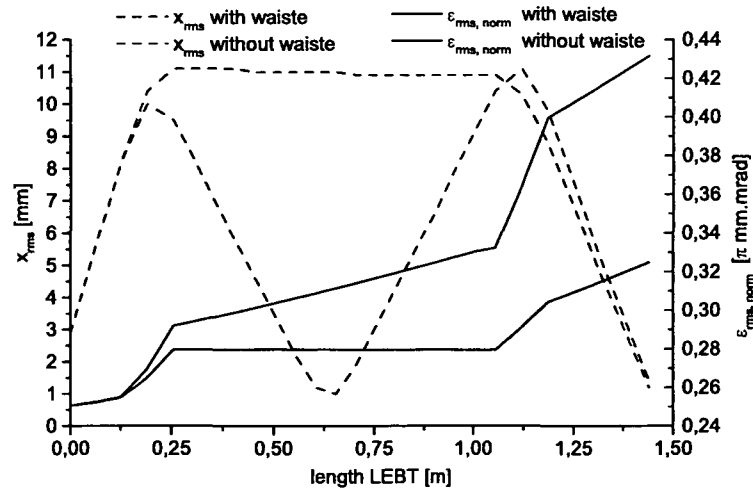


Figure 6.9: Dependence of the emittance growth on the focussing of Solenoid A (square beam, Gaussian distribution).

$\epsilon_{x,y} (1rms)$	$17.4 \pi \text{ mm}\cdot\text{mrad}$
$\epsilon_{x,y} (1rms, norm)$	$0.247 \pi \text{ mm}\cdot\text{mrad}$
$\alpha_{x,y}$	-4.16
$\beta_{x,y}$	1.19 mm/mrad
beam energy	95 kV
energy spread	$\pm 0.5 \%$
beam current	50 mA
macro particles	39000

Table 6.3: Input parameters at the aperture for a round and uniform beam.

The 30 % in the best case come from the energy spread, therefore a chromatic effect of the focussing, especially in Solenoid B. Aberrations are highly dependent on the beam radius in the solenoids, hence a larger aperture design would be a possibility to reduce the emittance growth.

The ideal solenoids were replaced by more realistic fields maps, calculated from POISSON, leading to an increased emittance growth of $\sim 50 \%$. By adjustment of the field strengths and the distances, especially L_1 – the drift into the first solenoid – the emittance growth could be reduced back to the initial 30 %.

In addition the square beam with a Gaussian distribution was replaced by a round, uniform beam with realistic beam input conditions, and the emittance reduced from 0.356 to $0.25 \pi \text{ mm}\cdot\text{mrad}$ rms normalised.

Emittance measurements at the SILHI proton source at the CEA/Saclay resulted in values of $\alpha = -14.7$, $\beta = 10.1 \text{ mm/mrad}$ and $\epsilon_{(1rms, norm)} = 0.165 \pi \text{ mm}\cdot\text{mrad}$, measured 53 cm after the source plasma electrode [39].

Tracking backwards, using PATH, leads to values of $\alpha = -4.18$, $\beta = 1.19 \text{ mm/mrad}$ assuming 95 % space charge compensation of the 120 mA beam, 5 cm away from the plasma electrode.

Generation of this beam in PATH requires slightly modified input conditions and a round aperture to avoid the square beam. With $\alpha = -5.1$, $\beta = 1.46 \text{ mm/mrad}$ and $\epsilon_{(1rms, un-norm)} = 19 \pi \text{ mm}\cdot\text{mrad}$, 50.000 macro-particles and a current of 64.1 mA, the beam conditions at the round aperture match the requirements (see Table 6.3). The energy spread is limited to $\pm 0.5 \%$.

6.2.3 Space charge compensation

Space charge compensation of negative ion beams is realised in the simplest way by the positive ions formed as a result of the residual gas ionisation by the beam itself.

Using the lengths quoted in Table 6.4, after proving that a matching to the RFQ is possible, the influence of space charge compensation in the LEBT was examined.

Tables 6.6 to 6.8 show the results for different beam currents, therefore different compensation percentages. Three compensation fractions are considered: 0 %, 50 % and

$\phi_{aperture}$	18.2 mm
aperture – center Solenoid A (L1)	170 mm
Solenoid A (CERN Type 2)	· 240 mm field map
	· real external length 190 mm
center Solenoid A – Solenoid B (L2)	930 mm
Solenoid B (CERN Type 2)	· 240 mm field map
	· real external length 190 mm
centre Solenoid B – output (L3)	320 mm

Table 6.4: Longitudinal dimension of individual LEBT parts.

90 %. Without space charge compensation, the transversal emittance growth per plane is ~ 60 %, at 50 % compensation it is ~ 10 % and only ~ 2 % at 90 % compensation.

The emittance growth is still small for 50 % compensation and then grows rapidly with smaller compensation fractions. With a small compensation it is not possible to keep the beam size small in the second solenoid where most of the emittance growth occurs.

Using the distance L_3 from the second solenoid to the RFQ as an additional matching parameter, the reduced beam size in the second solenoid resulted in a smaller emittance growth of ~ 26 % (see Table 6.9).

Shortening the distance L_2 between the solenoids might result in a reduction too but is not an option, due to the space requirements for steering and diagnostics.

In summary, the emittance growth of a uniform, circular beam can be kept small in the LEBT if several conditions are fulfilled:

The beam size in the first solenoid has to be controlled by the extraction system and the ability to keep L_1 short. The space charge compensation should be better than 90 %. For this a gas injection should be foreseen to reach the required pressures (see Chapter 6.2.4).

As mentioned above, space charge compensation is achieved via ionisation of the residual gas in the beam line. In this process of collisions not only ions are formed, but electrons as well [97].

At low gas pressures these electrons are extracted from the beam volume by the electric field and their concentration is non-essential. Only at high gas pressures, when the concentration of positive ions starts to overcome the beam concentration, the field changes its sign and starts holding slow electrons in the beam region.

The critical gas pressure, at which the system is transferred from a two-component to a three-component one and the beam is overcompensated, can be obtained from the balance equations for the ions and electrons and the quasi-neutrality and equals

$$n_0 \approx \frac{2v_i}{v_- r_0 \sigma_i} \quad (6.1)$$

with v_i as the velocity of the positive plasma ions and v_- as the velocity of the negative beam ions. The beam radius is r_0 and σ_i the ionisation cross-section of the residual gas. This three-component system can result in electron oscillations and therefore oscillations in the compensation degree. To avoid this the pressure in the LEBT should be controllable.

Soloshenko found as critical pressure value for a 15 keV H^- ion source $\sim 6.5 \cdot 10^{-5}$ mbar [97]. Using his results ($\sigma_i = 10 \cdot 10^{-16} \text{ cm}^2$, $\beta = 0.00565$, $r_0 \sim 4 \text{ mm}$) and formula (6.1) for a 95 keV H^- ion source the critical pressure would be at $\sim 2.5 \cdot 10^{-5}$ mbar. With a beam radius of about 1 cm in the solenoids the critical pressure would be $\sim 7 \cdot 10^{-6}$ mbar.

Baartman et al. [7] found a neutralisation level of 97 % at $\sim 1.8 \cdot 10^{-5}$ mbar, with a slight overcompensation at $\sim 1.6 \cdot 10^{-4}$ mbar (50 %/m stripping losses). Sherman et al. [92] found similar results.

6.2.4 Gas stripping losses

A pressure in the region of 10^{-5} mbar, necessary for high compensation fractions, may well lead to non-negligible stripping losses. Values for the electron detachment of H^- ions in the region of 100 keV for different possible residual gasses are giving in Table 6.5. The ionisation cross-sections are collected from different sources [3, 6, 48].

$\sigma_i(X):$	$\sigma_i(H_2)$	$\sigma_i(He)$	$\sigma_i(N_2)$	$\sigma_i(Ar)$	$\sigma_i(Ne)$	$\sigma_i(Kr)$	$\sigma_i(Xe)$
$\cdot 10^{-16} \text{ cm}^2$	4	2.01	9.23	8.4	4.2	11.5	11.3

Table 6.5: Electron detachment cross-sections σ_i for different support gasses for H^- ions at 100 keV).

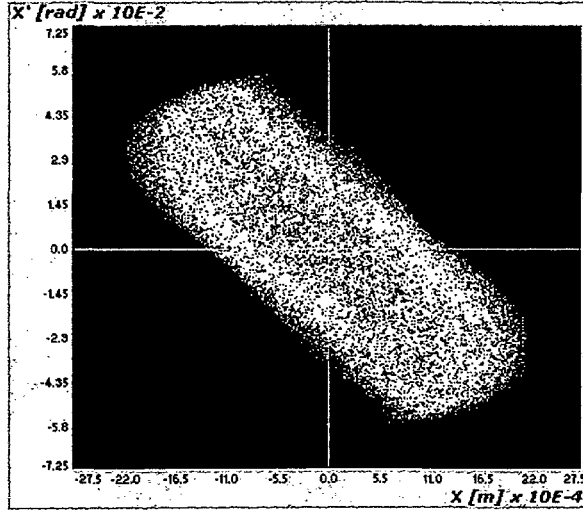
The mean free path length is given by

$$\lambda = \frac{1}{n_0 \sigma_i} = \frac{kT}{p \sigma_i} \quad (6.2)$$

and for $\sigma_i = 10 \cdot 10^{-16} \text{ cm}^2$ and a pressure of $2.5 \cdot 10^{-5}$ mbar in the region of $\lambda \approx 16 \text{ m}$ (for a pressure of $7 \cdot 10^{-6}$ mbar $\lambda \approx 60 \text{ m}$).

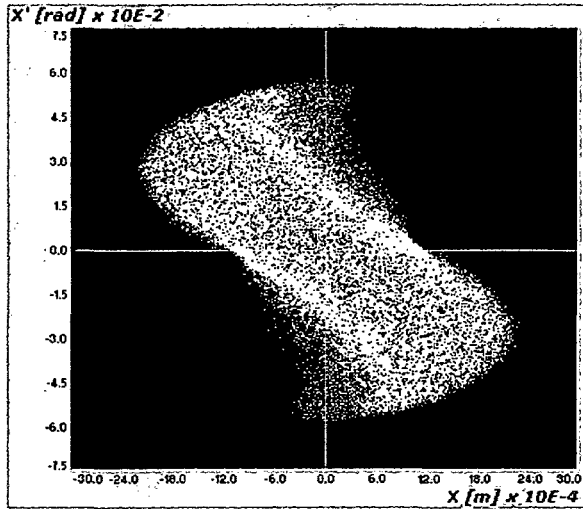
For a 1.4 m long LEBT this would result in stripping losses of $\geq 8 \%$. With a critical pressure in the order of $1 \cdot 10^{-5}$ mbar and gasses with lower cross-sections, like Helium, this could be significantly reduced, to $\leq 1 \%$.

The cross-sections for double electron detachment, from H^- to H^+ , are typically an order of magnitude smaller at low energies, nevertheless, a small proton beam might have negative effects on a high intensity accelerator.



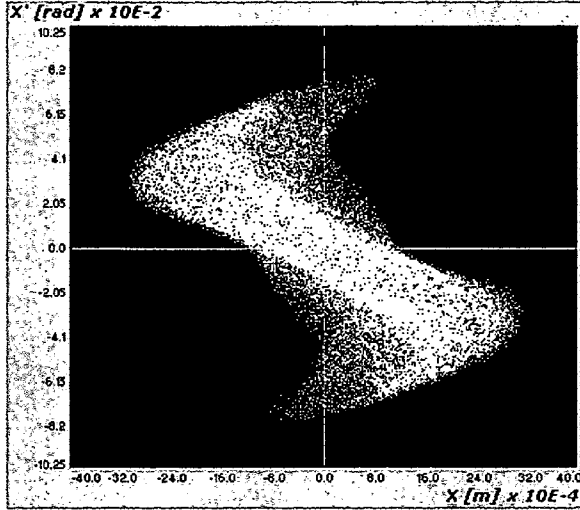
ϵ_x (1rms, norm)	0.2534π mm·mrad
ϵ_x (90 %, norm)	0.892π mm·mrad
α_x	1.16
β_x	0.0577 mm/mrad
ϵ_y (1rms, norm)	0.2547π mm·mrad
ϵ_y (90 %, norm)	0.895π mm·mrad
α_y	1.16
β_y	0.0576 mm/mrad
$\Delta\epsilon_x$	~ 3 %
$\Delta\epsilon_y$	~ 3 %

Table 6.6: The beam transverse phase space after the LEBT with 90 % space charge compensation (Solenoid A = 560 A, Solenoid B = 702 A, round, uniform beam, 95 keV, 39000 particles).



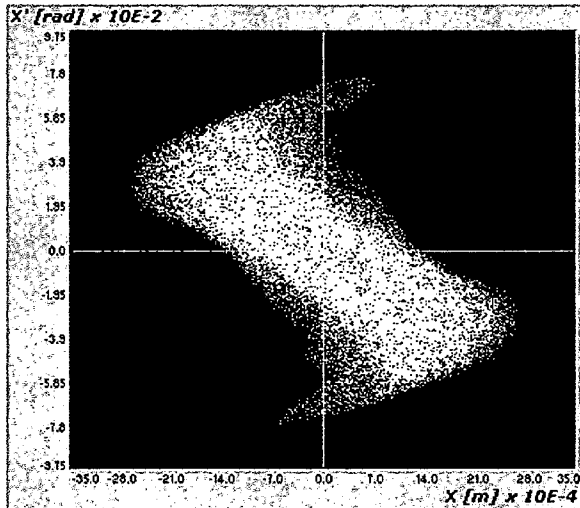
ϵ_x (1rms, norm)	0.276π mm·mrad
ϵ_x (90 %, norm)	1.048π mm·mrad
α_x	0.984
β_x	0.0519 mm/mrad
ϵ_y (1rms, norm)	0.275π mm·mrad
ϵ_y (90 %, norm)	1.0496π mm·mrad
α_y	0.973
β_y	0.0516 mm/mrad
$\Delta\epsilon_x$	~ 12 %
$\Delta\epsilon_y$	~ 11 %

Table 6.7: The beam transverse phase space after the LEBT with 50 % space charge compensation (Solenoid A = 680 A, Solenoid B = 784 A, round, uniform beam, 95 keV, 39000 particles).



ϵ_x (1rms, norm)	0.394π mm·mrad
ϵ_x (90 %, norm)	1.66π mm·mrad
α_x	1.257
β_x	0.0678 mm/mrad
ϵ_y (1rms, norm)	0.392π mm·mrad
ϵ_y (90 %, norm)	1.654π mm·mrad
α_y	1.265
β_y	0.0677 mm/mrad
$\Delta\epsilon_x$	~ 60 %
$\Delta\epsilon_y$	~ 59 %

Table 6.8: The beam transverse phase space after the LEBT with 0 % space charge compensation (Solenoid A = 780 A, Solenoid B = 810 A, round, uniform beam, 95 keV, 39000 particles).



ϵ_x (1rms, norm)	0.314π mm·mrad
ϵ_x (90 %, norm)	1.21π mm·mrad
α_x	1.15
β_x	0.056 mm/mrad
ϵ_y (1rms, norm)	0.316π mm·mrad
ϵ_y (90 %, norm)	1.236π mm·mrad
α_y	1.16
β_y	0.0565 mm/mrad
$\Delta\epsilon_x$	~ 27 %
$\Delta\epsilon_y$	~ 28 %

Table 6.9: The beam transverse phase space after the LEBT with 0 % space charge compensation for a shorter distance L3 (L3 = 300 mm, Solenoid A = 830 A, Solenoid B = 864 A, round, uniform beam, 95 keV, 39000 particles).

Chapter 7

Conclusions and future plans for the H^- ion production at CERN

Construction of an H^- ion source prototype, using some non standard approaches, and the setup of its infrastructure was carried out. The first H^- ions were extracted from a microwave driven source at CERN in 2004.

Flexibility in the magnetic field configuration allowed a systematic observation and direct comparison of different magnetic field setups and their influence on the H^- ion yield of the source.

Variation of the main source parameters, e.g. microwave power, hydrogen gas flow, antenna position and plasma electrode polarisation, allowed a complete analysis of the parameter space which permitted in an increase of the ion-current.

The maximum extracted H^- ion current was ~ 0.3 mA with an electron current of 4.6 mA, therefore an e^-/H^- ratio of 15, using the 1.5 kW microwave generator (pulse length 10 ms, repetition rate 1 Hz) with the magnetic multicusp structure.

This multicusp structure, together with a small additional solenoidal field in the extraction region, brought an increase in the H^- ion yield of ~ 40 %, although the maximum extracted H^- current could not be raised above 0.3 mA due to the replacement of the magnetron with a resulting reduction of the microwave power to 1.2 kW.

The solenoidal structure with its strong magnetic field yielded only small H^- ion currents, which probably is the result of too hot a plasma. Also the magnetic filter field might be too small, compared to the solenoidal field, for sufficient reflection of the hot electrons away from the H^- production region.

This result, in combination with own observations, prompted the staff in charge of the solenoidal H^- ion source at the CEA/Saclay to convert their source to a multicusp setup.

Various experiments, reported to have a positive effect on H^- ion production at individual sources, were carried out .

With a tantalum wall coverage an increase of H^- ion yield of ~ 30 % was observed for the multicusp structure. The ECR heating on a boron nitride surface brought a small improvement, though with reservations, and should be repeated.

An increase of the H^- ion yield observed for a collar at DESY or a grid at CEA/Saclay on the other hand could not be repeated at CERN. Additional theoretical work in the future may give an explanation for this different behavior.

The influence of different support gases (helium, argon, xenon) was studied, resulting in an H^- ion gain of up to 60 % for xenon. This discovery could later be confirmed at CEA/Saclay where the same effect could be found for krypton as well.

A proposal was made for a possible Low Energy Beam Transfer line, consisting of two solenoids with a total length of <2 m. Multi-particle simulations showed its capability to transport and focus the H^- ions from the source into the subsequent accelerator structure, the RFQ. The layout was approved and included into the layout of the 3 MeV test stand.

This thesis will also be the foundation for a decision on the future strategy concerning H^- ion production at CERN.

The total H^- ion current of the prototype is small compared to the requirements of a final Linac4/SPL H^- ion source¹ and probably can not be increased within the next design step to reach the specifications in time.

Nevertheless, important experience has been gathered for a possible second generation source, to be built at CERN, or for a decision on another existing source and its upgrade. For the design of a next generation H^- ion source the following recommendations should be considered.

In principle the concept of keeping the whole source and most of the support systems on high voltage is unnecessary and should be abandoned. Putting only the plasma chamber on high voltage would result in a simpler power delivery, especially if the aim is DC operation of the source.

The plasma chamber itself should incorporate the cooling system in its body and, if possible, be made up of several parts so that variations in its longitudinal dimension are possible.

Since a spatial potential in the extraction region proved to be highly effective, the additional installation of a grid, biased negatively with respect to the chamber and working as a kind of high pass filter for hot electrons, should be foreseen. The functionality of this design will be tested at the existing H^- ion source.

The position of a stronger magnetic filter should be variable along the central axis of the plasma chamber and the installation of a Langmuir probe in the different plasma regions might allow some plasma diagnostic work.

Liners for different wall materials (e.g. tantalum) might prove effective as well.

The basic magnetic field should be provided by permanent magnets in a multicusp constellation, with an additional solenoidal field to allow variations in magnetic field strength. The injection of microwave power with an antenna, as installed at the prototype source, is advantageous since it allows a good tuning to the plasma and shows low power reflection coefficients.

For further use with a broader tuning range, problems resulting from the rigidity of the 1 kW coaxial cables and the overheating of the vacuum feed-through, which prevents continuous operation of the source, would have to be solved.

Taking into account the limited time span until the commissioning of the 3 MeV test stand and the risks associated with new source development, a decision towards the copy

¹Maximum H^- ion current for the SPL changed from > 40 to 65 mA [35] at a pulse length of 1.5 ms at a repetition rate of 50 Hz.

and the upgrade of a source already operating near the demanded source parameters might be preferable.

A possible candidate would be the magnetron negative ion source of Brookhaven National Laboratory, since it requires only a small emittance reduction, or the DESY RF source. Also the choice not to involve caesium should be reconsidered. Caesium is commonly used and would significantly enhance the extracted H^- ion current.

Bibliography

- [1] J.G. Alessi, A. Herscovitsch and T. Sluyters, Rev.Sci.Instr. **55** (1984) 8-11.
- [2] J. Alessi, 20th ICFA Advanced Beam Dynamics Workshop, <http://www-bd.fnal.gov/icfa/workshops/20/> (last checked 22.04.2005).
- [3] C.J. Anderson, R.J. Girnius, A.M. Howald and L.W. Anderson, Phys.Rev.A. **22** (1980) 822-833.
- [4] <http://www.anl.gov/> (last checked 22.04.2005).
- [5] <http://www.ansys.com/> (last checked 10.04.2005).
- [6] <http://www-amdis.iaea.org/cgi-bin/ALADDIN/> (last checked 10.04.2005).
- [7] R. Baartman and D. Yuan, Space Charge Neutralization Studies of an H^- Beam, 1st European Particle Accelerator Conference, EPAC (1988) 949.
- [8] M.Bacal and G.G. Hamilton, Phys.Rev.Lett. **42** (1979) 1538-1540.
- [9] M. Bacal and D. Skinner, Comm.At.Mol.Phys. **23** (1990) 283.
- [10] M. Bacal et al., Rev.Sci.Instr. **75** (2004) 1699-1703.
- [11] M. Bacal et al., Rev.Sci.Instr. **59** (1988) 2152-2157.
- [12] C.P. Bailey, J.P. Duke, A.P. Letchford, J.W.G. Thomason, Results from the ISIS RFQ test stand, Proceedings of the 8th European Particle Accelerator Conference, Paris, France (2002) 867-869.
- [13] El Balghiti-Sube et al., Rev.Sci.Instr. **67** (1996) 2221.
- [14] Y. Belchenko and V. Savkin, Rev.Sci.Instr. **75** (2004) 1704-1708.
- [15] M. Benedikt, K. Cornelis et al., Report of the High Intensity Protons Working Group, CERN-AB-2004-022 OP/RF, Geneva, Switzerland (2004). ,
- [16] <http://www.bnl.gov/world/Default.asp> (last checked 22.04.2005).
- [17] J. Bruneteau et al., Proceedings of the 5th Intern. Symposium on Production and Neutralization of Negative Ions and Beams, Brookhaven, NY, USA, AIP-Conference-Proceedings **210** (1990) 266-277.

- [18] CERN Accelerator School, Proceedings of the Fifth General Accelerator Physics Course, CERN 94-01, University of Jyväskylä, Finland (1992).
- [19] R. Celiberto and A. Laricchiuta, Electron-impact cross sections for processes involving vibrationally excited diatomic hydrogen molecules, Proceedings of the 9th International Symposium on the production and neutralisation of negative ions and beams, Gif-sur-Yvette, France (2002) 3-12.
- [20] L. Celona, G. Ciavola, S. Gammino et al., *Rev.Sci.Instr.* **75** (2004) 1423-1426.
- [21] G. Ciavola, L. Celona, S. Gammino et al., *Rev.Sci.Instr.* **75** (2004) 1453-1456.
- [22] <http://www.cea.fr/> (last checked 22.04.2005).
- [23] F.F. Chen *Electric Probes in Plasma Diagnostic Techniques*, Ed. R. H. Huddleston and S. L. Leonard, Academic Press, NY, USA (1965).
- [24] http://www.chem.qmw.ac.uk/surfaces/scc/scat5_3.htm (last checked 10.04.2005).
- [25] C. Courteille, A.M. Bruneteau and M. Bacal, *Rev.Sci.Instr.* **66** (1995) 2533.
- [26] <http://www.cst.com/> (last checked 22.04.2004).
- [27] <http://www.desy.de/html/home/> (last checked 22.04.2005).
- [28] <http://www.fnal.gov/> (last checked 22.04.2005).
- [29] A.T.Forrester, *Large Ion Beams*, ISBN 0-471-62557 (1988).
- [30] Fukumasa et al., *Appl.Phys.* **20** (1987) 237-240.
- [31] I.S.K. Gardner, G.H. Rees, C.M. Warsop et al., Status of the European spallation source design study, 17th IEEE Particle Accelerator Conference (PAC 97), Vancouver, BC, Canada (1997) RAL-TR-97-030C.
- [32] R. Garoby, A New Proton Injector at CERN, CERN-AB-2003-048 (SPL), Geneva, Switzerland (2003).
- [33] R. Garoby et al., LINAC4, a new H^- Linear Injector at CERN, CERN-AB-2005-012, Geneva, Switzerland (2005).
- [34] R. Garoby, The Potential of the SPL at CERN, CERN-AB-2005-006, Geneva, Switzerland (2005).
- [35] R. Garoby, The SPL at CERN, AB-Note-2005-007, Geneva, Switzerland (2005).
- [36] R. Geller, *Electron cyclotron resonance ion sources and ECR plasmas*, ISBN 0-7503-0107-4, IOP Publishing (1996).
- [37] R. Gobin et al., Proceedings of the 9th Intern. Symposium on Negative Ion Sources and Beams, Saclay, France, AIP Conference Proceedings (2002) 639-177.
- [38] R. Gobin, Private communications, Saclay, France (2004).

- [39] R. Gobin, Private communications, Saclay, France (2005).
- [40] R. Gobin et al., *Rev.Sci.Instr.* **73** (2002) 983-985.
- [41] R. Gobin et al., *Rev.Sci.Instr.* **75** (2004) 1741.
- [42] R. Gobin et al., *Rev.Sci.Instr.* **75** (2004) 1414-1416.
- [43] P. Grübling, J. Holland and G. Ulm, *Rev.Sci.Instr.* **73** (2002) 614-616.
- [44] C.E. Hill, Private communications, CERN, Geneva, Switzerland (2005).
- [45] C.E. Hill, D. Kuchler, R. Scrivens and T. Steiner, H^- source developments at CERN, H^- -workshop, Kiev, Ukraine (2004).
- [46] C.E. Hill, A.M. Lombardi, W. Pirkel, E. Tanke and M. Vretenar, Performance of the CERN Linac 2 with a high intensity proton RFQ.
- [47] P. Heikkinen, Private Communications with R. Scrivens, CERN, Geneva, Switzerland (2004).
- [48] J. Heinemeier, P. Hvelpund and F.R. Simpson, *J.Phys.B.* **9** (1976) 2669-2684.
- [49] A. Herschovitsch and J.G. Alessi, Proceedings of the 6th Intern. Symposium on the Production and Neutralization of Negative Ions and Beams, Brookhaven, NY, USA, AIP-Conference-Proceedings (1992).
- [50] M.A. Hone, The Duoplasmatron Ion Source for the new CERN Linac Preinjector, CERN/PS/LR 79-37, Geneva, Switzerland (1979).
- [51] I.S. Hong, Y.S. Hwang and Y.S. Cho, *Rev.Sci.Instr.* **73** (2002) 979-982.
- [52] T. Inoue et al., *Plasma Sources Sci. Technol.* **1** (1992) 75-81.
- [53] <http://www.inp.nsk.su/> (last checked 22.04.2005).
- [54] <http://www.isis.rl.ac.uk/> (last checked 22.04.2005).
- [55] A. Jakob, C. Gabor, O. Meusel, J. Pozimski, H. Klein, U. Ratzinger, H^- LEBT in Frankfurt, Proceedings of the 8th European Particle Accelerator Conference, Paris, France (2002) 1906-1908.
- [56] A. Jakob, C. Gabor, O. Meusel, J. Pozimski, H. Klein, U. Ratzinger, Diagnostics at the Frankfurt H^- - LEBT, USA, AIP-Conference-Proceedings **639** (2002) 128-134.
- [57] A. Jakob, O. Meusel, J. Pozimski, H. Klein, A. Lakatos, Study of Space Charge compensated LEBT for ESS, Proceedings of the Particle Accelerator Conference, NY, USA **2** (1999) 1288-1290.
- [58] K. Jayamanna, D. Yuan, T. Kuo et al., *Rev.Sci.Instr.* **67** (1996) 1061-1063.
- [59] <http://www.jyu.fi/indexeng.shtml> (last checked 22.04.2005).

- [60] R. Keller et al., Progress with the SNS Front End Systems, Proceedings of the 2001 Particle Accelerator Conference, Chicago, IL, USA, AIP-Conference-Proceedings (2001) 70-72.
- [61] R. Keller, Ion-source and low-energy beam-transport issues for H^- accelerators, Proceedings of the Particle Accelerator Conference, NY, USA (1999) 87-91.
- [62] W.D. Kilpatrick, Rev.Sci.Instr. **28** (1957) 824-826.
- [63] K.I. Krylov, V.V. Kuznetsov, D.V. Penkin and N.N. Semashko, Proceedings of the 5th Intern. Symposium on Production and Neutralization of Negative Ions and Beams, Brookhaven, NY, USA, AIP-Conference-Proceedings **210** (1990) 290-297.
- [64] T. Kuo, D. Yuan, K. Jayamanna et al., Rev.Sci.Instr. **69** (1998) 959-961.
- [65] S. Kurz and S. Russenschuck, The application of the BEM-FEM coupling method for the accurate calculation of fields in superconducting magnets, Electrical Engineering - Archiv fuer Elektrotechnik, Berlin, Germany **82** (1999).
- [66] <http://laacg1.lanl.gov/laacg/services.html> (last checked 10.04.2005).
- [67] http://www.lanl.gov/organization/profiles/lansce_profile.shtml (last checked 22.04.2005).
- [68] <http://www.lanl.gov/external/> (last checked 22.04.2005).
- [69] <http://www.lbl.gov/> (last checked 22.04.2005).
- [70] <http://lhc-new-homepage.web.cern.ch/lhc-new-homepage/> (last checked 09.05.2005).
- [71] K.N. Leung et al., Appl.Phys.Lett. **47** (1985) 227-228.
- [72] K.N. Leung et al., Appl.Phys.Lett. **61** (1990) 1110-1116.
- [73] A.P. Letchford, C.P. Bailey, J.P. Duke, D.J.S. Findlay, J.W.G. Thomason, Measured performance of the ISIS RFQ, Proceedings of the 8th European Particle Accelerator Conference, Paris, France (2002) 927-929.
- [74] <http://linac2.home.cern.ch/linac2/publn.htm#l96> (last checked 18.04.2005).
- [75] E.Métral, M. Benedikt, K. Cornelis et al., High Intensity Proton Beams at CERN and the SPL study, APAC 2004, Gyeongju, Korea CERN-AB-2004-021-ABP (2004).
- [76] F. Naito et al., The JAERI/KEK joint project and its performance, Proceedings of the International LINAC Conference (LINAC 2002), Gyeongju, Korea (2002) 564-568.
- [77] E. Nicolopoulou, M. Bacal and H.J. Doucet, Journal-de-Physique **38** (1977) 1399-1404.

- [78] M. Okamura, T. Katayama, R.A. Jameson, T. Takeuchi, T. Hattori, H. Kashiwagi, Scheme for direct plasma injection into an RFQ linac, 14th International Symposium on Heavy Ion Inertial Fusion, Moscow, Russia, Laser-and-Particle-Beams, UK **20** (2002) 451-454.
- [79] J. Peters, Internal versus external RF coupling into a volume source, Proceedings of EPAC 2002, Paris, France (2002) 1727.
- [80] J. Peters, Review of high intensity H^- sources and matching to high power RFQ's, Proceeding of EPAC 2000, Vienna, Austria (2000) 113-117.
- [81] J. Peters, Rev.Sci.Instr. **71** (2000) 1069-1074.
- [82] J. Peters, Rev.Sci.Instr. **75** (2004) 1709-1713.
- [83] J. Peters, Rev.Sci.Instr. **69** (1998) 992-994.
- [84] J. Peters, The Status of DESY H^- sources, Proceedings of the 18th International LINAC Conference (LINAC 96), Geneva, Switzerland (1996) 199-201.
- [85] <http://physics.nist.gov/PhysRefData/Ionization/molTable.html> (last checked 10.04.2005).
- [86] <http://preprints.cern.ch/cernrep/1993/93-01/93-01.html> (last checked 18.04.2005).
- [87] C. Rossi et al., The SPL Front End: A 3 MeV H^- Test Stand at CERN, CERN-AB-2004-102 RF, Geneva, Switzerland (2004).
- [88] G. Rouleau, E.C. Golcher, E. Geros et al., H^- surface converter source development at Los Alamos, Proceedings of the 2003 Particle Accelerator Conference, Portland, Or , USA (2003) 73-75.
- [89] R. Scrivens, Proton and ion sources for high intensity accelerators, EPAC 2004, Lucerne, Switzerland, CERN-AB-2004-075 (2004).
- [90] J.D. Sherman, A. Avin, L. Hansborough et al., Rev.Sci.Instr. **69** (2004) 1003-1008.
- [91] J.D. Sherman, W.B. Ingalls et al., Review of scaled Penning H^- surface plasma source with slit emitters for high duty factor LINACS, Proceedings of EPAC 2002, Paris, France (2002) 284-286.
- [92] J. Sherman, E. Pitcher, R. Stevens and P. Allison, H^- beam neutralization measurements in a solenoidal beam transport system, Upton, NY, USA, AIP Conference Proceedings **287** (1994) 686-694.
- [93] M. Shirai, M. Ogasawara et al., Rev.Sci.Instr. **67** (1996) 1085-1087.
- [94] H.V. Smith, J.P. Allison and J.D. Sherman, Rev.Sci.Instr. **65** (1994) 123-128.
- [95] H.V. Smith, J.P. Allison et al., Initial operation of the CW8X H^- ion source discharge, Proceedings of the 1993 Particle Accelerator Conference, Washington DC, USA (1993) 3172-3174.

- [96] <http://www.snu.ac.kr:6060/engsnu/> (last checked 22.04.2005).
- [97] I.A. Soloshenko, *Rev.Sci.Instr.* **75** (2004) 1694-1698.
- [98] D. Spence, K.R. Lykke and G.E. McMichael, Plasma Modified Production of High-current, High-purity cw H⁺, D⁺, and H⁻ Beams from Microwave-driven Sources, *Proceeding of the 18th International LINAC Conference (LINAC 96)*, Geneva, Switzerland (1996) 71.
- [99] J.W. Staples, J.J. Ayers, D.W. Cheng, J.B. Greer, M.D. Hoff and A. Ratti, The SNS Four-Phase LEBT Chopper, NY, USA, *AIP Conference Proceedings* (1999) 1961-1963.
- [100] J.W. Staples, Private communications, Berkeley National Laboratory, University of California, CA, USA (2005).
- [101] T. Sakurabazashi, A. Hatayama and M. Bacal, *Rev.Sci.Instr.* **95** (2004) 3937-3942.
- [102] P.G. Steen and W.G. Graham, The effect of caesium and xenon addition on negative ion production, *Joint 7th Intern. Symposium on the Production and Neutralization of Negative Ions and Beams and 6th European Workshop on the Production and Application of Light Negative Ions*, Brookhaven, NY, USA, *AIP Conference Proceedings* **380** (1996) 16-24.
- [103] T. Steiner, PhD-thesis, H⁻ source developments and diagnostics at CERN, Geneva, Switzerland (2005).
- [104] H.C. Straub et al., *Phys.Rev.A.* **54** (1996) 2146-2152.
- [105] T. Takeuchi, T. Katayama, M. Okamura, K. Yano, A. Sakumi, T. Hattori, N. Hayashizaki, R.A. Jameson, *Nuc. Instr. Meth. Phys. Res.B.* **188** (2002) 233-237.
- [106] E. Tanke, Realignment of the Linac2 LEBT during the 1994/1995 machine shut-down, (1995) PS/HI-Note 95-10 (MD).
- [107] http://tdserver1.fnal.gov/8gevinacPapers/Meeting_Minutes/Cryomodules/TraceWin/TRACE3D.PDF.
- [108] J.W.G. Thomason, P.J. Barrat et al., The RFQ test stand ion source at RAL, *Proceedings of EPAC2002*, Paris, France (2002) 1741-1743.
- [109] R. Tracz, PATH Manager User Guide, CERN document PS/HP-note-99 (1999) unpublished.
- [110] <http://www.triumf.info/> (last checked 22.04.2005).
- [111] A. Ueno, Y. Kondo, K. Ikegami, N. Kamikubota and C. Kubota, First beam test of a volume production H⁻ ion source with a LEBT, *Proceedings of the 20th International LINAC Conference (LINAC 1998)*, Monterey, California (2000) 256-258.
- [112] O.L. Veresov, S.V. Grigorenko and S. Udovichenko, *Technical Physics*, **45** (2000) 1009-1013.

-
- [113] K. Volk, A. Maaser, H. Klein, The Frankfurt H^- source for the European Spallation Source, Proceedings of the International LINAC Conference (LINAC 98), Chicago, IL, USA (1998) 896-898.
- [114] B. Vosicki, M. Buzic and A. Cheretakis, The Duoplasmatron source for the CERN PS Linac, MPS/Int.LIN 66-11 (1966).
- [115] S.R. Walter, K.N. Leung and W.B. Kunkel, J.Appl.Phys. **64** (1988) 3424-3428.
- [116] <http://www.webelements.com/webelements/elements/text/Kr/key.html>
(last checked 10.04.2005).
- [117] R.F. Welton and M.P. Stockli, Rev.Sci.Instr. **73** (2002) 1-4.
- [118] R.F. Welton, M.P. Stockli and R.Keller, Development and status of the SNS ion source, Proceedings of the 2003 Particle Accelerator Conference, Portland, Or, USA (2003) 3306-3308.
- [119] B. Wolf, Handbook of Ion Sources, ISBN 0-8493-2502-1, CRC Press (1995).
- [120] H. Zhang, Ion Sources, ISBN 5-540-65747-9, Springer Verlag (1999).
- [121] Z. Zakrzewski, M. Moisan, Plasma Sources Sci. Technol. **4** (1995) 379.

Appendix A

Drawings of the H^- ion source

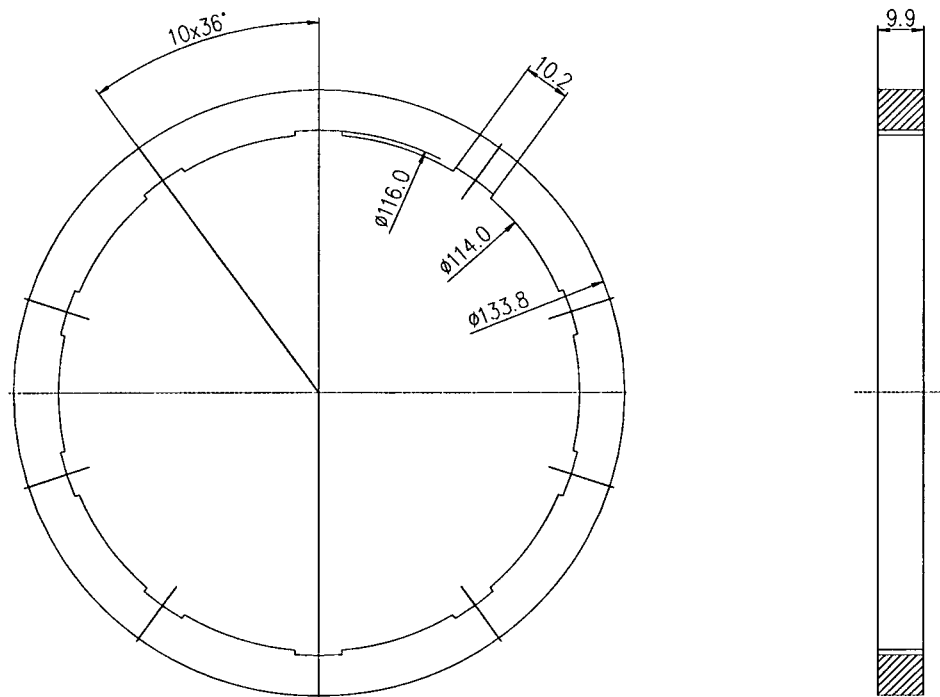


Figure A.1: Example of an iron ring with the slots for the installation of the permanent magnets (Dimensions in mm).

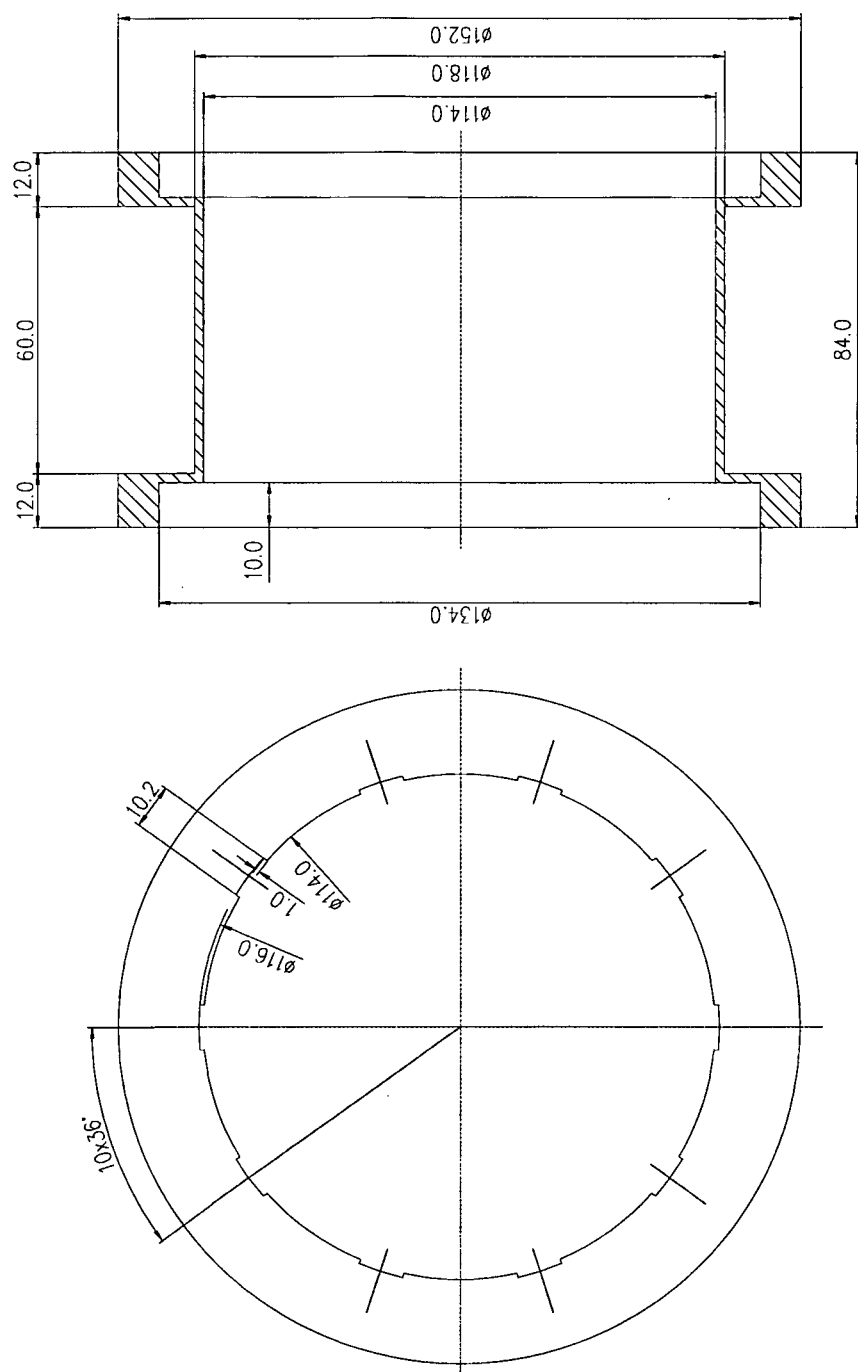


Figure A.2: The antico body of the solenoids (Dimensions in mm).

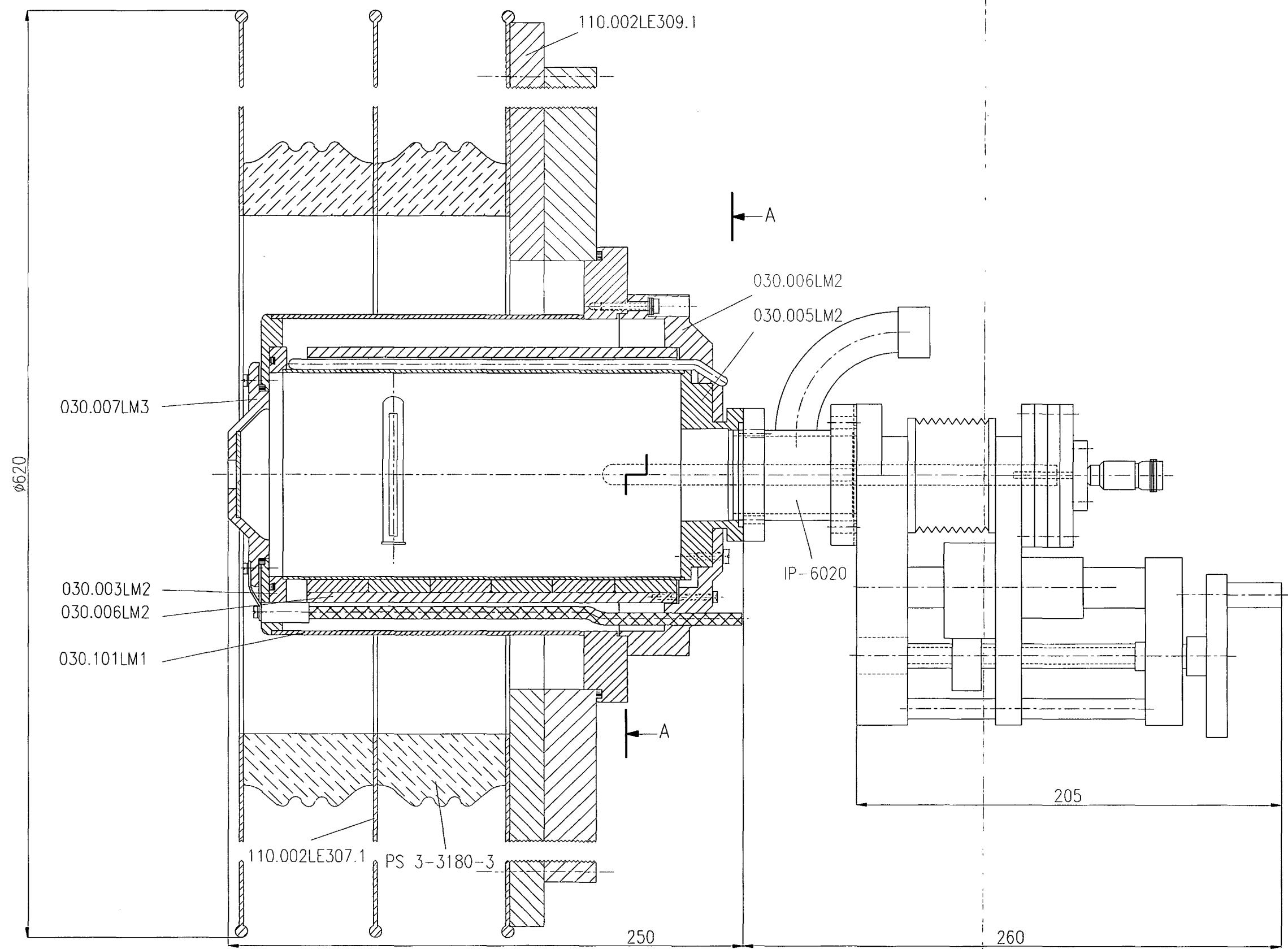


Figure A.3: Side view of the H⁻ ion source with the multicusp magnetic structure (Ref. AC: ip-6021, 29.03.2005, Hadorn/Steiner)

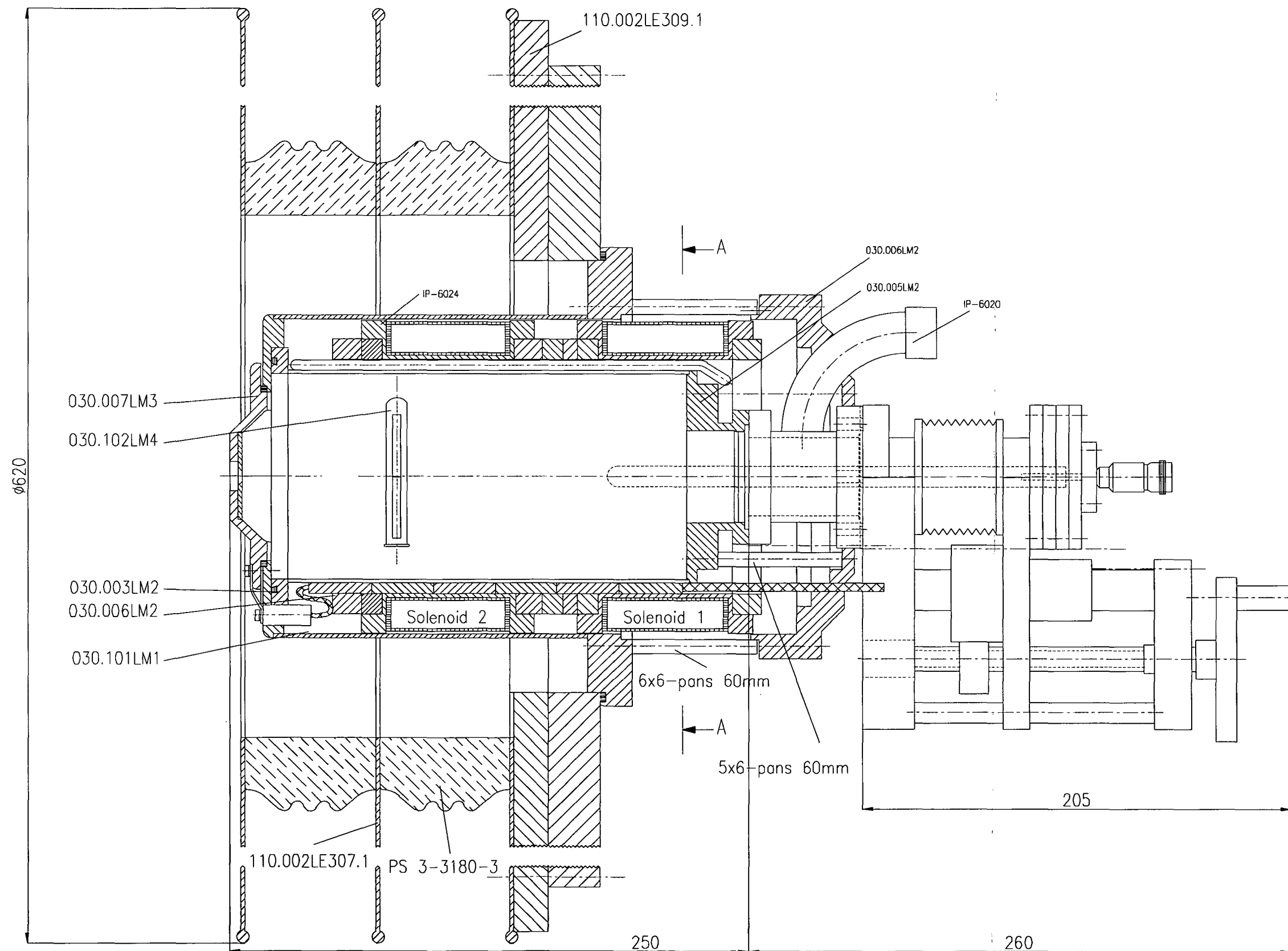


Figure A.4: Side view of the H^- ion source with the solenoidal magnetic structure (Ref. AC: ip-6021, 29.03.2005, Hadorn/Steiner)

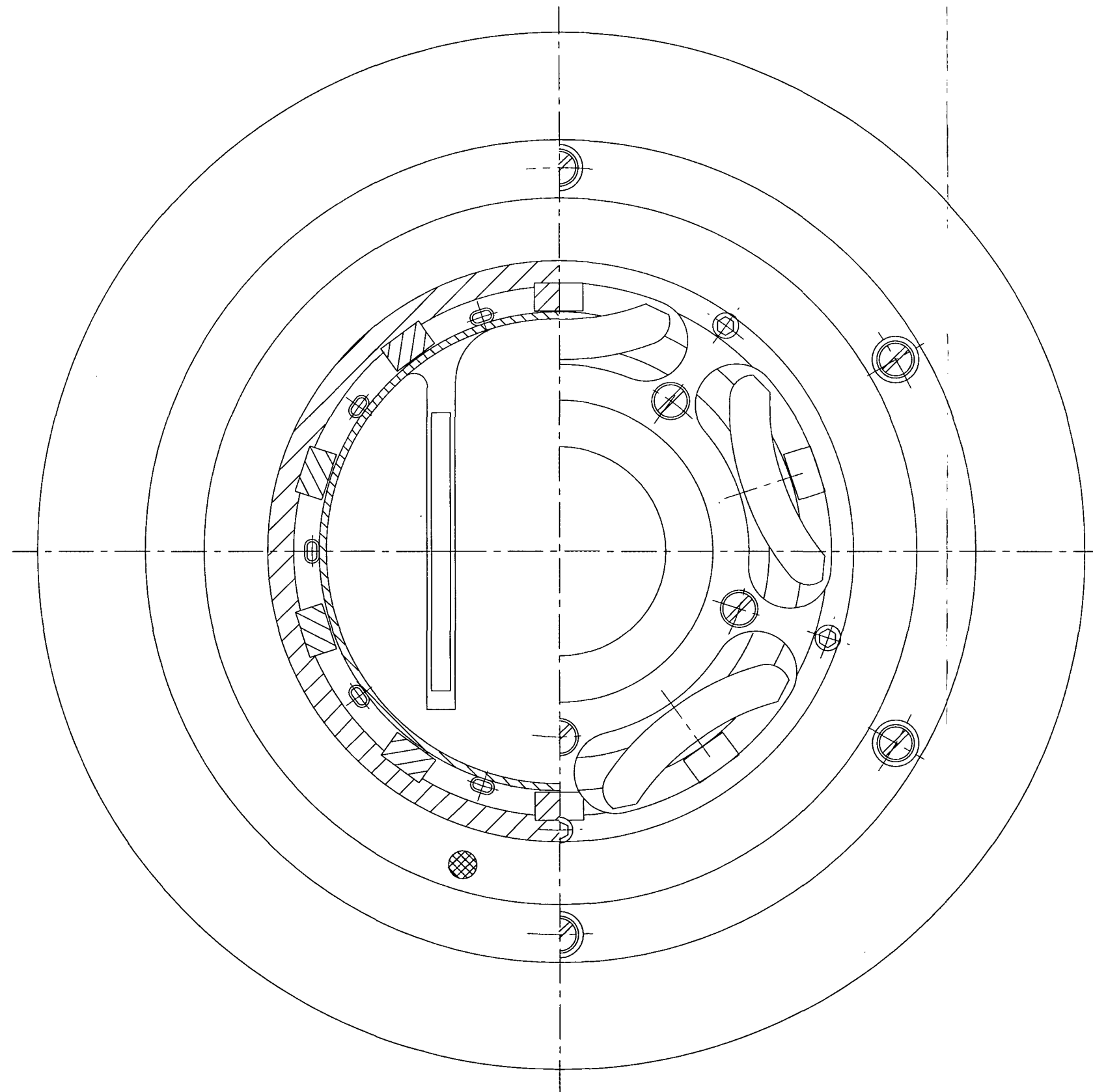


Figure A.5: Front view of the H⁻ ion source with the multicusp magnetic structure (Ref. AC: ip-6021, 29.03.2005, Hadorn/Steiner)

Curriculum Vitae

Thomas Steiner

PERSONAL DATA

Name: Thomas Steiner
Date of Birth: 20. Februar 1975
Nationality: Austrian
Marital Status: Single
Military service: completed

CONTACT ADDRESS

Dorfstr.59
2560 Neusiedl
Austria
email: thomas.steiner@cern.ch

CURRENT POSITION

Oct. 2002 - present: Doctoral student in the Accelerators & Beam Physics Group
at CERN
Thesis topic: *H⁻ source developments and diagnostics at CERN*

EDUCATION

Oct. 2001: Degree of Dipl. Ing. (Master of Science) in Physics
Thesis topic: „*Einfluss des Drucks in der quantitativen Analytik mittels ESEM*“ (Influence of the pressure in quantitative analytic by means of an ESEM)
1993 - 2001: Vienna University of Technology, Subject area: Technical Physics
1985 - 1993: High School, realistic branch, Berndorf, Austria
specialist area work („*Fachbereichsarbeit*“), topic: „*Aufbau und Struktur von Hauptreihensternen*“ (Structure of main sequence stars)

PART-TIME WORK

1993 - 2002: System Administrator for REXAM Austria Dosen, former PLM Austria, Enzesfeld, Austria
Summer 1993 - Postman, Berndorf, Austria
Summer 2000:
Winter 1996 - Ski instructor in several skiing resorts in Austria
Winter 2000:
Summer 1991 - Factory worker in a dairy, Baden, Austria
Summer 1992:

LANGUAGES

German: native language
English: excellent
French: beginner level

COMPUTER SKILLS

Operating Systems: MS Windows
Software and Languages: MS Office, Origin, AutoCAD, Poisson Superfish, Microwave Studio, Latex, ANSYS, Visual Basic, basic knowledge in Fortran

HOBBIES AND INTERESTS

mountaineering, skiing, climbing, traveling

LIST OF PUBLICATIONS

- C.Hill, D.Küchler, R.Scrivens, T. Steiner, *H⁻ source developments at CERN*, poster, CARE-HHH-2004, Geneva, Switzerland (2004).
- C. Rossi, T. Steiner et al., The SPL Front End: A 3 MeV H⁻ Test Stand at CERN, CERN-AB-2004-102 RF, Geneva, Switzerland (2004).
- T.Steiner, *H⁻ source developments at CERN*, Cern Accelerator School, best poster, Baden, Austria (2004).
- C.Hill, D.Küchler, R.Scrivens, T. Steiner, *H⁻ source developments at CERN*, H⁻-workshop, Kiev (2004).
- T. Steiner, „*Einfluss des Drucks in der quantitativen Analytik mittels ESEM*“, Diploma thesis, Vienna, Austria (2001).